ABSTRACT

Title of dissertation: PROBING THE NATURE OF RADIATIVE
PROCESSES WITHIN RADIO GALAXIES
USING THE FERMI GAMMA-RAY
LARGE AREA TELESCOPE

Jeffrey D. Magill
Doctor of Philosophy, 2018

Dissertation directed by: Doctor Jeremy Perkins
NASA Goddard Space Flight Center

Adjunct Associate Professor Julie McEnery
Department of Physics

Radio galaxies, active galactic nuclei with misaligned relativistic jets and large diffuse extended lobe structures, are home to radiative processes which are still not well understood. In this thesis, I describe my use of γ-ray photon data from the *Fermi* Large Area Telescope to investigate these radiative processes in the case of two radio galaxies, Fornax A and Centaurus A. I describe my discovery of the spatially extended nature of the γ-ray emission from Fornax A and my observation of a γ-ray intensity which is not consistent with the predicted process of stray energetic electrons inverse-Compton scattering with extragalactic background light photons. I describe how I positively identified a new γ-ray spectral component from the core region of Centaurus A jointly with data from the High Energy Stereoscopic System and how the spectral component can be explained by the addition of a second hidden zone of synchrotron self-Compton emission. I describe my discovery of fine filamentary sub-structures in the γ-ray lobes of Centaurus A using

a new imaging technique which I created, mapping out the unexpected γ-ray emission farther from the assumed central engine than we have observed in radio. I discuss how my observations of the Centaurus A lobes suggest local re-acceleration or channels of negligible magnetic field allowing long distance high energy particle paths.

Probing the Nature of Radiative Processes within Radio Galaxies using the Fermi Gamma-Ray Large Area Telescope

by

Jeffrey David Magill

Dissertation submitted to the Faculty of the Graduate School of the
University of Maryland, College Park in partial fulfillment
of the requirements for the degree of
Doctor of Philosophy
2018

Advisory Committee:
Professor Peter Shawhan, Chair
Doctor Jeremy Perkins, Advisor
Professor Julie McEnery, Co-Advisor
Professor Jordan Goodman
Professor M. Coleman Miller, Dean's Representative

Preface

Chapter 4 of this thesis is taken from "Fermi Large Area Telescope Detection of Extended Gamma-Ray Emission from the Radio Galaxy Fornax A," [1] published in The Astrophysical Journal in 2016, of which I am the primary author. It has been edited for clarity for its inclusion into the thesis.

Chapter 5 is taken from "The γ-ray spectrum of the core of Centaurus A as observed with H.E.S.S. and Fermi-LAT," [2] accepted into Astronomy & Astrophysics in 2018. The paper was led by the H.E.S.S. Collaboration, and I am the primary author for the LAT analysis. I have removed details of the analysis for which I did not take part, referring the reader to the article where appropriate, and edited it for clarity for its inclusion into the thesis.

Chapter 6 covers my own analysis which is planned to result in a paper soon, title and journal yet to be determined.

Table of Contents

Preface ii

List of Tables vi

List of Figures vii

List of Abbreviations xi

1 Introduction 1
- 1.1 Thesis Organization . . . 2

2 Active Galactic Nuclei 3
- 2.1 History . . . 3
- 2.2 AGN Taxonomy . . . 5
  - 2.2.1 Blazars . . . 5
  - 2.2.2 Radio Galaxies . . . 7
- 2.3 Emission Mechanisms of Radio Galaxies . . . 9
  - 2.3.1 Leptonic . . . 9
    - 2.3.1.1 Synchrotron Radiation . . . 11
    - 2.3.1.2 Inverse-Compton Radiation . . . 12
  - 2.3.2 Hadronic . . . 14

3 *Fermi* Large Area Telescope (LAT) 19
- 3.1 Overview . . . 19
- 3.2 Instrument . . . 21
  - 3.2.1 Tracker (TKR) . . . 21
  - 3.2.2 Calorimeter (CAL) . . . 23
  - 3.2.3 Anti-Coincidence Detector (ACD) . . . 27
  - 3.2.4 Uncertainties . . . 30
- 3.3 LAT Data . . . 33
  - 3.3.1 Pass 8 . . . 35
- 3.4 LAT Analysis . . . 37
  - 3.4.1 Basics . . . 37

3.4.2 `fermipy` 39

4 Fornax A 42
4.1 Introduction 42
4.2 Observations & Analysis 45
4.2.1 *Fermi*-LAT Observations 45
4.2.2 Extension and Morphology 49
4.2.2.1 Spatial Extension 51
4.2.2.2 Blind Tests for Morphology 51
4.2.2.3 Radio-Motivated Tests for Morphology 54
4.2.3 Spectral and Temporal Analysis 58

5 Centaurus A Core 62
5.1 Introduction 62
5.2 H.E.S.S. observations and results 65
5.2.1 Observations 65
5.2.2 Results of the observations of Cen A with H.E.S.S. 66
5.3 *Fermi*-LAT observations and results 68
5.3.1 Observations and analysis 68
5.3.2 Results of the observations of Cen A with *Fermi*-LAT 74

6 Centaurus A Lobes 78
6.1 Introduction 78
6.2 Observations & Analysis 79
6.2.1 *Fermi*-LAT Observations 79
6.2.1.1 γ-ray Morphology and Background Modeling 82
6.2.1.2 Checks on Morphology 86
6.3 Results 88

7 Discussion 92
7.1 Fornax A 92
7.1.1 Leptonic Modeling 94
7.1.2 Hadronic Modeling 95
7.2 Cen A Core 96
7.3 Cen A Lobes 99

8 Conclusions 103
8.1 Future work 105

A Diffuse extragalactic background radiation 110

B Statistics 112
B.1 Parameter Estimation 112
B.1.1 Maximum Likelihood 113
B.2 Model Comparison 116
B.2.1 Likelihood Ratio Test 118

C Light curves 120
C.1 Light curves with `fermipy` 121
C.1.1 Variability 121

Bibliography 124

List of Tables

4.1 Fornax A LAT spectral fit results. Each fit was performed leaving normalization and spectral shape parameters of all sources free, except for the models for the diffuse background γ rays which were fit with only normalization. 48

4.2 Fornax A spatial model comparisons. Calculated using the likelihood ratio computation as described in Section 4.2. The third column is the difference in the number of degrees of freedom (DOF) between the two hypotheses. The alternative hypotheses are preferred over the corresponding null hypotheses by the significances σ in the fifth column. 50

4.3 Fornax A total lobe LAT spectral flux assuming radio lobes template spatial model. For bins with a * added, energy fluxes given are 95% confidence upper limits. 60

6.1 Best-fit spectral parameters associated with each of the six independent extracted lobe morphology templates. 90

B.1 Common interpretation of the Bayes factor from Harold Jeffreys [3]. . . . 117

List of Figures

2.1 Color composite image of radio galaxy Centaurus A showing typical features of an AGN. Arrows show viewing angle with respect to the jet. Image made with data from ESO/WFI (Optical), MPIfR/ESO/APEX/A.Weiss et al. (Submillimetre), NASA/CXC/CfA/R.Kraft et al. (X-ray). 6
2.2 Very Large Array (VLA) radio images of four radio galaxies, showing clear morphological differences between FR 1 type (top) and FR 2 type (bottom). Observing frequency of top-left is 1477 MHz; top-right, 608 MHz; bottom-left, 1650 MHz; and bottom-right, 4860 MHz. 8
2.3 Spectral energy distribution (SED) of bright blazar Mrk 421 from all available wavelength bands from radio through TeV. This shows a very clear case of the typical double-bump structure of AGN spectra which can be explained as synchrotron emission creating the lower energy bump and inverse-Compton creating the higher energy bump. Shown in red and green lines are two possible synchrotron self-Compton models which can fit the data [4]. 10
2.4 Example particle cascade from a proton colliding with a nucleus. Notably, γ-ray photons and neutrinos may be produced.[1] 16
2.5 Broadband spectrum of bright blazar Mrk 421 showing a hadronic model of the high-energy bump with the low-energy bump modeled with electron synchrotron emission. The neutral pion cascade component is shown in the purple dotted line, the charged pion cascade is shown in the green dashed-dotted line, the muon synchrotron and cascade is shown in the blue triple-dot-dashed line, the proton synchrotron and cascade is shown in the red dashed line, and the sum of all components is shown in the black solid line. Note the significant difference between this and the leptonic model in Fig. 2.3 in the MeV energy band. [4] 18

3.1 Cutaway of the LAT showing an example path of a γ ray converting into an electron-positron pair. [5] 20
3.2 Side view diagram showing a charged particle traveling through the active depletion region of an SSD. The depletion region is increased with a reverse bias, wherein the n side is held at a greater electric potential than the p side. [6] 22

3.3 Side view diagram of a Tracker tower showing the arrangement of layers [7]. 24
3.4 Fully assembled Tracker instrument showing the 16 towers [5]. 25
3.5 Exploded view of the Calorimeter, showing alternating orientations of the CsI(Tl) crystal elements, each with a photodiode attached to both ends [5]. 26
3.6 Photograph of a single plastic scintillating ACD tile showing embedded wavelength shifting (WLS) fibers to collect signal light bundled into two clusters for detection by two photomultiplier tubes [8]. 27
3.7 Diagram of the ACD tiles, showing overlapping tile positioning pattern and location of the ACD PMTs and electronics [5]. 29
3.8 Showing two examples of simulated backsplash events in the LAT. Red lines indicate charged particles and blue lines indicated photons [8]. . . . 31
3.9 68% containment PSF of the LAT with the latest Pass 8 dataset, as derived from Monte Carlo simulations. Also shown are the containment angles for each of the divided PSF event type quartiles.[2] 32

4.1 Relative smoothed (4.7 px, 0.°24 Gaussian FWHM) residual γ-ray counts ((counts - model)/model) in the 1.°5 square region around the core of Fornax A between 1 and 300 GeV. Overlaid are the radio contours (gray lines) from the VLA observations of [9] with the radio core (position indicated by A) subtracted. The γ-ray residual counts are elongated in a similar way to the radio lobes. Also shown are the 95% confidence error ellipses for 2FGL J0322.4−3717 and 3FGL J0322.5−3721; the 3FGL source has the smaller ellipse. The dashed circle shows the 95% confidence error circle from our maximum-likelihood localization of the region as a single point source centered at position B. The other points (labeled C, D, E) are the locations of various sources and test sources, as detailed in the text and in Table 4.2. This figure is reproduced here from the publication [1]. 47
4.2 $\Delta \log \mathcal{L}$ between a flat disk of radius 0.°03 (i.e., point-like) and flat disks of various radii. A cubic fit gives a maximum likelihood radius of 0.°33 ± 0.°05. The increase in $\mathcal{L}$ from 0.°03 to the maximum likelihood radius indicates the emission is not point-like. This figure is reproduced here from the publication [1]. 52
4.3 $\Delta \log \mathcal{L}$ between the non-rotated radio lobe template and the template rotated around the central core indicating that the unrotated radio morphology is preferred. This figure is reproduced here from the publication [1]. 53
4.4 Plot of the template for the Fornax A lobes used in this study created from data from VLA at 1.5 GHz. Creation of the template is described in Sect. 4.2.2.3 and with greater detail in Appendix A of McConville's Ph.D. thesis [10]. 56

4.5 Broadband SED of the lobes of Fornax A (bottom panel) and detailed view of the high-energy part of the SED (top panel). As in [11], we used archival measurements of the total lobe radio flux densities (shown in red) from [12–17], as collected by [18], replacing an extrapolated 100 MHz data point from [12] with an 86 MHz measurement [19]. The 3-year integrated *WMAP* data are shown in magenta [20], and X-ray data from ROSAT [21] are shown in green. The LAT data points from this study are shown in blue. The black upper limit point is from EGRET [22]. The black solid lines from left to right show the synchrotron ($< 10^{13}$ Hz), IC/CMB ($> 10^{13}$ Hz), and IC/EBL (on the assumption of the model of [23]) flux models ($> 10^{15}$ Hz). The dashed black line shows the IC/EBL flux models assuming the fast evolution model of [24]. The dotted red and cyan lines show the IC upscattered host galaxy photon flux from infrared and optical, respectively. The solid green line shows the hadronic model flux, while the solid magenta line shows the combined hadronic and leptonic model flux. This figure is reproduced here from the publication [1]. 61

5.1 SED of Cen A γ-ray core. *Fermi*-LAT and H.E.S.S. data points along with a high-energy power-law extrapolation of the γ-ray spectrum measured below the break energy. Eight years of *Fermi*-LAT data and 213 hours of H.E.S.S. data were used. Statistical error bars are shown. This figure is reproduced here from the publication [2]. 67

5.2 Template of Cen A lobes created from *WMAP* at 22 GHz [25]. 70

5.3 “Filled in” modified version of the 22 GHz *WMAP* Cen A lobes template as described in Sect. 5.3.1 72

5.4 Template of the Cen A lobes created from Parkes radio data at 6.3 cm wavelength [26]. 73

5.5 Change in overall $\log\mathcal{L}$ while fixing Cen A core break energy to values within the range 0.9 – 7.0 GeV as derived from *Fermi*-LAT data using the *WMAP*, modified *WMAP*, and Parkes templates and compared to the $\log\mathcal{L}$ value at 0.9 GeV for the *WMAP* template. The solid vertical line shows the best-fit value of the break energy parameter, while the dashed vertical lines show 1σ interval for the parameter. This figure is reproduced here from the publication [2]. 76

6.1 TS map of 9.7 years of Pass 8 LAT data cut above 1 GeV in the $15^\circ \times 15^\circ$ ROI surrounding Cen A. This plot highlights the significant excess γ-ray emission present after modeling all visible point sources and the *WMAP* template (see Fig. 5.2) for the Cen A lobes. White text labels indicate sources being modeled. Those starting with “PS” were added during the analysis. 80

6.2 Broadband SED of emission from each lobe of Cen A. See the article for details [25]. 81

6.3 Detailed SED of emission from each lobe of Cen A with 10 month LAT data points showing IC contributions from each seed photon field. [25] . . 81
6.4 9-year γ-ray morphology of the outer lobes of Cen A extracted from *Fermi*-LAT data as described in Section 6.2.1.1. Plots (a) and (c), respectively, show the north and south lobe images below 1 GeV. Plots (b) and (d), respectively, show the north and south lobe images above 1 GeV. Plot (e) shows the extended southern tail feature and plot (f) shows the bright hotspot feature, both of which are applied across the full analysis energy range. The overlayed white circles shown on plots (a) – (d) show the largest possible 68% containment PSF within the template's energy range. 87
6.5 Likelihood profiles of each extracted γ-ray template while applying a 2D Gaussian smoothing filter with variable sigma. The filtered templates applied are arranged here correspondingly with their arrangement in Fig. 6.4. 89
6.6 SEDs of each of the six independent lobe templates. The SEDs are arranged here correspondingly with their arrangement in Fig. 6.4. 91

7.1 SED of Cen A core with model fits as described in text. The red curve corresponds to an SSC component designed to fit the radio to sub-GeV data. The blue curve corresponds to a second SSC component added to account for the highest energy data. The black curve corresponds to the sum of the two components. SED points as derived from H.E.S.S. and *Fermi*-LAT data in this study are shown with open circles. This figure is reproduced here from the publication [2].[3] 98

8.1 Sensitivity over energy of various astronomy observatories in the X-rays to γ rays. 107
8.2 Angular resolution of the proposed AMEGO instrument, showing the difference between Compton and pair conversion events. 108

A.1 Schematic representation of the spectral energy distribution of the diffuse extragalactic background radiation.[4] 111

B.1 Example profile likelihood 115

List of Abbreviations

2FGL	*Fermi*-LAT second year catalog
3FGL	*Fermi*-LAT Third Source Catalog
ACD	Anti-Coincidence Detector
AGN	active galactic nucleus
AMEGO	All-sky Medium Energy Gamma-ray Observatory
BL Lac	BL Lacertae
CAL	Calorimeter
Cen A	Centaurus A
CMB	cosmic microwave background
CsI(Tl)	thallium-activated cesium iodide
DOF	degree of freedom
EBL	extragalactic background light
EC	external Compton
EGRET	Energetic Gamma Ray Experiment Telescope
FGST	Fermi Gamma Ray Space Telescope
FITS	Flexible Image Transport System
FL8Y	Preliminary LAT 8-year Point Source List
FR	Fanaroff-Riley
FSRQ	flat-spectrum radio quasar
FSSC	*Fermi* Science Support Center
GBM	Gamma-ray Burst Monitor
GRB	gamma-ray burst
GTI	Good Time Interval
H.E.S.S.	High Energy Stereoscopic System
HE	high energy (100 MeV–100 GeV)
IC	inverse Compton
IR	infrared
IRF	instrument response function
LAT	Large Area Telescope

Mrk	Markarian
PMT	photomultiplier tube
PSF	point spread function
ROI	region of interest
SED	spectral energy distribution
SOI	source of interest
SSC	synchrotron self-Compton
SSD	silicon strip detector
TDRSS	Tracking and Data Relay Satellite System
TKR	Tracker
TS	test statistic
UV	ultraviolet
VHE	very high energy (30 GeV–30 TeV)
VLA	Very Large Array
WLS	wavelength shifting
WMAP	Wilkinson Microwave Anisotropy Probe
XML	Extensible Markup Language

Chapter 1: Introduction

Active galactic nuclei (AGNs) are the most luminous persistent sources of radiation known. The activity, thought to be caused by mass accretion into a central supermassive black hole, is capable of accelerating individual particles to greater energies than man-made accelerators have been capable of achieving. This makes AGNs great natural astrophysical laboratories for extreme physics. One particular variety is called the radio galaxy, characterized by its misaligned relativistic jets and observable diffuse lobe structures. These objects are the subject of study in this work.

The measurements done in support of this work were mainly performed from astrophysical observations of extraterrestrial γ rays. γ rays are the quantized particle representation of electromagnetic radiation, photons, which occupy the highest range of energies, typically above $\sim 100\,\mathrm{keV}$. Because of their high energies, γ rays can only be significantly produced by a limited set of celestial objects, most notably AGNs. γ-ray interactions with matter are limited to Compton scattering (interactions with electrons), electron-positron pair production (interaction with nuclei), photofission (nuclei splitting from absorbed γ-ray), and photodisintegration (nuclei emitting a subatomic particle from absorbed γ-ray), making them impossible to detect with conventional focusing optics and light collection. Instead, astrophysical observations require particle detectors designed specifically for one (or multiple) of these processes.

1.1 Thesis Organization

In this work, three studies are presented on the emission mechanisms, especially of γ-ray emission, taking place in radio galaxies. The investigation is centered around analysis of the γ-ray data taken by the *Fermi* Large Area Telescope (LAT). In Chapter 2, AGNs and the radiative emission mechanisms that are thought to take place within them are introduced. In Chapter 3, a description is given of the instrument whose data makes up the basis of this work, the *Fermi*-LAT. In Chapter 4, a discovery of γ-ray spatial extension in the radio galaxy Fornax A and an unexpectedly high γ-ray flux is discussed. Chapter 5 covers an investigation into an unexpected spectral feature in the core of the radio galaxy Centaurus A (Cen A) across high- and very-high-energy γ-ray regimes using *Fermi*-LAT and the High Energy Stereoscopic System. Chapter 6 introduces a γ-ray morphological study of the Cen A outer lobes, in particular a discovery of fine filamentary structures. In Chapter 7, the physical interpretations of the work of this thesis are discussed. Finally, this work is summarized in Chapter 8.

Chapter 2: Active Galactic Nuclei

Some galaxies host a nucleus that is more luminous than all of the galaxy's stars combined. These are called AGNs. These objects are extreme non-thermal emitters over a very wide range of wavelengths, including radio, microwave, infrared (IR), visible, ultraviolet (UV), X-rays, high energy (HE; 100 MeV–100 GeV) γ rays, and very high energy (VHE; 30 GeV–30 TeV) γ rays. Many AGNs produce a pair of relativistic, highly collimated jets directed roughly normal to the plane of the host galaxy. AGNs are thought to be powered by matter from a surrounding disc accreting into a central supermassive black hole ($10^{8–9}$ $M_\odot$).

2.1 History

[27] The origins of our understanding of the AGN can be traced back as far as 1909, when Edward Arthur Fath, while looking at spectral lines from spiral nebulae using the optical Lick Observatory near San Jose, CA, noticed an unusual spectroscopic signature from NGC 1068 featuring a combination of emission and absorption lines [28]. The lines were generally wider than expected, and this was attributed to Doppler shifting by Carl Keenan Seyfert in his 1943 study of emission lines from six spiral nebulae outside the galactic plane [29]. The addition of radio astronomy starting with work from Karl

Guthe Jansky in 1931 led to the ruling out of thermal emission as the major mechanism to produce the observed radiation around 1947 because the necessary temperatures were too high to be physical. The synchrotron process with local magnetic fields was proposed in 1950 by Alfvén & Herlofson [30] to explain this radio emission. Finally, in 1963, enough evidence had accumulated that quasi-stellar objects (quasars) have significantly high redshift (measurement of the amount which known nuclear spectral line frequencies are decreased, or reddened, by some process). The best explanation for the observed redshifting was Hubble expansion caused by separations of cosmological distances.

The inclusion of radio galaxies into the category of AGNs began in 1978 when Blandford & Rees proposed that BL Lacertae (BL Lac) objects could actually be radio galaxies but viewed down the jet. Eventually, this idea has largely been accepted into a full unified model of AGNs (see Sect. 2.2).

Prior to the launch of *Fermi*, the best observations of AGNs in the HE range came from the Energetic Gamma Ray Experiment Telescope (EGRET) onboard the *Compton Gamma Ray Observatory (CGRO)*. EGRET is a pair production detector, similar to *Fermi*-LAT, sensitive to γ rays between 20 MeV and 30 GeV. Although operating with similar principles, EGRET could not match the detection capabilities of its successor, *Fermi*-LAT, according to every metric, e.g., effective area, field of view, angular resolution, and sensitivity. However, EGRET played an important role in trail-blazing our knowledge of the HE band of astrophysical γ rays. After a series of viewing periods between April 1991 and September 1995, EGRET positively identified 67 AGNs, only one of which was a non-blazar (see Sect. 2.2), Cen A, the nearest AGN to our current location [31,32]. The detection of Cen A by EGRET created the expectation for potentially many more similar non-blazar AGNs in the HE regime with the anticipated launch of the *Fermi* observatory about a decade later. Particularly, with its improved angular resolution, *Fermi* offered the possibility of morphology studies of radio galaxies with HE γ rays. These extended and relatively nearby objects had since only been morphologically observed with radio waves and microwaves.

2.2 AGN Taxonomy

Many AGNs which were historically identified as different types have more recently been thought to be the same type of object, varying mainly because of the perspective from which we view them [33]. There are two broad categories of AGNs which are important to this work, those with their relativistic jet pointed in the direction or close to the direction of the viewer (blazars), and those whose relativistic jet is pointed away from the viewer (radio galaxies).

2.2.1 Blazars

Blazars are a broad category which refer to AGNs with the special case that one relativistic jet is aligned towards the viewer as shown in Fig. 2.1. Because of this alignment, their emission is much brighter than it would appear when misaligned. Blazars make up the vast majority of sources visible in γ rays ($> 86\%$), with most of the remaining being pulsars ($\sim 6\%$) [34]. Looking only outside of the plane of our Milky Way Galaxy, where this work is focused, they dominate the sky even more. A high degree of variability is often observed in blazars in HE γ rays [35], with flux change timescales as short as days

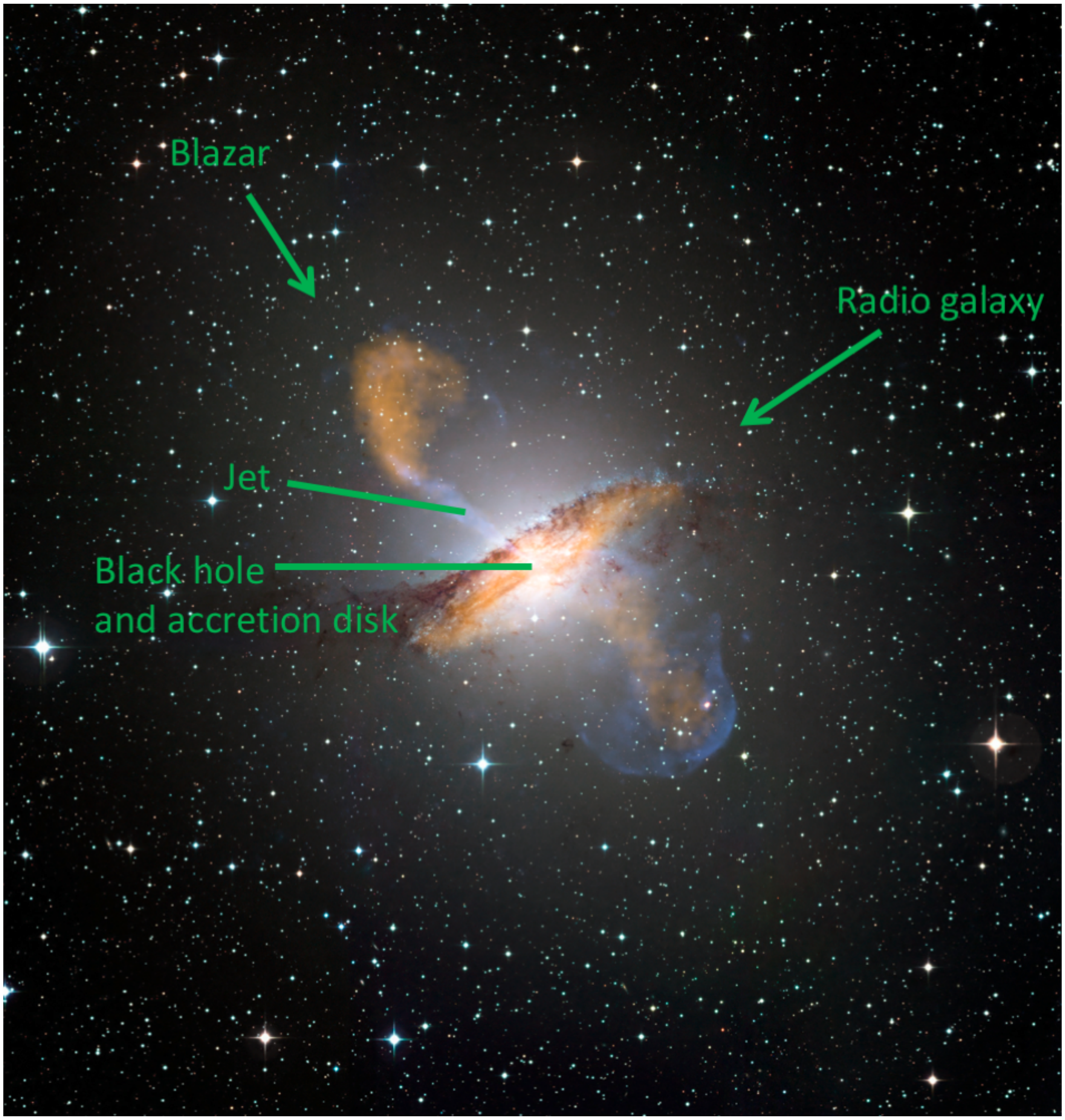

Figure 2.1: Color composite image of radio galaxy Centaurus A showing typical features of an AGN. Arrows show viewing angle with respect to the jet. Image made with data from ESO/WFI (Optical), MPIfR/ESO/APEX/A.Weiss et al. (Submillimetre), NASA/CXC/CfA/R.Kraft et al. (X-ray).

or even minutes [36]. They can be broken down into two classes, flat-spectrum radio quasars (FSRQs) and BL Lacs. The main distinction is that FSRQs are more distant, more luminous, and have stronger emission lines than BL Lacs.

Because AGN jets are well-collimated, alignment to the viewer is actually a very rare occurrence. However, in addition to the high luminosity offered by the jet's energy remaining confined to a small angle, these relativistic jets are also Doppler boosted to further increase their apparent brightness. This boosting offsets their low probability of occurrence, making them the most populous visible sources in the γ-ray sky, as well as the most distant observable objects known [33].

2.2.2 Radio Galaxies

When the jet of an AGN is misaligned with respect to the viewer as shown in Fig. 2.1, it is called a radio galaxy. They are much less luminous than blazars. It is by observing the structure of radio galaxies that we've been able to understand much more about the nature of all AGNs. Radio galaxies feature large extended structures, referred to as lobes, believed to be created by past material from the jet cooling and diffusing into the surrounding medium. Radio galaxies have been taxonomized into two classes by Fanaroff-Riley (FR) [37]: FR 1, with large jet opening angle, lobes brighter closer to the core, smooth falloff away from the core, high luminosity, often symmetric jets; and FR 2, with highly collimated jets, lobes brighter away from the core, sharper edges, and low luminosity. See Fig. 2.2 for typical morphologies of these two types. The nature and composition of radio galaxy lobes is a key subject of study in this work.

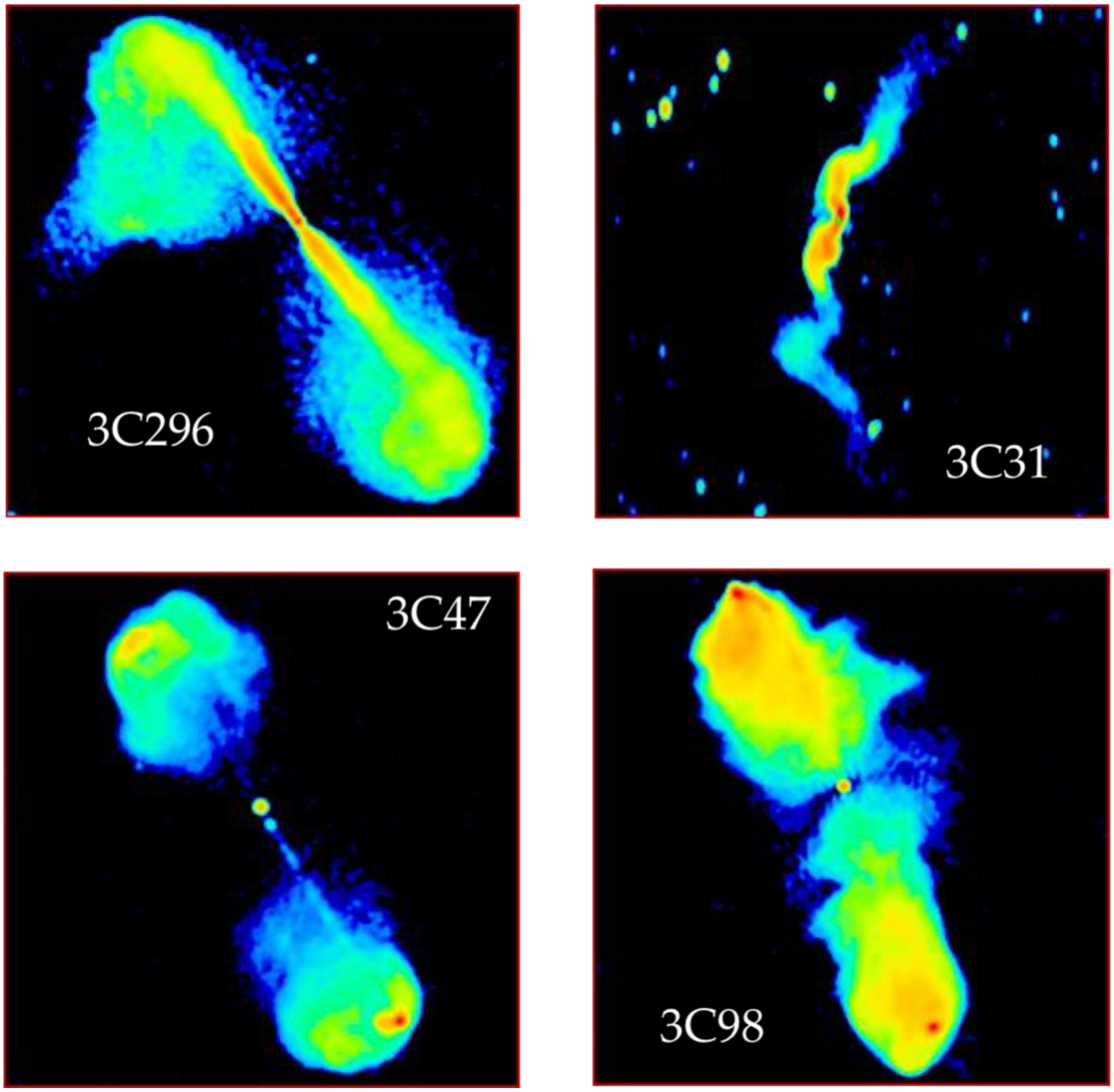

Figure 2.2: Very Large Array (VLA) radio images of four radio galaxies, showing clear morphological differences between FR 1 type (top) and FR 2 type (bottom). Observing frequency of top-left is 1477 MHz; top-right, 608 MHz; bottom-left, 1650 MHz; and bottom-right, 4860 MHz.

2.3 Emission Mechanisms of Radio Galaxies

Radio galaxies are non-thermal emitters of light across a broad spectrum. Unlike blazars, which appear as point-like sources at HE, some of the radio galaxies are spatially resolved and appear extended at HE. Thus, radio galaxy emission has the potential to be observed from both the central engine (core) and the extended lobe regions separately. High energy radio galaxy radiation is thought to be created by some combination of three fundamental processes: two leptonic, synchrotron and inverse-Compton, and one hadronic, neutral pion decay.

2.3.1 Leptonic

In the leptonic scenario, the low-energy emission (radio to optical) is mainly produced by the synchrotron process, while inverse-Compton scattering is responsible for the high-energy emission. While the literature is generally biased toward leptonic models on studies of AGNs, hadronic models remain a viable option. Multiwavelength spectra from most blazars are not in conflict with the leptonic scenario. For example, in Fig. 2.3 we see a very convincing match with the leptonic hypothesis across every available band in the spectrum of bright blazar Markarian (Mrk) 421 [4]. As with this example, spectra from AGNs, including radio galaxies, usually feature a low energy synchrotron “bump" peaking in the radio/microwave band and an inverse-Compton “bump", peaking in the hard X-ray to γ-ray band.

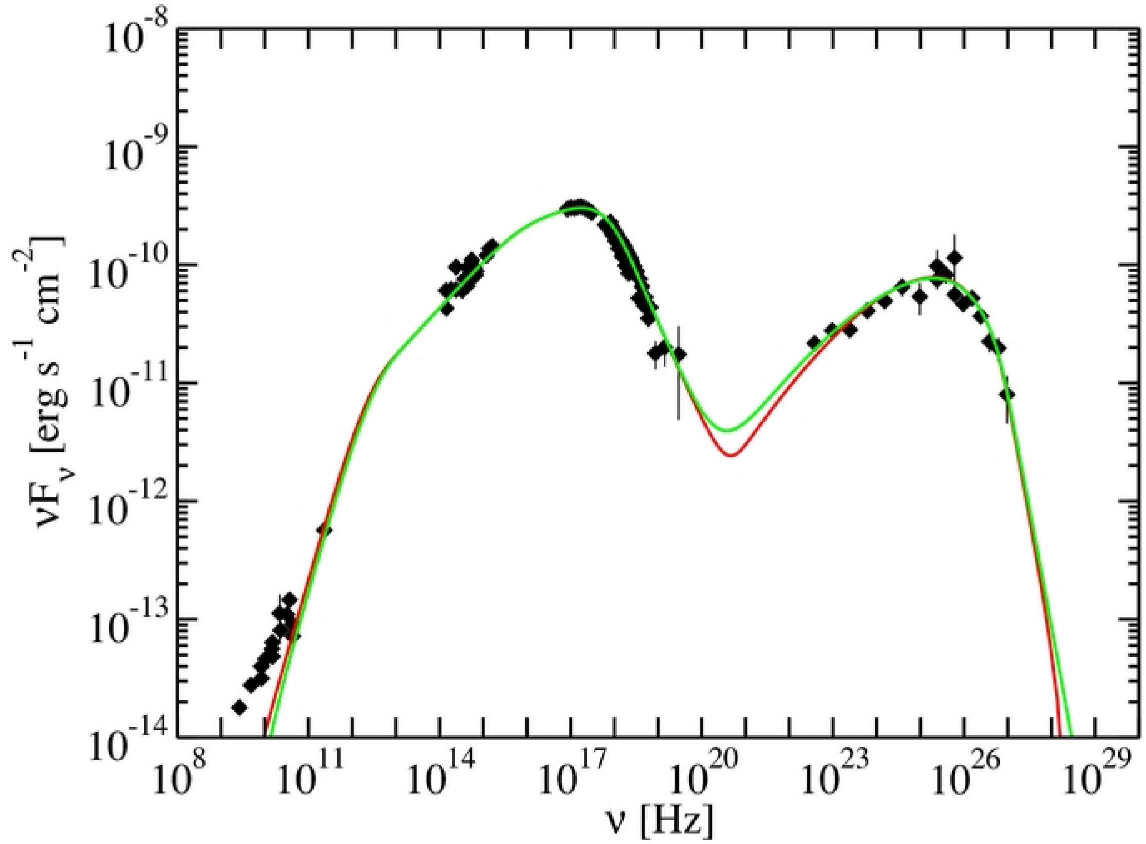

Figure 2.3: Spectral energy distribution (SED) of bright blazar Mrk 421 from all available wavelength bands from radio through TeV. This shows a very clear case of the typical double-bump structure of AGN spectra which can be explained as synchrotron emission creating the lower energy bump and inverse-Compton creating the higher energy bump. Shown in red and green lines are two possible synchrotron self-Compton models which can fit the data [4].

2.3.1.1 Synchrotron Radiation

Synchrotron radiation occurs when charged particles are forced to change direction by an external magnetic field. A single charge with mass m and charge q moving with velocity $\mathbf{v}$ through a magnetic field $\mathbf{B}$ will experience a force given by the Lorentz force law (in cgs units)

$$\mathbf{F} = \frac{q}{c}\mathbf{v} \times \mathbf{B},$$

assuming no electric field is present. When $|\mathbf{v}|$ is nearly c, we can use the relativistic mass γm, where $\gamma = \frac{1}{\sqrt{1-\frac{\mathrm{v}^2}{c^2}}}$ is the Lorentz factor. Using Newton's Second Law, we get that the acceleration experienced by the charge is

$$\mathbf{a} = \frac{\mathbf{F}}{\gamma m} = \frac{q}{\gamma mc}\mathbf{v} \times \mathbf{B},$$

or,

$$|\mathbf{a}| = \frac{qvB}{\gamma mc}\sin\alpha,$$

where α is the angle between $\mathbf{v}$ and $\mathbf{B}$. The Larmor formula gives us the total power radiated by the accelerating charge as

$$P = \frac{2}{3}\gamma^4\frac{q^2a^2}{c^3} = \frac{2}{3}\gamma^4\frac{q^2}{c^3}\frac{q^2v^2B^2}{\gamma^2m^2c^2}\sin^2\alpha = \frac{2}{3}\frac{\gamma^2q^4v^2B^2}{c^5m^2}\sin^2\alpha. \tag{2.1}$$

If we want to find the average synchrotron power from each charge in a set of charges all with speed v and an isotropic distribution of directions, we can calculate it by averaging Eq. 2.1 over all directions:

$$\langle P\rangle = \frac{2}{3}\frac{\gamma^2q^4v^2B^2}{c^5m^2}\langle\sin^2\alpha\rangle.$$

We can do this by integrating over the solid angle:

$$\langle \sin^2 \alpha \rangle = \frac{\int \sin^2 \alpha \, d\Omega}{\int d\Omega} = \frac{1}{4\pi} \int \sin^2 \alpha \, d\Omega.$$

Then, changing to spherical coordinates with $d\Omega = \sin\alpha \, d\alpha \, d\phi$,

$$\langle \sin^2 \alpha \rangle = \frac{1}{4\pi} \int_0^{2\pi} \int_0^{\pi} \sin^3 \alpha \, d\alpha \, d\phi = \frac{2}{3}.$$

We substitute using the Thomson cross section $\sigma_T \equiv \frac{8\pi}{3} \frac{q^4}{m^2 c^4}$ ($\sim 6.65 \times 10^{-25}\,\mathrm{cm}^2$ for electrons), the energy density of the magnetic field $U_B = \frac{B^2}{8\pi}$, and $\beta \equiv \frac{v}{c}$ to get the average synchrotron power of

$$P_{syn} = \frac{4}{3} \sigma_T c \beta^2 \gamma^2 U_B. \tag{2.2}$$

In AGNs, the charged particles are usually assumed to be electrons accelerated to relativistic energies by the mass accretion into the supermassive black hole. The process by which this occurs is still unknown, however one prevailing theory is the Blandford–Znajek process, wherein magnetic field lines from currents in the surrounding disk thread a rotating black hole, inducing an electric potential [38]. By this explanation, the presence of these relativistic electrons nearer the AGN is expected, since synchrotron emission is the primary process of cooling of energetic charged particles which is assumed to take place as they travel outward within the lobes of radio galaxies.

2.3.1.2 Inverse-Compton Radiation

Compton scattering refers to the collision of photons with electrons. In the rest frame of the electron, the photon will always lose energy to the electron. In this frame, we can define the direction of the incoming photon along the x axis and all final momenta within the x-y plane without sacrificing generality. We can write the initial and final 4-momenta of the photon as

$$P_{\gamma 0} = \left(\frac{hc}{\lambda_0}, \frac{hc}{\lambda_0}, 0, 0\right) \qquad\qquad P_{\gamma 1} = \left(\frac{hc}{\lambda_1}, \frac{hc}{\lambda_1}\cos\theta, \frac{hc}{\lambda_1}\sin\theta, 0\right),$$

where λ_0 is the photon wavelength before scattering, λ_1 is the wavelength after scattering, h is Planck's constant, c is the speed of light, and θ is the angle between the incoming and outgoing photon propagation directions. We can write the initial and final 4-momenta of the electron as

$$P_{e0} = \left(mc^2, 0, 0, 0\right) \qquad\qquad P_{e1} = \left(mc^2, \ldots\right),$$

where m is the rest mass of the electron and the final momentum components can be ignored. Then, by using the conservation of 4-momentum, $P_{\gamma 0} + P_{e0} = P_{\gamma 1} + P_{e1}$, we can calculate

$$\begin{aligned}
\left(P_{\gamma 0} + P_{e0} - P_{\gamma 1}\right)^2 &= P_{e1}^2 \\
P_{\gamma 0}^2 + P_{\gamma 0}P_{e0} - P_{\gamma 0}P_{\gamma 1} + P_{e0}P_{\gamma 0} + P_{e0}^2 - P_{e0}P_{\gamma 1} + P_{\gamma 1}^2 - P_{\gamma 1}P_{\gamma 0} - P_{\gamma 1}P_{e0} &= P_{e1}^2 \\
P_{\gamma 1}^2 + P_{e0}^2 + P_{\gamma 1}^2 + 2P_{e0}\left(P_{\gamma 0} - P_{\gamma 1}\right) - 2P_{\gamma 0}P_{\gamma 1} &= P_{e1}^2 \\
m^2c^4 + 2\left(\frac{hmc^3}{\lambda_0} - \frac{hmc^3}{\lambda_1}\right) - \frac{2h^2c^2}{\lambda_0\lambda_1}(1-\cos\theta) &= m^2c^4 \\
mc\left(\frac{1}{\lambda_0} - \frac{1}{\lambda_1}\right) &= \frac{h}{\lambda_0\lambda_1}(1-\cos\theta),
\end{aligned}$$

which gives us Compton's scattering relation

$$\lambda_1 - \lambda_0 = \frac{h}{mc}(1-\cos\theta).$$

However, in a frame where the electron is not at rest, it is possible that the electron loses energy to the photon, thereby giving the photon an energy boost. This process is called inverse-Compton (IC) scattering. The power radiated through inverse-Compton by an isotropic distribution of electrons all with speed $v = \beta c$ scattering with an isotropic distribution of photons with energy density U_{ph} is given by

$$P_{IC} = \frac{4}{3}\sigma_T c\beta^2\gamma^2 U_{ph}.$$

The inverse-Compton process requires the presence of high energy electrons and a photon field, often called *seed photons* in the case of AGNs. Under the standard leptonic model of AGN radiation production, it is assumed that the electrons which are boosting photons are the same distribution of relativistic electrons which are emitting via the synchrotron process. For the seed photons in radio galaxies, there are three main fields that may contribute to inverse-Compton scattering: diffuse extragalactic background radiation (see Appendix A), starlight from the host galaxy, and photons created by local synchrotron radiation. When the seed photons are from local synchrotron radiation, the process is called *synchrotron self-Compton (SSC)*. Otherwise, it is called *external Compton (EC)*. SSC is the most common model attributed to blazar emission, as, for example, with Markarian 421 whose SED is shown in Fig. 2.3. EC is the most common for radio galaxy emission, however, FSRQs also require a EC component.

2.3.2 Hadronic

In addition to leptonic emission, γ rays can be produced via hadronic processes as well. These require the presence of relativistic protons. The three main hadronic processes which produce γ rays are photohadronic, in which protons interact with lower-energy photons to produce pair cascades resulting in pions; hadronuclear, in which protons collide with other protons or nuclei to produce pions as shown in Figure 2.4; and direct synchrotron radiation of protons. Charged and neutral pions emerging from the first two interactions cascade and produce neutrinos and γ rays in their decay chain.

The relativistic jets of AGNs are composed of leptons and hadrons. If the system is capable of channeling enough power into accelerating protons to relativistic energies, then hadronic interactions may also contribute to the emitted electromagnetic radiation. Most blazar broadband spectra have been so far successfully modeled in the context of a leptonic scenario. However, it may be possible to fit a spectrum with either scenario. For example, the broadband SED shown in Fig. 2.5 shows the same data as is shown in Fig. 2.3 but fit to a hadronic model instead of a leptonic.

Models requiring contributions from hadronic emission have been proposed by several authors, legitimately assuming that at least some fraction of the hadrons may be accelerated along with the electrons. Protons undergoing hadronuclear collisions in the vicinity of the black hole are predicted in, e.g., AGN core models [39–41], while the strong shocks thought to be present in the relativistic jets offer another ideal environment for accelerating protons [42]. In AGN jets where there are sufficient lower-energy photons present, especially in the UV band from the accretion disk, photo-hadronic processes are thought to be the dominant interaction for possible hadronic γ-ray emission, with some contribution possible from proton synchrotron emission as well [43]. In the lobes of radio galaxies, where the lower-energy photon fields originating from jet activity and the accretion disk are decreased due to a much greater distance, the dominant potential hadronic process is thought to be from proton-proton collisions, for example with surrounding gas

---

[2] `https://www.hawc-observatory.org/science/cosmicrays.php`

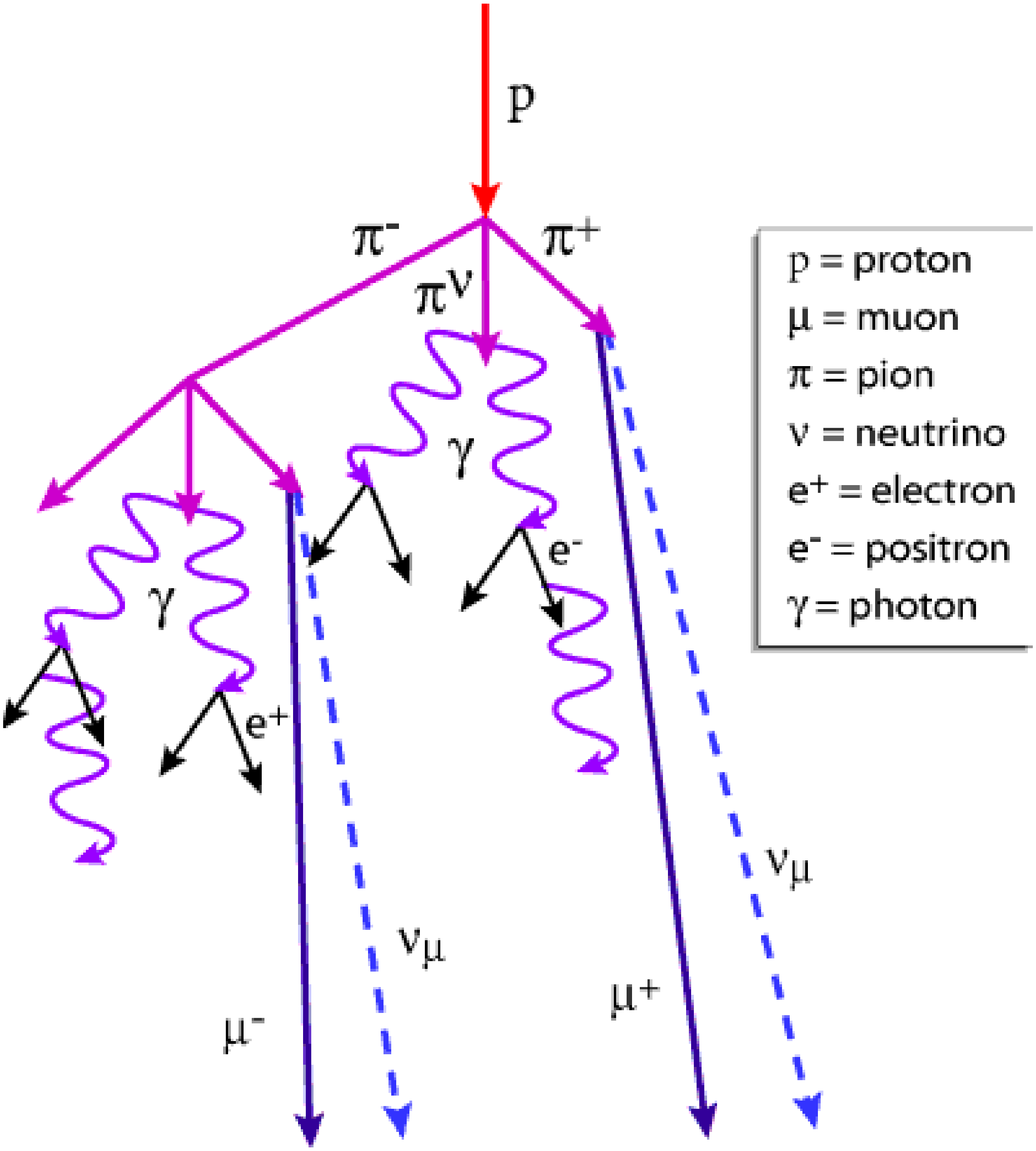

Figure 2.4: Example particle cascade from a proton colliding with a nucleus. Notably, γ-ray photons and neutrinos may be produced.[2]

or plasma nuclei [44, 45].

The "smoking gun" signature of hadronic emission from AGNs is the observation of neutrino emission. While photon emission, including γ rays, may be produced in other processes rather than the hadronic one, neutrinos are not produced in leptonic processes, and thus constitute a unique tracer of hadronic processes. Neutrinos are always a product of charged pion decay. If proton-proton collisions are producing neutral pions, they must also be producing charged pions. Therefore, neutrinos must be produced alongside the process of hadronic γ-ray emission originating from proton-proton collisions. In September 2017, an astrophysical muon neutrino was detected by the IceCube Neutrino Observatory at the South Pole whose origin was found to spatially coincide with a blazar in a flaring state, TXS 0506+056 [46]. The combined significance of the spatial and temporal coincidence of the flaring blazar and the neutrino was estimated at the 3σ level. Assuming the neutrino originated from the blazar, this joint detection would be definitive evidence that an AGN is creating cosmic-ray protons, and that it is creating γ rays via hadronic processes.

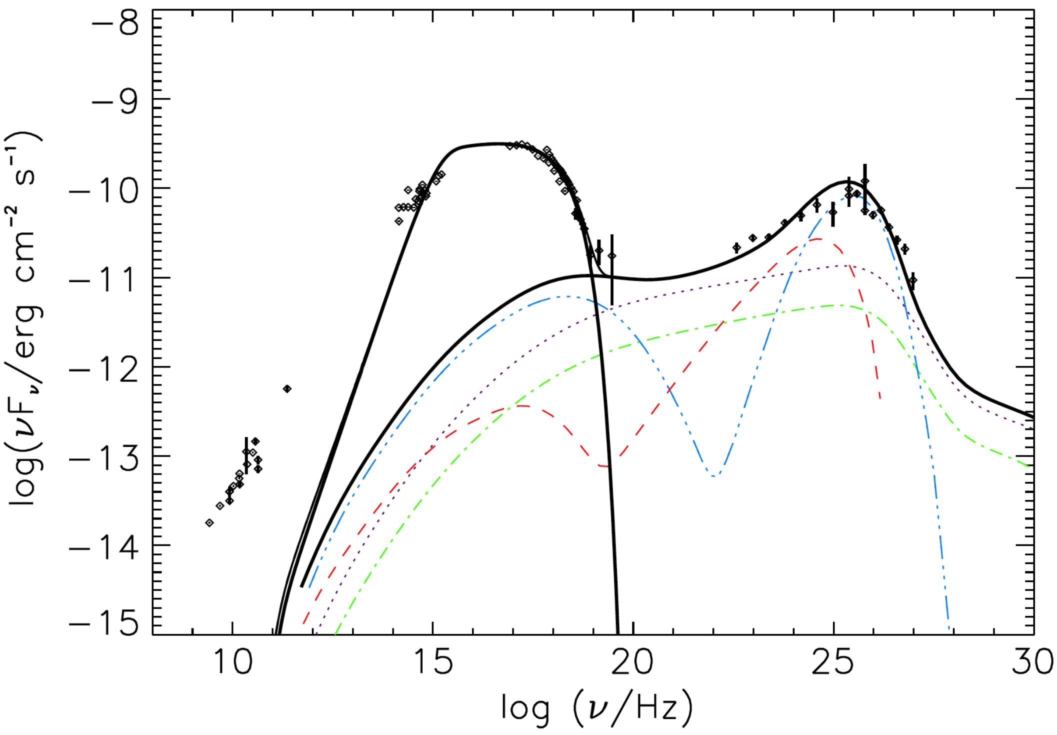

Figure 2.5: Broadband spectrum of bright blazar Mrk 421 showing a hadronic model of the high-energy bump with the low-energy bump modeled with electron synchrotron emission. The neutral pion cascade component is shown in the purple dotted line, the charged pion cascade is shown in the green dashed-dotted line, the muon synchrotron and cascade is shown in the blue triple-dot-dashed line, the proton synchrotron and cascade is shown in the red dashed line, and the sum of all components is shown in the black solid line. Note the significant difference between this and the leptonic model in Fig. 2.3 in the MeV energy band. [4]

Chapter 3: *Fermi* Large Area Telescope (LAT)

3.1 Overview

The LAT is one of two instruments onboard the *Fermi* Gamma-ray Space Telescope, the other being the Gamma-ray Burst Monitor (GBM). The *Fermi* satellite operates in orbit around the Earth where it can observe without being hindered by Earth's atmosphere. In low Earth orbit, it can obtain a fresh glimpse of the γ-ray sky every 90 minutes. The LAT detects and analyzes individual γ-ray photons in energies between tens of MeV and hundreds of GeV [5]. The LAT is a pair-conversion telescope, which means it detects γ rays by creating an environment conducive for photons to interact with protons, an interaction which then creates electron-positron pairs. It is these pairs which are truly detected, providing information about the photon's energy, propagation direction, and arrival time. This functionality is obtained with contributions from three components all shown in Fig. 3.1, the Tracker (TKR), the Calorimeter (CAL), and the Anti-Coincidence Detector (ACD).

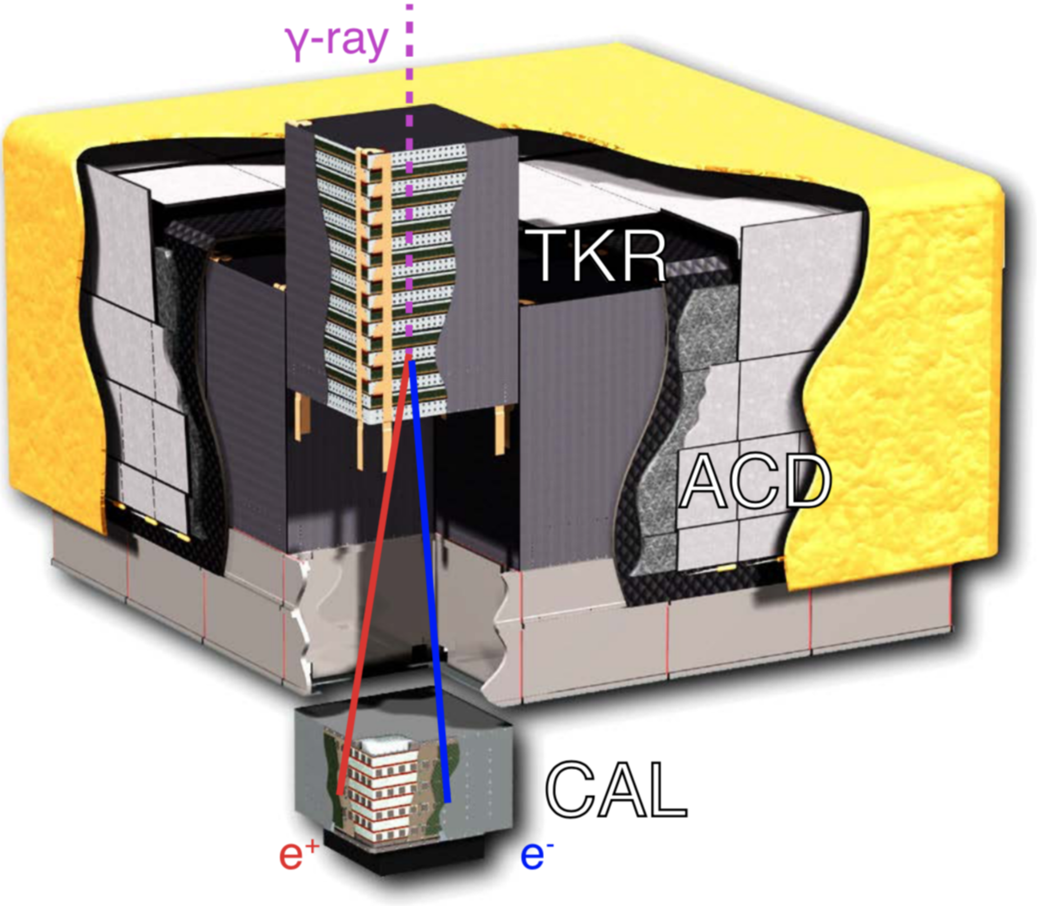

Figure 3.1: Cutaway of the LAT showing an example path of a γ ray converting into an electron-positron pair. [5]

3.2 Instrument

3.2.1 Tracker (TKR)

Information in this section was gathered from the Tracker design paper [7].

The Tracker contains 16 towers of 19 trays. Each tray can hold silicon strip detectors (SSDs), tungsten foil, and readout electronics. The Tracker's primary purpose is to measure the direction of the incident γ ray. The tungsten has a high atomic number (74) which gives it the higher cross-section for interaction of its nuclei with incoming γ rays needed to produce the traceable electron-positron pairs. These pairs then create signals in the SSDs, which allow their paths to be traced, or *tracked*. These paths can be reconstructed to provide the direction of the original incoming γ-ray photon.

SSDs operate with a series of p–n junctions aligned into long strips. A reverse bias voltage is applied to the junctions, increasing the size of the depletion region so that only negligible current can flow. The p–n junction naturally creates a stable electric field within the depletion region which pulls any free electrons towards the n side and any free holes towards the p side. A high energy charged particle (electron or positron as created by the original incoming γ ray) will separate electrons in the depletion region away from their atoms, creating free electrons and holes along its path. These free holes will be pulled by the electric field to the nearest p strip, creating a small current signal. This process is shown in Fig. 3.2.

Each tower consists of layers of tungsten, single-sided SSDs oriented along the x direction, single-sided SSDs oriented orthogonally along the y direction, and structural

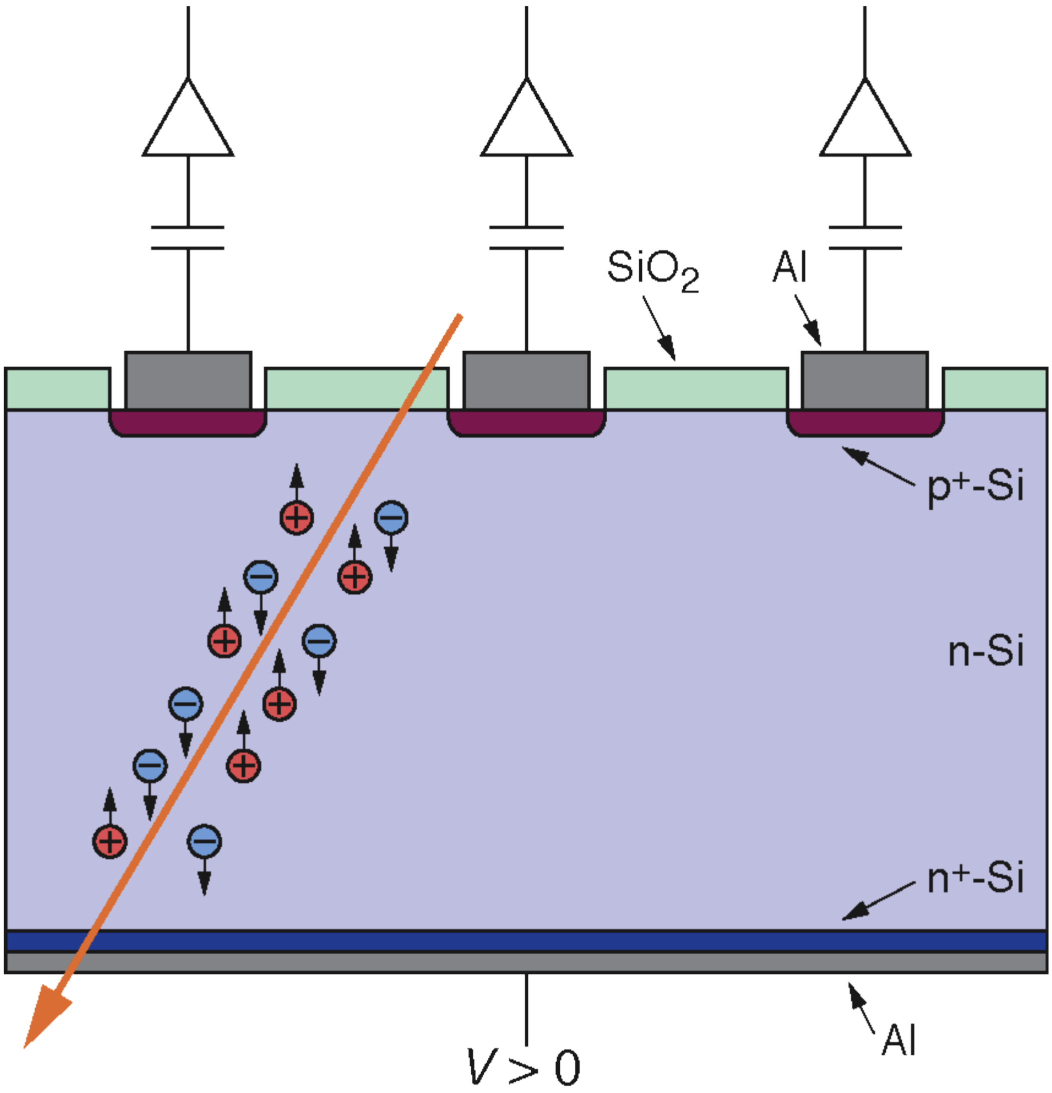

Figure 3.2: Side view diagram showing a charged particle traveling through the active depletion region of an SSD. The depletion region is increased with a reverse bias, wherein the n side is held at a greater electric potential than the p side. [6]

material as shown in Fig. 3.3. The use of layered SSDs oriented orthogonally allows for full detection of the position of the particles within the plane of the SSDs. In the top twelve layers (“Front”), the tungsten conversion foils are thin, with a thickness of 0.095 mm. Four of the bottom layers (“Back”), contain foils which are thick, with a thickness of 0.72 mm, and three trays have no foil. This was done to reduce multiple scatterings in lower energy γ rays while providing sufficient opportunity for conversion of higher energy γ rays. These towers fully assembled are shown in Fig. 3.4. In contrast to the Calorimeter, the Tracker is not designed to stop as many particles as possible, but to convert the γ rays into pairs, producing a simple track so that the direction of the original γ-ray can be determined.

3.2.2 Calorimeter (CAL)

Information in this section was gathered from the LAT description paper [5]. See also the Calorimeter paper for more details [47].

The Calorimeter’s primary purpose is to measure the energy of the incident γ ray. It absorbs the electron-positron pair, along with any additional secondary particles, using the scintillating material crystalline thallium-activated cesium iodide, CsI(Tl). The crystals are shaped into long rods with square cross section as shown in Fig. 3.5. Bound electrons in the CsI(Tl) are boosted into excited states by the incoming radiation, then drop back into lower energy states and release a photon via spontaneous emission. Most of the light emitted by the CsI(Tl) is trapped within the crystal and propagates to the end of the rod. That emission has a maximum emission wavelength in the green around 550 nm, making

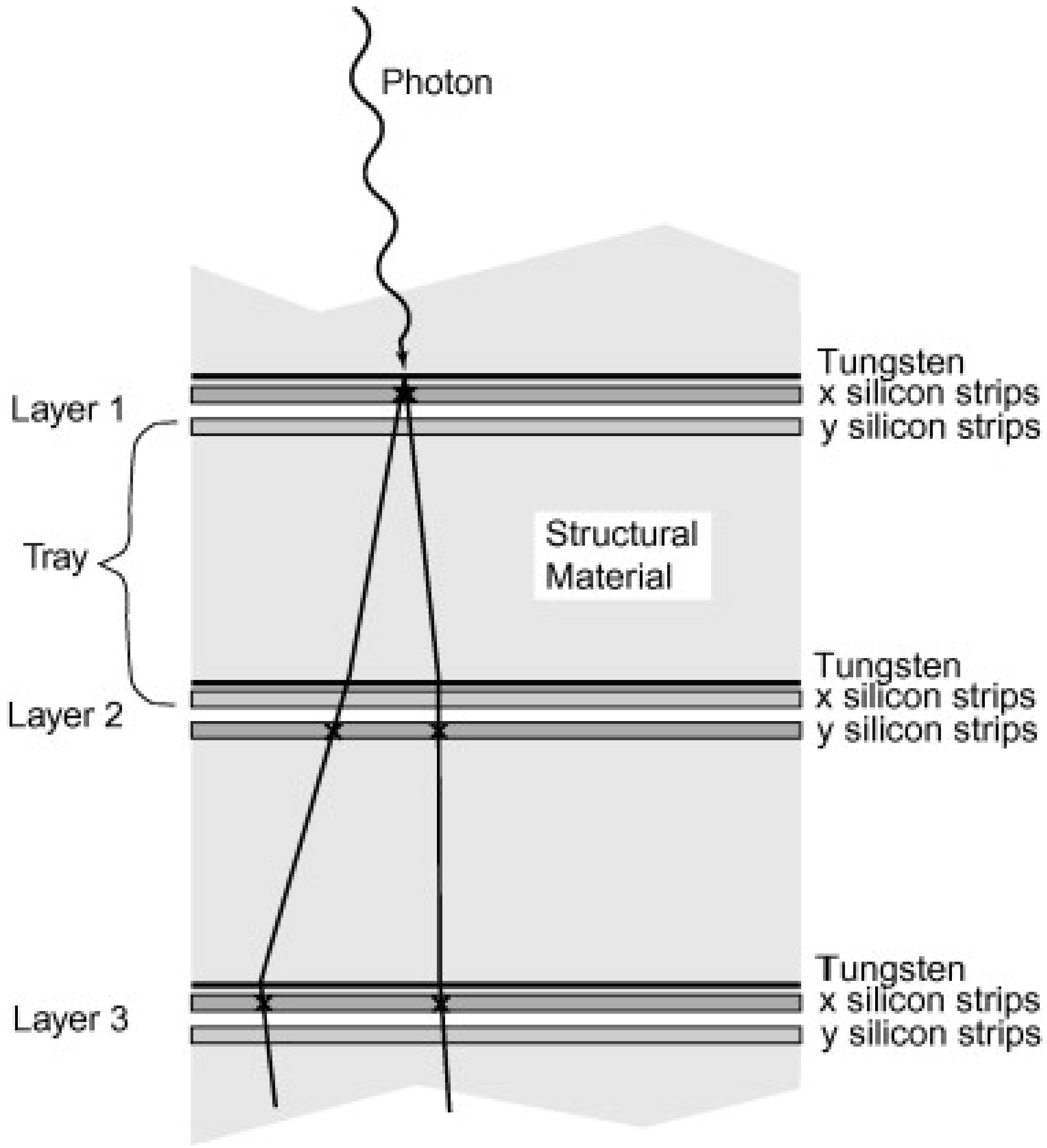

Figure 3.3: Side view diagram of a Tracker tower showing the arrangement of layers [7].

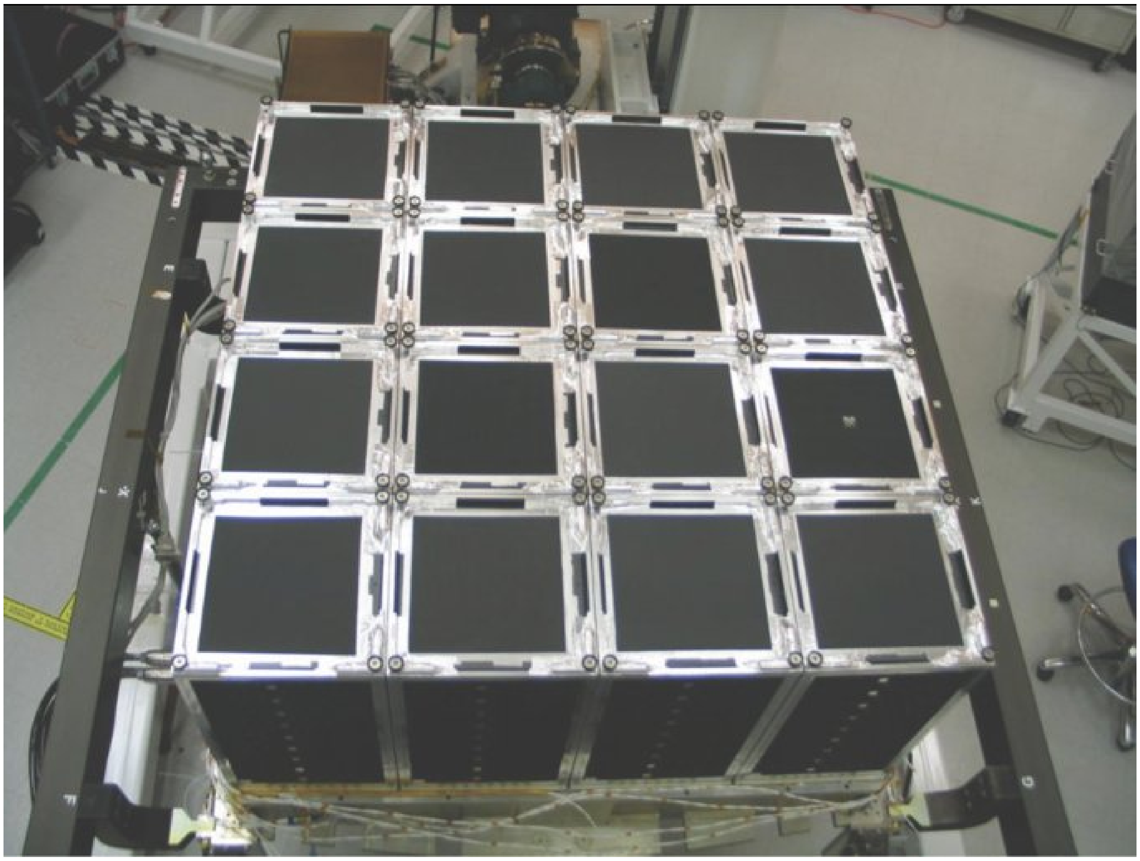

Figure 3.4: Fully assembled Tracker instrument showing the 16 towers [5].

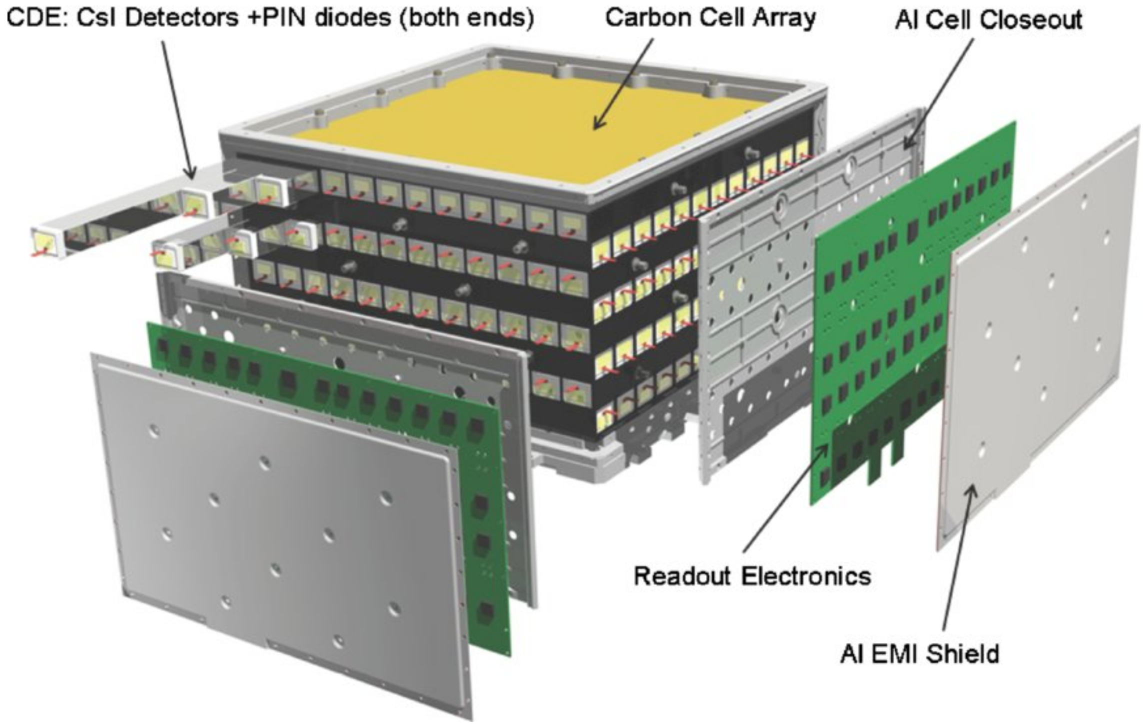

Figure 3.5: Exploded view of the Calorimeter, showing alternating orientations of the CsI(Tl) crystal elements, each with a photodiode attached to both ends [5].

it easy to detect using a photodiode on both ends of each crystal. CsI(Tl) is a good choice for the Calorimeter because it has a high light yield, high density, and high atomic number which increases the probability of interaction with incoming radiation. It is therefore good at stopping most particles so they are detected and not lost. By capturing the entire shower, we can measure the full energy of the original γ ray. With its crystals oriented in alternating orthogonal directions as shown in Fig. 3.5, some spatial information and thus imaging can be obtained of the particle shower, allowing for further constraints on the energy.

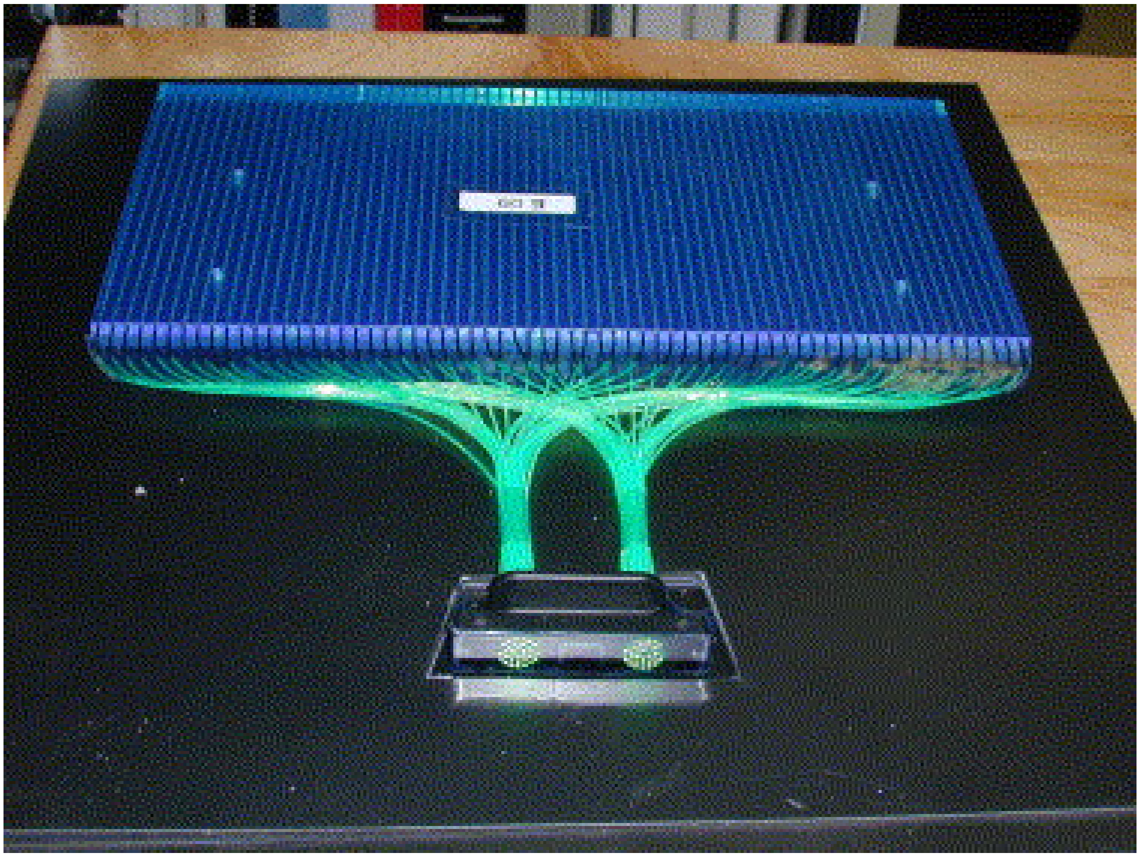

Figure 3.6: Photograph of a single plastic scintillating ACD tile showing embedded wavelength shifting (WLS) fibers to collect signal light bundled into two clusters for detection by two photomultiplier tubes [8].

3.2.3 Anti-Coincidence Detector (ACD)

Information in this section was gathered from the ACD paper [8].

The primary purpose of the ACD is to detect charged cosmic rays and provide a veto to the rest of the LAT for such non-photon background events. This is crucial, since the event rate for cosmic rays is significantly greater than the event rate of signal γ rays. The ACD works by surrounding the LAT on 5 sides in 89 plastic scintillator tiles. As shown in Fig. 3.6, embedded into the tiles are 1 mm diameter WLS optical fibers. The plastic scintillators are optimized to emit light in the violet–blue, and this light then causes the WLS fibers, which are designed to fluoresce with green light when exposed to blue light, to fluoresce within the fiber core. A fraction of this green light with sufficiently small incidence angle relative to the longitudinal direction of the fiber is trapped by total internal reflection of the fiber. These fibers are fed to the bottom of the LAT where two bundles from each tile are each coupled to a photomultiplier tube (PMT) for detection. The PMTs and readout electronics for the ACD are positioned there so they are out of the way of incoming radiation.

The ACD tiles are designed and positioned for the smallest gaps and leakage possible. To that end, the ACD tiles are overlapping in the optimized pattern as shown in Fig. 3.7. In addition, there are 8 flexible scintillating fiber ribbons underneath the tiles along the edges of the tiles to further decrease gaps and leakage.

The choice of plastic scintillators as a detection mechanism for cosmic rays but not for γ rays is good because HE γ rays naturally penetrate matter unless the density and atomic number (Z) are sufficiently high. The plastic scintillators have very good cross section for fluorescing by other radiation, but are not dense enough or high enough in Z to interact with γ rays. Thus, they carry out their role of detecting background while not obstructing incoming γ rays.

The LAT's ACD offered a large improvement over the ACD of its predecessor, EGRET. From the EGRET experiment with its single channel ACD and no spatial information, it was learned that HE events would frequently create showers within the detector with some of the charged particles reversing direction and traveling back up through the ACD, thus creating a false veto. This phenomenon is called *backsplash*, and an example

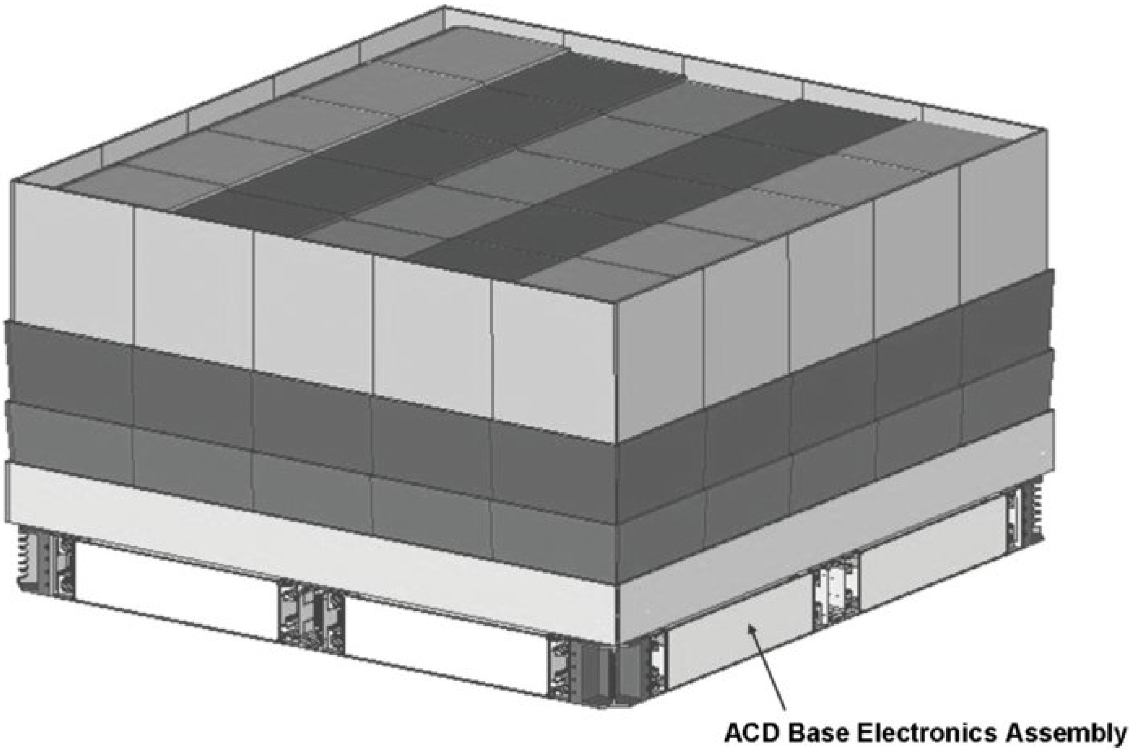

Figure 3.7: Diagram of the ACD tiles, showing overlapping tile positioning pattern and location of the ACD PMTs and electronics [5].

event from simulation is shown in Fig. 3.8. By segmenting the ACD on *Fermi*, it becomes possible to identify such backsplash events by comparing the reconstructed direction and position to the location of the ACD tile(s) that was(were) triggered.

3.2.4 Uncertainties

The LAT is a one-at-a-time high energy particle detector in space. Using its three primary instruments collectively, it reconstructs as much information as possible about each individual incoming γ-ray photon. This process of measurement and reconstruction has only limited effectiveness, which means the direction and energy of the γ ray comes with statistical and systematic uncertainties determined by many factors, such as the detector design, the direction and energy of the γ ray, as well as random specifics about the event like where the pair conversion occurred. The probability distribution of energies for a given measurement is called energy dispersion, and the probability distribution of the 2-dimensional direction is called the point spread function (PSF).

An idealized, infinitesimally small source of light, when observed by the detector, will appear smoothed out into a larger shape roughly in a 2-D Gaussian distribution[3]. The PSF is this shape, a point source as observed by the detector. The PSF is particularly important to spatial studies with γ rays, and therefore plays a significant role in this work.

---

[2] `http://www.slac.stanford.edu/exp/glast/groups/canda/lat_Performance.htm`

[3] The exact form of the PSF is a double Moffat distribution [48], each which has the basic functional form

$$I(r) = I_0\left(1 + (r/R)^2\right)^{-\beta}. \tag{3.1}$$

For more details, visit `https://fermi.gsfc.nasa.gov/ssc/data/analysis/documentation/Cicerone/Cicerone_LAT_IRFs/IRF_PSF.html`

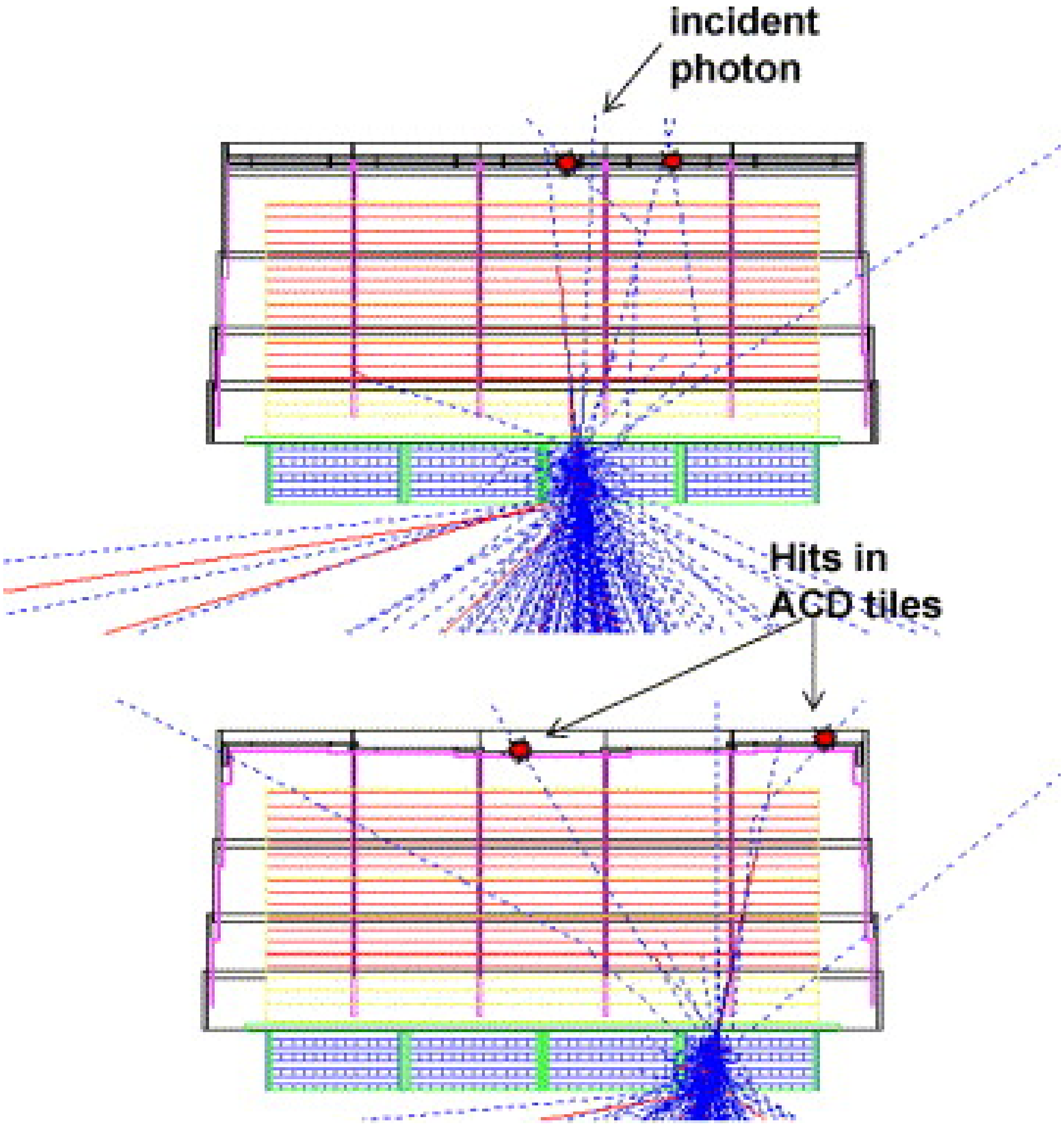

Figure 3.8: Showing two examples of simulated backsplash events in the LAT. Red lines indicate charged particles and blue lines indicated photons [8].

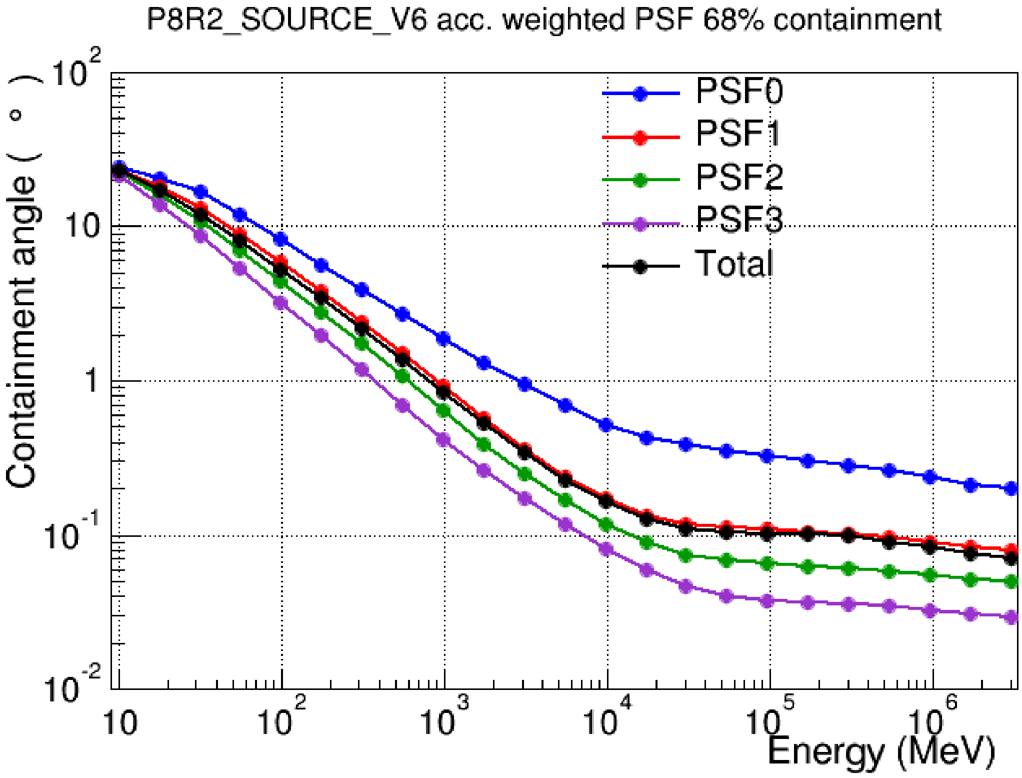

Figure 3.9: 68% containment PSF of the LAT with the latest Pass 8 dataset, as derived from Monte Carlo simulations. Also shown are the containment angles for each of the divided PSF event type quartiles.[2]

The LAT PSF is relatively large when compared with many other astronomical telescopes, which creates the problem of *source confusion*, when nearby source signals blur out spatially enough that they become difficult to distinguish. The LAT PSF is energy dependent, decreasing significantly with greater energy, as shown in Figure 3.9.

3.3 LAT Data

The process of turning all of the raw data from the LAT's sensors into γ-ray photon data is called event reconstruction. This reconstructed photon data is publicly available in Flexible Image Transport System (FITS) format from the LAT Data Server[4] on the *Fermi* Science Support Center (FSSC), hosted by NASA Goddard Space Flight Center. The LAT Data Server provides γ-ray data in real time, with a typical delay of only about 4–5 hours from the time of onboard detection, depending on the status of the LAT and the communications network, the Tracking and Data Relay Satellite System (TDRSS). The data is automatically processed at a computer cluster at the SLAC facility in Menlo Park, CA, and each data run (i.e., data taken during one 90-minute orbit) goes through a series of checks for quality and potential instrument malfunctions and is inspected and approved by a human being on call.

In its simplest form ("photon data"), this high-level representation of the data consists of a list of photon events, with each entry containing basic information about the individual photon, primarily its energy, its originating sky position, and the time it was observed. It also contains a few pieces of secondary information, notably four angles de-

---

[4] `https://fermi.gsfc.nasa.gov/ssc/data/access/`

scribed in the next paragraph. These data FITS files containing photon events are called FT1 files.

The angles provided are θ, the angle between the incident direction and a line normal to the top surface of the LAT, ϕ, the angle between the incident direction and a line normal to the sun-facing side of the spacecraft, the zenith angle, measured between the incident direction and a line passing through the center of the Earth and the spacecraft, and the Earth azimuthal angle, indicating the second coordinate for the complete origination position on the Earth. The most important of these for this work is the zenith angle, which can be used to quickly cut out potential γ rays which have terrestrial origin.

Each photon is also classified by its probability of being a photon (as opposed to non-photon background, such as cosmic rays) and the quality of its reconstruction. The classifications based on probability of being a photon, called “event class”, are named, in order of increasing probability, Transient, Source, Clean, and Ultraclean. In this order, each of these event classes contain all events in the one following. All of the LAT analysis in this work was done using data from the Source class, recommended for source analysis and providing a good balance of sensitivity and suppressed background. The photons are also classified into “event types” according to the specifics and quality of the reconstruction. Prior to the release of Pass 8 (see Sect. 3.3.1), there were two event types, Front and Back, referring to the location in the Tracker (see Sect. 3.2.1) where the photons were converted into electron-positron pairs. Events converted in the Front, where the tungsten conversion foil is thinner, generally have better reconstruction and thus angular resolution than those converted in the Back.

Finally, another form of data required for analysis (and also available from LAT

Data Server) are spacecraft files, also known as FT2 files. These files come in FITS format, and they describe the position and orientation of the *Fermi* Gamma-ray Space Telescope as a function of time. This information is necessary to calculate the LAT's exposure. The FT2 also includes information about time periods when the spacecraft was in a favorable condition to take data (e.g., when not in a place of its orbit with known regions of high background flux, such as the South Atlantic Anomaly), called Good Time Intervals (GTIs). These GTIs can be used to quickly cut out bad photon data from the FT1 based on their detection times.

3.3.1 Pass 8

The LAT event reconstruction process has evolved over time since well before *Fermi*'s launch in 2008 in a series of iterations called "Passes". With each new pass release, all of the raw data (i.e., the full dump of readouts from every sensor and detector) prior to its release are reprocessed as well. From the time of launch until August 2011, Pass 6 was used to process the data. Pass 7 followed it, which took advantage of improved calibration that was possible with data from years of real operations. Next, Pass 7 reprocessed was released which used up-to-date calibration constants, mainly resulting in an improvement to the PSF [49]. Finally, Pass 8, released in June 2015, was the result of a major overhaul in the entire analysis chain. Whereas Pass 7 and Pass 7 reprocessed were primarily an improvement of the calibration resulting in a reduction of the systematic uncertainties, Pass 8 marked the first improvements made to the event-level reconstruction from the ground up.

Pass 8 changed the processing in several key areas. It alleviated the problem of instrumental pile-up, called "ghost events". This occurs when remnants of electronic signals from events a few μs prior appear as a background for events immediately following. It adopted a new tree-based pattern recognition algorithm, replacing the prior combinatoric algorithm, which does not depend on information from the calorimeter and is less sensitive to track-confusion from backsplash (see Sect. 3.2.3). A new clustering stage was added during reconstruction from calorimeter data, which allows for separately identifying ghost signals from proper signals. The calorimeter energy reconstruction was reworked, reducing the effects of crystal saturation, when signals exceed the dynamic range of the readout electronics. This is achieved by recovering some of this lost information with information from nearby crystals that are not being saturated. Pass 8 included an improved algorithm for using particle tracks with ACD tile information. Also, boosted decision trees were employed for an improvement in separating classifications of photons and cosmic rays [50]. These changes led to a significantly improved effective area, acceptance, and PSF at all energies.

Another new feature relevant to this work that was introduced with Pass 8 was the expansion of photon event types. Because the photon reconstruction can be different for different events, some photons can be much better constrained in space and energy than others, all else being equal. By lumping all photons together as an average, we lose a lot of information from certain photons that could contribute much more from their better tracking. In the ideal case, we would perform analysis with every photon each with its own PSF and energy containment. Unfortunately, because of limitations in computation, this quickly becomes impractical. However, with the expansion of event types in Pass 8, photon events are categorized into four quartiles based on the quality of the reconstruction, with each quartile containing equal numbers of events. With this setup, the analysis can be performed with reasonable computation while using much more of the individual photon information. One can select only the best-constrained quartile of photons, or, as was done in this work, one can still use all photons in summation while treating each quartile with its own unique instrument response function (IRF), thereby extracting the maximum information possible from the data. In addition to the existing event types from Pass 6 and 7, Front and Back, selection of event types PSF0–3 and EDISP0–3 became possible, with 0 being the worst quartile in PSF and energy dispersion, and 3 being the best. See Fig. 3.9 for a comparison of the Pass 8 PSF quartiles.

3.4 LAT Analysis

3.4.1 Basics

Most astronomical observations of electromagnetic radiation flux are done using aperture photometry. This is done by defining a hard cut region of the sky with size according to the PSF and summing the total counts observed within it. Then, to estimate the background level for subtraction, the surrounding regions without visible sources are observed in the same way. This technique is rarely possible with the LAT, apart from observations of very bright transients. As mentioned in Sect. 3.1, the large PSF of the LAT causes source confusion, wherein individual photons can often be roughly equally probable of originating from two or more source sky locations. Also, signal from most persistent γ-ray sources end up appearing only barely above the background (whether from galactic interstellar emission or isotropic γ-ray background). For these reasons, analysis with LAT data requires careful statistical treatment starting by fitting the data to a model of not just the source of interest (SOI), but all sources in a region at least 1–2 PSF lengths away (using the largest PSF possible in the analysis to be conservative). This region is called the region of interest (ROI), and is typically at least $10^\circ \times 10^\circ$ in size and centered at the SOI. The ROI model is defined in an Extensible Markup Language (XML) formatted file with all sources within the ROI and their properties. The XML model can be constructed by hand or, more conveniently, by script. One notable script is `make3FGLxml`, authored and maintained by Tyrel Johnson and available on the FSSC[5], which generates an XML model from the *Fermi*-LAT Third Source Catalog (3FGL) [34].

There are two basic modes of performing LAT analysis, unbinned and binned. In unbinned mode, all events are carried through and treated in the analysis, with all individual data about each photon intact. In binned mode, the events are initially binned both in spatial direction and energy, thereby reducing the resolution of this information to the size of the bins. Unbinned analysis is always more accurate, however since in unbinned mode the computation time scales as the number of photon events, it is usually much more intensive and slow when compared to binned analysis. Binned mode, on the other hand, only scales as the number of bins, so unbinned only has the potential to be as fast as binned when there are fewer events than the number of bins there would be in binned mode. Because of the enormous savings in computation, binned analysis is always the preferred method for data taken from more than a few days or so of observing, and the loss of information by binning is minimal when the spatial and energy bins are chosen to

---

[5] `https://fermi.gsfc.nasa.gov/ssc/data/analysis/user/`

be smaller than the PSF and energy dispersion, respectively. All of the LAT analysis in this work was done using binned mode, and all further descriptions of the analysis here assume binned mode.

Typically, analysis of LAT data then proceeds by making use of the *Fermi* Science Tools[6] software package. These tools provide all of the low-level functionality needed to do analysis. First, the `gtselect` tool is used to make the primary cuts on the data, such as the selection of events contained within the spatial ROI, within a specified time interval, within a specified energy range, having less than a specified maximum zenith angle, and having specified event classes and types. Next, the tool `gtmktime` is used to select data only during GTIs. The `gtbin` tool is then used to bin the data in both direction and energy, generating a counts cube (i.e., count maps across energy bands). Three derivative data files needed for the analysis are then computed from the model and the resulting reduced FT1 and FT2 files: the integrated livetime as a function of sky position and off-axis angle via `gtltcube`, the exposure map from the livetime cube via `gtexpcube2`, and finally the source map generated from convolving the model with the instrument response via `gtsrcmaps`. With a model of all sources in the ROI at hand, we can generate a model map using the `gtmodel` tool. The model map is a full grid of predicted counts, represented as the LAT data would be through convolution with the IRF.

3.4.2 `fermipy`

In the process of using the low-level Science Tools to do LAT analysis, one usually ends up scripting the repetitive tasks. After a while, every scientist often ends up using

---

[6] `https://fermi.gsfc.nasa.gov/ssc/data/analysis/software/`

either their own personal set of higher-level scripts to facilitate the analysis or a collection of borrowed scripts from someone else. Built on top of the Science Tools, `fermipy`[7] is an open source collaborative coding project in Python which attempts to unite these individual efforts into a single usable set of high-level LAT analysis scripts [51]. `fermipy` was utilized for both the Cen A core (see Chapter 5) and Cen A lobes (see Chapter 6) projects in this thesis.

In addition to offering scripts to expedite existing tools, `fermipy` brings important new algorithms to the analysis process. In particular, the `optimize` method proves an invaluable tool for fitting an ROI containing a large number of sources and parameters. On its own, the fitting functionality in the Science Tools is quite limited in the number of parameters that can be fit simultaneously by the fitting algorithm, usually Minuit [52] or similar. `optimize` provides an alternative solution by iteratively freeing key sources and parameters in the model in a sensible order, most significantly detected sources first, and then running the fit in each case. This allows for the convergence of a whole potentially large and complex ROI to its maximum likelihood while keeping the number of free parameters given to the fitting algorithms low.

Another key feature provided with `fermipy` is the `find_sources` method which quickly and iteratively searches for and adds point sources to the model which are detected to be missing from the existing model. This works by first creating a test statistic (TS) map. A TS map is a spatial map of the region where each pixel is made by adding a new putative point source to the model at that location and fitting the model to check the change in likelihood caused by its inclusion. The name “TS map” comes from the value

---

[7] `http://fermipy.readthedocs.io/en/latest/index.html`

mapped at each location being the TS of the existence of a point source there. The TS map is a great tool for locating spots in the model which underpredict γ-ray emission in the form that is fit well by a point source. `find_sources` uses peaks in this TS map to add the most probable missing sources.

In addition, `fermipy` offers tools for spatial extension fitting and faster creation of residual and TS maps to check for how well the model fits the data, all of which are not available from the Science Tools.

Primary original feature contributions to the `fermipy` project consisted of improvements made to the light curve creation script, `GTAnalysis.lightcurve`. An approach to the calculation of flux variability was added, which could not easily be done prior. See Appendix C for details. Other contributions to `fermipy` include some minor improvements to `optimize`, including the option to skip optimization of certain sources as well as other developments in the fitting logic. Additions to the plotting scripts, including code to generate histograms from residual maps, were incorporated. These were broadly useful in all of the analyses of this thesis utilizing `fermipy`. Finally, several other small contributions were made fixing bugs throughout the code. [8]

---

[8] `https://github.com/fermiPy/fermipy/pulls?utf8=%E2%9C%93&q=is%3Apr+author%3Ajefemagril`

Chapter 4: Fornax A

The work described in this chapter is published in an article in The Astrophysical Journal [1]. It has been included it here, edited for clarity for its inclusion into the thesis. The study follows work from William McConville [10], who is also a contact author for the paper.

4.1 Introduction

The radio galaxy Fornax A, well known for its radio lobes spanning $\sim 50'$, with a lobe-to-lobe separation of $\sim 33'$ [15], is one of the closest and brightest radio galaxies, located at a distance of only 18.6 Mpc [53]. Hosted by the elliptical galaxy NGC 1316, the radio source contains a low-ionization nuclear emission-line region nucleus, which has been imaged to arcsecond-scale resolution and features a flat spectrum ($\alpha = 0.4$; $S_\nu \propto \nu^{-\alpha}$) core with dual-opposing "s"-shaped jets that are detected out to $\sim$ 5 kpc from the core [54]. The radio lobes are characterized by a complex polarized filamentary structure with no observable hotspots [9].

Fornax A was the first radio galaxy reported to emit diffuse, non-thermal X-ray emission from within its radio lobes from observations with ROSAT [21] and ASCA [55], which were later confirmed through dedicated observations of the east lobe with *XMM*-

Newton [18] and the west lobe with *Suzaku* [56]. The non-thermal X-rays have been widely attributed to IC emission of relativistic electrons scattering on cosmic microwave background (CMB) photons, with the same population of relativistic electrons producing both synchrotron and IC emission [57]. To date, similar leptonic IC/CMB emission has been detected in X-rays from tens of extended lobes in radio galaxies and quasars. In general, such detections imply that the ratio of relativistic electron pressure to magnetic field pressure within the lobes is $\sim$ 1–100 [58–60]. More recently, a detection of thermal emission was reported from the western lobe of Fornax A using combined *Suzaku* and *XMM-Newton* data [61]. Thermal emission in the lobes of a radio galaxy is typically not seen, although evidence for this has also been reported in the giant lobes of the nearby radio galaxy Centaurus A [62, 63].

Motivated by the observed (and presumed IC/CMB) X-ray emission from the lobes of Fornax A, it was predicted that the high-energy tail of the IC/CMB would be detected by the *Fermi*-LAT [5] at $> 100\,\mathrm{MeV}$ [64]. Following this, it was predicted that the lobes would also be detected in γ rays at higher energies by the LAT due to IC upscattering of the infrared and optical extragalactic background light (EBL) photons, analogous to the CMB photons upscattered to X-ray energies [11]. The association of Fornax A with the *Fermi*-LAT second year catalog (hereafter 2FGL) [65] source 2FGL J0322.4−3717 thus raised an important question regarding the origin of the γ-ray source, which at the time had no evidence presented for significant extension. In particular, a distinction between emission arising from the lobes and possible contamination from the central core region could not be established from the γ-ray data alone, although X-ray and radio observations [66] suggested that the contribution from the core was likely to be minimal. Previous attempts to search for spatial extension with 44 months of Pass 7 LAT data yielded only a marginal indication at the $\sim 2\sigma$ level, and attempts to distinguish between core and lobes with γ rays was unsuccessful [10]. This was likely due to insufficient exposure time and the reduced spatial sensitivity of Pass 7 compared to Pass 8.

In a recent study [44], the spectrum of the Fornax A lobes was modeled in multiple wavelengths using both leptonic and hadronic production scenarios without knowledge of γ-ray spatial extent or γ-ray contamination from the galaxy core. They concluded the most likely source of γ-ray production is hadronic processes within filamentary structures of the lobes. Our study follows the successful γ-ray detection of the extended lobes from Centaurus A [25], and LAT studies of the lobes of NGC 6251 [67] and Centaurus B [68]. Gamma-ray upper limits using High Energy Stereoscopic System (H.E.S.S.) and *Fermi*-LAT observations have been used to constrain the hadronic cosmic-ray population within the radio lobes of Hydra A [69].

Fornax A is not associated with a γ-ray source in the most recent, third *Fermi*-LAT catalog based on four years of LAT data [34, 35]. However, the centroid of the source 3FGL J0322.5−3721 is offset by $0^{\circ}.15$ from the core of Fornax A. This offset is greater than the 95% position uncertainty of the 3FGL source. In the following we discuss possible reasons for this offset, detail a significant γ-ray detection of extended emission from Fornax A using 6.1 years of *Fermi*-LAT data, and present modeling under leptonic and hadronic scenarios. Detecting extended emission from Fornax A with the LAT is challenging because the 68% containment PSF radius is $\sim 0^{\circ}.8$ at 1 GeV, which is larger than the Fornax A lobe-to-lobe separation. The LAT PSF is energy dependent going from

5° at 100 MeV to 0.°1 at 100 GeV with 68% confidence[1] (see Fig. 3.9).

4.2 Observations & Analysis

4.2.1 *Fermi*-LAT Observations

Unlike all studies mentioned in Section 4.1, we used 6.1 years (from 2008 August 4 to 2014 September 4) of Pass 8 LAT data. Compared to previous iterations of the LAT event-level analysis, Pass 8 provides greater acceptance and improved PSF [50] (see Sect. 3.3.1). These factors allowed for a firm detection of extension of Fornax A. We selected from all-sky survey data at energies from 0.1 to 300 GeV extracted from a ROI with 10° radius centered at the J2000.0 radio position of Fornax A (R.A. = 50.°673, Decl. = −37.°208) [54]. We used the "source" event class, recommended for individual source analysis, a zenith angle limit of 100° to greatly reduce contamination from the Earth limb, and a rocking angle limit of 52° (see Sect. 3.3). *Fermi* Science Tools `v10r01p00` and IRFs `P8R2_SOURCE_V6` were used for this analysis[2].

To model the LAT data, we included all sources from the 3FGL within 10° of the radio core position of Fornax A. The Galactic diffuse background model was `template_4years_P8_V2_scaled`, and the isotropic background model was `isotropic_source_4years_P8V3`[3]. Several tests were performed, and we determined that the results presented here with the preliminary diffuse models are compatible with those obtained with the finalized models. We used the same spectral models as in the 3FGL catalog for all

---

[1] `http://www.slac.stanford.edu/exp/glast/groups/canda/lat_Performance.htm`

[2] `http://fermi.gsfc.nasa.gov/ssc/data/analysis/software`

[3] `http://fermi.gsfc.nasa.gov/ssc/data/access/lat/BackgroundModels.html`

background sources, and the normalization and spectral shape parameters of all point sources were left free during optimization. For the diffuse models, only the normalization parameters were left free.

We initially modeled Fornax A as a point source located at the position of the radio core, removing 3FGL J0322.5−3721 from the model since it is offset from the radio core by $0^{\circ}\!.15$. We optimized the localization using the `gtfindsrc` tool provided in the Science Tools in unbinned mode. The best-fit localization is R.A. = $50^{\circ}\!.73$, Decl. = $-37^{\circ}\!.28$ with a 95% confidence error circle radius of $0^{\circ}\!.14$, slightly southeast of the position of the Fornax A core and consistent with the reported 3FGL localization. Figure 4.1 shows the best-fit localization (point B) and the core (point A) as well as the 2FGL and 3FGL error contours plotted on top of the relative residual counts map. Optimizing the model with the single point source at point B, we detect γ-ray emission with TS = 121 (see Sect. B.2.1). The spectrum was modeled as a single power law with a resulting maximum-likelihood photon index $\Gamma = 2.08 \pm 0.08$ and a full-band energy flux of $(5.34 \pm 0.78_{\rm stat}{}^{+0.03}_{-0.05}{}_{\rm sys}) \times 10^{-12}$ erg cm^{-2} s^{-1} (see Table 4.1). Systematic errors are due to the systematic uncertainty in the LAT effective area[4]. These fluxes and indices are consistent with those reported in the catalogs for sources 2FGL J0322.4−3717 and 3FGL J0322.5−3721.

---

[4] `http://fermi.gsfc.nasa.gov/ssc/data/analysis/LAT_caveats.html`

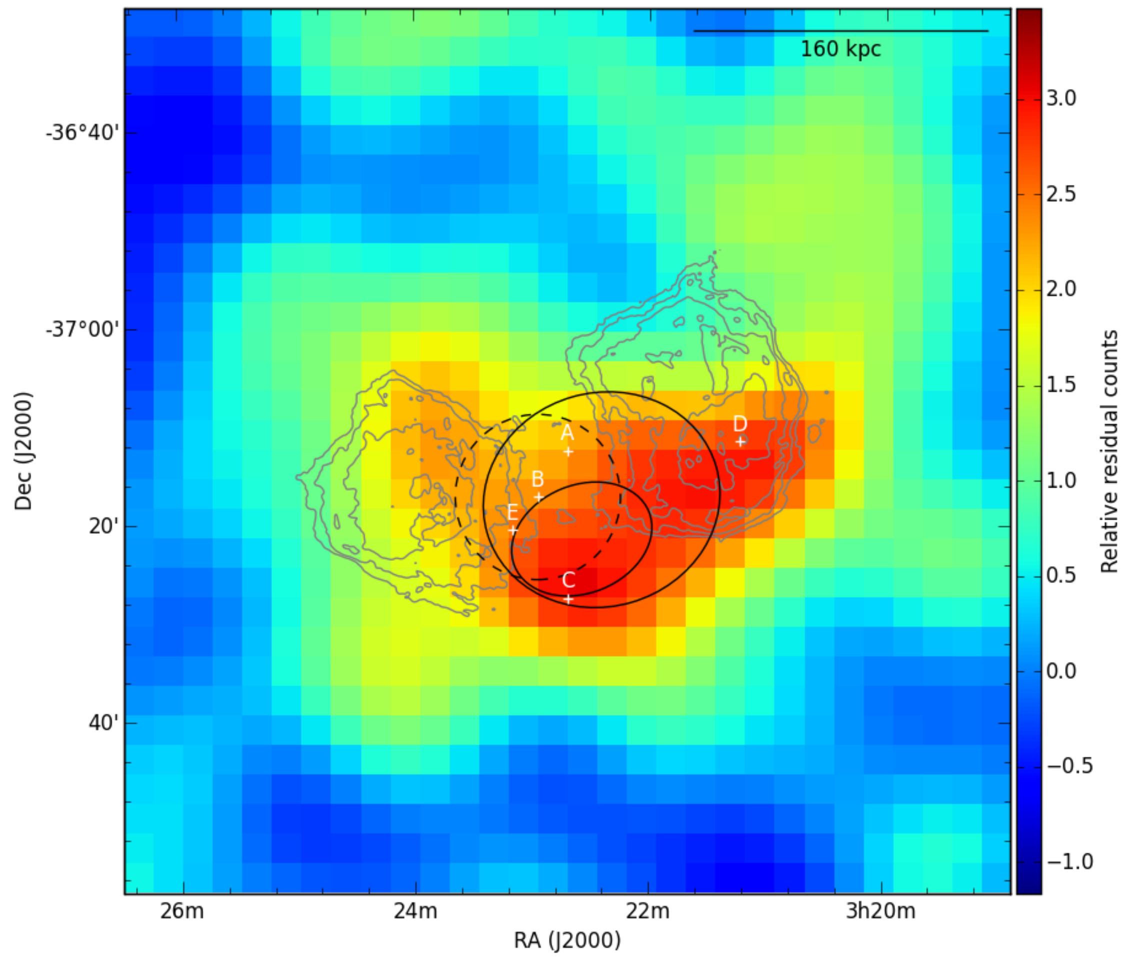

Figure 4.1: Relative smoothed (4.7 px, 0.°24 Gaussian FWHM) residual γ-ray counts ((counts - model)/model) in the 1.°5 square region around the core of Fornax A between 1 and 300 GeV. Overlaid are the radio contours (gray lines) from the VLA observations of [9] with the radio core (position indicated by A) subtracted. The γ-ray residual counts are elongated in a similar way to the radio lobes. Also shown are the 95% confidence error ellipses for 2FGL J0322.4−3717 and 3FGL J0322.5−3721; the 3FGL source has the smaller ellipse. The dashed circle shows the 95% confidence error circle from our maximum-likelihood localization of the region as a single point source centered at position B. The other points (labeled C, D, E) are the locations of various sources and test sources, as detailed in the text and in Table 4.2. This figure is reproduced here from the publication [1].

Table 4.1: Fornax A LAT spectral fit results. Each fit was performed leaving normalization and spectral shape parameters of all sources free, except for the models for the diffuse background γ rays which were fit with only normalization.

Model	TS	Energy flux ($\times 10^{-12}$ erg cm^{-2} s^{-1})	Photon index
Point (best-fit location B)	121	$5.34 \pm 0.78^{+0.03}_{-0.05}$ sys	$2.08 \pm 0.08 \pm 0.03_{\mathrm{sys}}$
Disk (best-fit location B, 0°.33 radius)	158	7 ± 1	1.99 ± 0.07
Radio lobes template	158	$7.57 \pm 1.05^{+0.06}_{-0.08}$ sys	$1.99 \pm 0.07^{+0.03}_{-0.04}$ sys
Two point sources, summed		6.6 ± 0.8	
West (location D)	37	2.9 ± 0.7	2.02 ± 0.13
East (location E)	51	3.7 ± 0.8	2.05 ± 0.11
Radio lobes template and point source (location C), summed		8 ± 1	
Radio lobes template	66	6 ± 1	1.97 ± 0.08
Point source (location C)	14	1.6 ± 0.6	2.01 ± 0.20

4.2.2 Extension and Morphology

In the following, we describe several tests performed to determine the morphology of the observed γ-ray emission from the direction of Fornax A, as summarized in Tables 4.1 & 4.2. All tests on extension and morphology made full use of the additional spatial information brought about by the new Pass 8 PSF event type partitions. The broadband flux and spectrum optimizations in addition to these tests were performed using all PSF types in composite likelihood (see Sect. 3.3.1).

Table 4.2: Fornax A spatial model comparisons. Calculated using the likelihood ratio computation as described in Section 4.2. The third column is the difference in the number of degrees of freedom (DOF) between the two hypotheses. The alternative hypotheses are preferred over the corresponding null hypotheses by the significances σ in the fifth column.

Null hypothesis	Alternative hypothesis	DOF	$\Delta \log \mathcal{L}$	σ	Sect.
Point source (core location A)	Point source (best-fit location B)	2	0.6	0.6	4.2.1
Disk (best-fit location B, $0\overset{\circ}{.}03$ radius)	Disk (best-fit location B, $0\overset{\circ}{.}33$ radius)	1	17.3	5.9	4.2.2.1
Point source (best-fit location B)	Two point sources (locations D and E)	4	16.2	4.8	4.2.2.2
Point source (core location A)	Radio lobes template and point source (core location A)	2	19.8	6.0	4.2.2.3
Radio lobes template	Radio lobes template and point source (core location A)	2	0.7	0.7	4.2.2.3
Radio lobes template, rotated 90° CW	Radio lobes template	1	12.9	5.1	4.2.2.3
Radio lobes template, rotated 90° CCW	Radio lobes template	1	18.9	6.1	4.2.2.3
Radio lobes template	Radio lobes template and point source (location C)	4	7.0	2.7	4.2.2.3

4.2.2.1 Spatial Extension

To determine if the γ-ray emission is extended beyond that of a point source we modeled Fornax A as a flat circular disk of various sizes ($0\overset{\circ}{.}03$ to $0\overset{\circ}{.}75$ in steps of $0\overset{\circ}{.}03$) by producing several disk templates centered at the best-fit location of the LAT source described in Section 4.2.1 (point B in Figure 4.1). The uniform disk is the simplest diffuse spatial model, and the use of a Gaussian profile has typically been shown to produce comparatively little difference in the overall likelihood and best-fit spectral parameters [70]. Using `gtlike` in binned mode (with bin size $0\overset{\circ}{.}05$), we determined the overall likelihood $\mathcal{L}$ as a function of the disk radius r. As shown in Figure 4.2, $\mathcal{L}$ is peaked at $r = 0\overset{\circ}{.}33 \pm 0\overset{\circ}{.}05$, which is roughly compatible with the extent of the lobes as observed in radio (1.5 GHz at $14''$ resolution [9]). By comparing the likelihood of the peak radius with the near-zero radius of $0\overset{\circ}{.}03$ (effectively a point source), we found that the γ-ray emission is spatially extended with 5.9σ confidence ($\Delta \log \mathcal{L} = 17.3$, 1 degree of freedom [71]). See Tables 4.1 and 4.2 for more information, and Appendix B for more on the likelihood formulation.

4.2.2.2 Blind Tests for Morphology

With the aim of making no prior assumptions about the morphology of the γ-ray emission in this region, we used the ROI fit with our position-optimized point source as described in Section 4.2.1 and removed that point source from the model, thereby leaving only the background sources. Using this background model, we created a map of residual counts above 1 GeV in the ROI by subtracting the model's predicted counts from the

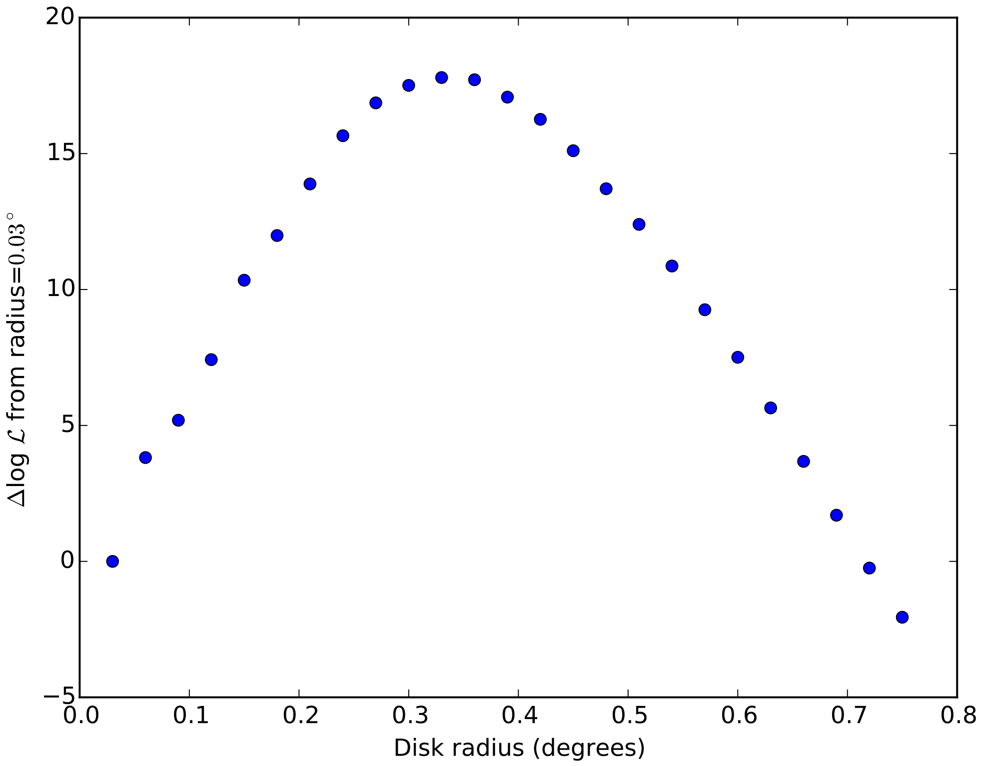

Figure 4.2: $\Delta \log \mathcal{L}$ between a flat disk of radius $0.^\circ03$ (i.e., point-like) and flat disks of various radii. A cubic fit gives a maximum likelihood radius of $0.^\circ33 \pm 0.^\circ05$. The increase in $\mathcal{L}$ from $0.^\circ03$ to the maximum likelihood radius indicates the emission is not point-like. This figure is reproduced here from the publication [1].

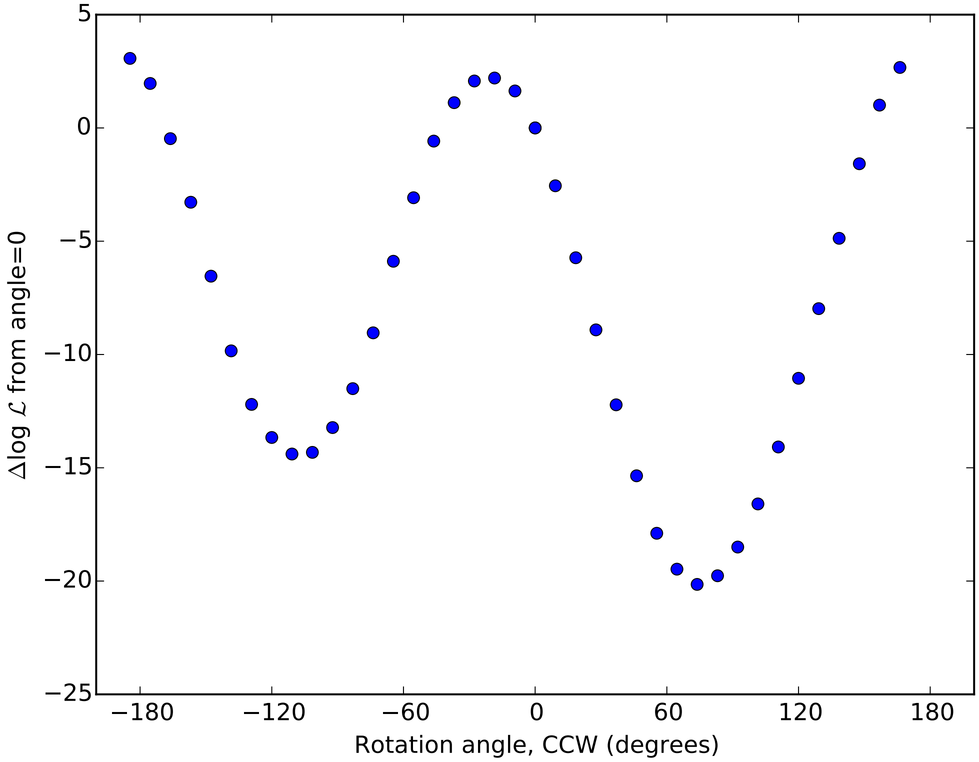

Figure 4.3: $\Delta \log \mathcal{L}$ between the non-rotated radio lobe template and the template rotated around the central core indicating that the unrotated radio morphology is preferred. This figure is reproduced here from the publication [1].

observed counts in each bin. Apart from the emission near Fornax A, the map of residuals is flat in significance and the distribution of significance values for the bins is Gaussian, indicating there are no significant systematic deviations from the ROI model. The map of residual counts shown in Figure 4.1 is cropped to a $1.^{\circ}5 \times 1.^{\circ}5$ region centered around the Fornax A core. The shape of the residuals suggests a non-circular morphology that resembles the known extended radio morphology. The contours of radio emission from a VLA 1.5 GHz image at $14''$ resolution [9], with the radio core subtracted, are overlaid in Figure 4.1.

We also tested a model which included two separate point sources whose initial locations were chosen by eye based upon the residual counts. The locations of these two point sources were then optimized using `gtfindsrc`. The best-fit location of the western point source (labeled D in Figure 4.1) matches well the western lobe's centroid while the eastern point (labeled E in Figure 4.1) is offset from the centroid of the eastern lobe. The double point-source model is preferred over the single point-source model at a confidence level of 4.8σ. Table 4.2 details these results and Table 4.1 lists the fit parameters. Note that the spectral index is statistically compatible with the single point-source model and for both point sources in the double point-source model.

4.2.2.3 Radio-Motivated Tests for Morphology

Assuming that the same electron energy distribution determined from the radio emission scatters optical EBL photons to produce γ rays, then a reasonable guess for the γ-ray morphology should be the observed radio structure. The lobes of Fornax A were found to emit non-thermal IC scattered X-rays, with excellent spatial coincidence to the radio structure produced by synchrotron-emitting relativistic electrons [21]. Diffuse hard X-ray emission associated with the east lobe has been confirmed with *XMM-Newton* [18], implying the magnetic field is reasonably uniform, further supporting the expectation that the γ rays should match the radio morphology. Under these circumstances, as was observed in Centaurus A [25], the relativistic electrons will trace the γ-ray emission [11]. (Whereas this assumption was used at the time of this analysis, we later discovered this is not the case with Cen A in Chapter 6.) However, for the purpose of constraining the EBL with the γ-ray flux, using the radio structure is the best choice for the spatial distribution. Physically, Fornax A images from the Wilkinson Microwave Anisotropy Probe (*WMAP*) might be a better choice of template for the γ-ray emission because the synchrotron radiation within $\sim 23-94\,\mathrm{GHz}$ should be originating from the same band of relativistic electrons that IC scatter into $\sim 0.1-10\,\mathrm{GeV}$ γ rays. We revisit this topic later in the section.

We created a spatial template of the lobe emission using VLA 1.5 GHz radio data [9], which offers a more-than-adequate spatial resolution of $14''$. Both the central core of Fornax A and various radio point sources inside the lobe structure were manually removed from the spatial template, the former by reduction to zero and the latter by interpolation of the adjacent lobe-dominated flux. The central core was reduced to zero because the lobes do not overlap with the central core [15]. This template is shown in Fig. 4.4. Further details on the creation of the template can be found in Appendix A of McConville's Ph.D. thesis [10]. We found this template in addition to a point-source model of the core is preferred over just the point source at the core with a confidence of 6.0σ ($\Delta \log \mathcal{L} = 19.8$,

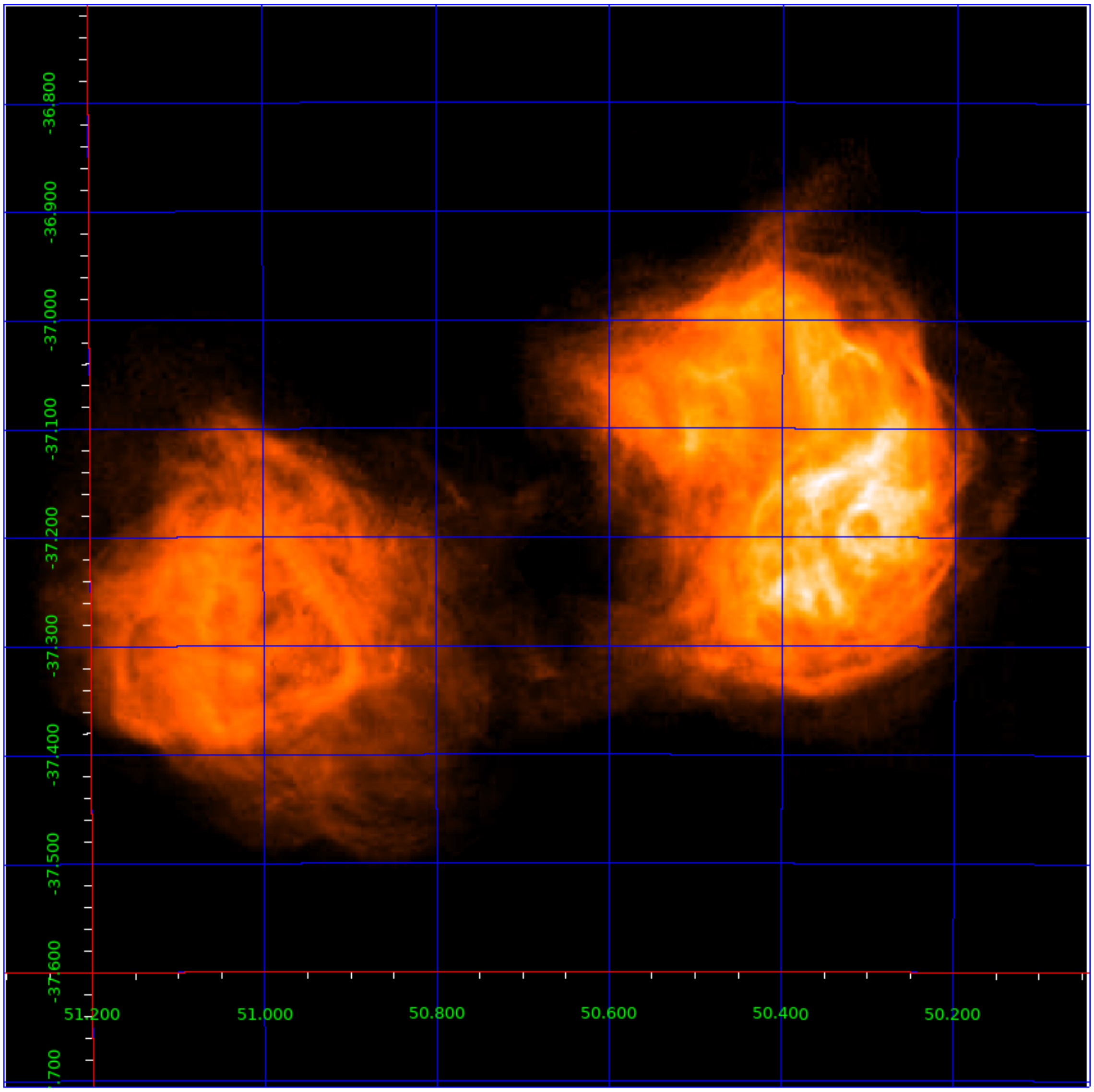

Figure 4.4: Plot of the template for the Fornax A lobes used in this study created from data from VLA at 1.5 GHz. Creation of the template is described in Sect. 4.2.2.3 and with greater detail in Appendix A of McConville's Ph.D. thesis [10].

2 degrees of freedom). However, this combined model is preferred over the lobes template alone by only 0.7σ. Moreover, in the combined point-source-and-lobes template fit only 14% of the energy flux is assigned to the core point source. See Tables 4.1 and 4.2 for more information. We consider this as evidence that the γ-ray emission from the core of Fornax A is insignificant. Minimal γ-ray flux from the central core is expected, as it is assumed to be synchrotron self-Compton, and the radio flux from the core has been reported to be relatively weak compared to the luminous galaxy lobes [54].

In order to test the uniqueness of the radio template morphology and its rotational symmetry, we rotated the template around the central core in increments of $9^{\circ}\!.2$ and computed the likelihood at each one. The results from this test are shown in Figure 4.3 and indicate that the template in its original orientation is preferred. In particular, we see the original orientation is a better model than the one rotated 90° clockwise with 5.1σ confidence ($\Delta\log\mathcal{L}$=12.9, 1 degree of freedom) and 90° counterclockwise with 6.1σ confidence ($\Delta\log\mathcal{L}$=18.9, 1 degree of freedom). The maximum likelihood rotation was $-20^{\circ} \pm 10^{\circ}\!.$ Additionally, our plot of $\log\mathcal{L}$ over template rotation angle shows a sinusoidal profile with a similar peak in likelihood around 180° as around 0°. This degeneracy indicates that the data are not constraining enough to statistically differentiate the lobes. Modeling the lobes as separate point sources (see Section 4.2.2.2) results in the measurement of similar fluxes and spectral shapes for the two regions, but this is at odds with radio observations of the lobes. According to the 1.5 GHz VLA observation [9], the west lobe has about twice the total flux than the east. In fact, the two point-source γ-ray analysis indicated the east lobe may be slightly brighter (but is within the statistical errors). This disagreement may be a symptom of our use of 1.5 GHz VLA data instead of the very similar but more physically motivated $\sim$ 23 – 94 GHz *WMAP* data as a spatial template for the γ-rays. Indeed, the flux ratio of west to east is $\sim$ 1.3 in the *WMAP* 41 and 61 GHz maps [11], closer to the γ-ray result. However, Fornax A is at the resolving power of the LAT in this analysis and the PSF is broad enough ($\sim$ $0^\circ\!.8$ radius at 1 GeV) that fine scale changes would be smoothed out and indistinguishable from the original, and small changes in the flux ratio between the lobes should leave the average flux nearly the same. This is highlighted by the similarity in overall likelihood we observe between 0° and 180° rotations of the 1.5 GHz VLA template, where the rotation of 180° is identical to a flux ratio of $\sim$ 0.5. In addition, even when using the spatial morphology of a single point source, the flux is nearly consistent with the radio template flux (see Section 4.2.1).

With the aim of testing the region for the possibility of a contaminating background γ-ray source, we added a point source to the lobes template model and optimized its position using `gtfindsrc`. The optimized position of this point source (labeled C in Figure 4.1) was R.A. = $50^\circ\!.67$, Decl. = $-37^\circ\!.46$ with a 95% confidence error circle radius of $0^\circ\!.42$ (large enough to encompass the whole Fornax A emission region). The resulting fit was marginally preferred over the lobes template alone with 2.7σ significance. Therefore, we do not consider any contribution from a background point source to be significant.

4.2.3 Spectral and Temporal Analysis

In the following we assume the radio morphology template (without any core contribution) is the best description of the Fornax A γ-ray emission. The likelihood ratio technique cannot quantify whether the radio template is statistically preferred with respect to the best-fit disk model because these models are not nested (see Sect. B.2.1). However, the radio template is the physically motivated model based on the leptonic scenario of γ-ray production. Further, the rotation study presented above indicates a preferred axis of the γ-ray emission which mimics the elongated emission observed at radio frequencies, in turn supporting the similarity between the γ-ray and radio emission morphology.

We tested several broadband spectral models (log-parabola, broken power law, and broken power law with an exponential cutoff), and found none were significantly preferred over the single power law. Then, we measured spectral points by fitting each of 6 equal logarithmically spaced energy bins from 0.1 to 300 GeV to a power law and optimized the flux normalizations by maximizing the likelihood function. In each bin, the normalization parameters for all sources were free, and all other parameters were fixed to the values obtained from the broadband fit. These spectral data points are shown in Figure 4.5 and Table 4.3. The source is detected in 4 of the 6 spectral bins with $\mathrm{TS} > 5$, and 95% confidence upper limits were calculated for the two lower-significance bins (at the highest energies).

To test the γ-ray variability over the 6.1 year period, we made a 0.1–300 GeV light curve in time bins of 185 days, which was found to be the smallest possible time scale while maintaining a reasonable significance of detection in the majority of bins. For each time interval, the emission associated with Fornax A was fit to a single point source (positioned at the best-fit location B in Figure 4.1), as we expected any potential variable emission to be associated with a point source at the core and not the lobes. All sources included in the 6.1 year analysis were fit with all spectral shape parameters fixed to their optimized values from the full fit, while all normalizations were left free. Upper limits

Table 4.3: Fornax A total lobe LAT spectral flux assuming radio lobes template spatial model. For bins with a * added, energy fluxes given are 95% confidence upper limits.

Bin energy range (GeV)	Energy flux ($\times 10^{-12}$ erg cm^{-2} s^{-1})	TS
0.10 – 0.38	0.7 ± 0.4	6.1
0.38 – 1.4	1.0 ± 0.2	49
1.4 – 5.5	1.1 ± 0.2	87
5.5 – 21	0.8 ± 0.2	22
21 – 79*	< 1.7	3.5
79 – 300*	< 2.6	4.3

were calculated for time bins within which the TS fell below 4 ($< 2\sigma$). The significance of variability was determined following the method described in [65]. Our analysis yielded a 1.3σ confidence that the emission is variable, and so we conclude that we do not observe significant variability. This result is consistent with previous work on Fornax A variability using Pass 7 LAT data [10].

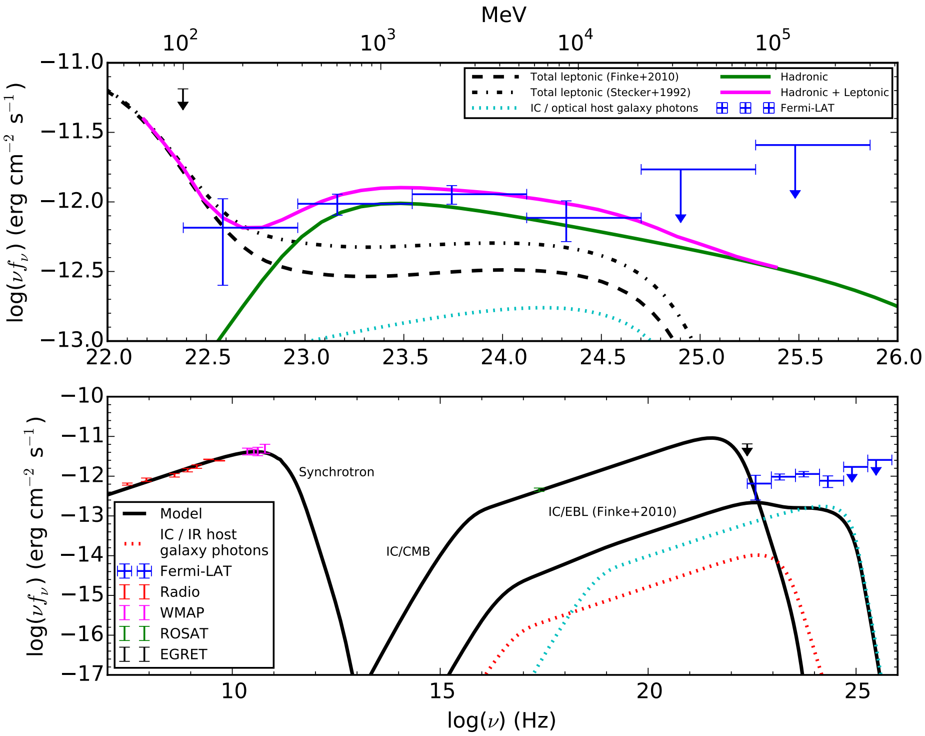

Figure 4.5: Broadband SED of the lobes of Fornax A (bottom panel) and detailed view of the high-energy part of the SED (top panel). As in [11], we used archival measurements of the total lobe radio flux densities (shown in red) from [12–17], as collected by [18], replacing an extrapolated 100 MHz data point from [12] with an 86 MHz measurement [19]. The 3-year integrated *WMAP* data are shown in magenta [20], and X-ray data from ROSAT [21] are shown in green. The LAT data points from this study are shown in blue. The black upper limit point is from EGRET [22]. The black solid lines from left to right show the synchrotron ($< 10^{13}$ Hz), IC/CMB ($> 10^{13}$ Hz), and IC/EBL (on the assumption of the model of [23]) flux models ($> 10^{15}$ Hz). The dashed black line shows the IC/EBL flux models assuming the fast evolution model of [24]. The dotted red and cyan lines show the IC upscattered host galaxy photon flux from infrared and optical, respectively. The solid green line shows the hadronic model flux, while the solid magenta line shows the combined hadronic and leptonic model flux. This figure is reproduced here from the publication [1].

Chapter 5: Centaurus A Core

As of the time of this writing, an article on the work described in this chapter has been accepted for publication into the journal Astronomy & Astrophysics. The preprint version is available online [2]. It has been included it here, edited for clarity for its inclusion into the thesis.

5.1 Introduction

Active galaxies host a small, bright core of non-thermal emission. At a distance of $d \simeq 3.8$ Mpc, Cen A is the nearest active galaxy [72, 73]. Its proximity has allowed for a detailed morphological analysis over angular scales ranging from milli-arcseconds to several degrees ($1^\circ \simeq 65$ kpc). A variety of structures powered by its AGN have been discovered using observations in radio [74–76], infrared [77–79], X-ray [74, 80], and γ-ray [25,81,82] bands. These structures include a radio emitting core with a size of $\leq 10^{-2}$ pc, a parsec-scale jet and counter-jet system, a kiloparsec-scale jet and inner lobes, up to giant outer lobes with a length of hundreds of kiloparsecs.

Based on its radio properties, Cen A has been classified as a radio galaxy of Fanaroff-Riley type I [37]. According to AGN unification schemes, radio galaxies of this type are thought to correspond to BL Lac objects viewed from the side, the latter showing jets aligned along the line of sight and corresponding to a subclass of blazars [33]. BL Lac objects are the most abundant class of known extragalactic VHE emitters[1], and exhibit double-peaked SEDs. It is commonly thought that their low-frequency emission in the radio to ultraviolet (and X-ray, for high-peaked BL Lacs) band is synchrotron emission from relativistic electrons within a blob (zone) moving at relativistic speeds in the jet. Synchrotron self-absorption implies that the lower-frequency observed radio emission cannot be produced by a compact blob and is likely produced by synchrotron from a larger jet component. The high-energy emission (hard X-ray to VHE γ-ray) from high-peaked BL Lac type objects has been satisfactorily modeled as SSC radiation resulting from the inverse Compton upscattering of synchrotron photons by the same relativistic electrons that produced the synchrotron radiation [83, 84], although other more complex models (involving e.g. external inverse Compton emission, hadronic interactions, or multiple zones) are conceivable [85].

At a few tens of keV to GeV photon energies, Cen A was detected by all instruments on board the *Compton* Gamma-Ray Observatory in the period 1991-1995 revealing a high-energy peak in the SED at an energy of ~ 0.1 MeV [86–88]. An earlier investigation found that it is possible to fit the data ranging from the radio band to the γ-ray band using a single-zone SSC model [89], but this implies a low flux at VHE. High-energy and VHE γ-ray observations are thus important to test the validity of the SSC scenario for modeling of the SED of radio galaxies.

The discovery of Cen A as an emitter of VHE γ rays was reported on the basis of 115 hr of observation (labeled data set A in this study) with H.E.S.S. performed from

---

[1] `http://tevcat.uchicago.edu/`.

April 2004 to July 2008 [90]. The signal from the region containing the radio core, the parsec-scale jet, and the kiloparsec-scale jet was detected with a statistical significance of 5.0σ. In this work, we refer to this region as the Cen A γ-ray core. Subsequent survey observations at high energies were performed by the LAT on board the *Fermi Gamma Ray Space Telescope* (FGST) launched in June 2008 [5]. During the first three months of science operation, started on August 4, 2008, *Fermi*-LAT confirmed the EGRET detection of the Cen A γ-ray core [91]. Spectral analysis and modeling based on ten months of *Fermi*-LAT observations [81] suggested the high-energy γ-ray emission up to $\sim$ 10 GeV to be compatible with a single power law, yet indicated that a single-zone SSC model would be unable to account for the (non-contemporaneous) higher energy TeV emission observed by H.E.S.S. in 2004-2008. The analysis of extended *Fermi*-LAT data sets has in the meantime provided increasing evidence for a substantial spectral break above a few GeV [92, 93]. This supports the conclusion that the TeV emission observed in 2004-2008 with H.E.S.S. belongs to a distinct, separate spectral component.

In this chapter, we present the results of long-term observations of the Cen A γ-ray core performed both with H.E.S.S. and with *Fermi*-LAT. These include new (more than 100 hr) VHE observations of the Cen A γ-ray core with H.E.S.S. performed when the FGST was already in orbit. We report results of the spectral analysis of the complete H.E.S.S. data set with an exposure time that is twice that used in the previously published data, as well as an update of the spectrum of the Cen A γ-ray core obtained with *Fermi*-LAT at GeV energies. The results are discussed and put into wider context in Section 7.2.

5.2 H.E.S.S. observations and results

Cen A is a weak VHE source with a measured integral flux above 250 GeV of about 0.8% of the flux of the Crab Nebula.[2] The discovery of faint VHE γ-ray emission from Cen A motivated further observations with H.E.S.S., which were performed in 2009-2010. In this section, we report the results of the Cen A observations with H.E.S.S. taken between 2004 and 2010.

5.2.1 Observations

The H.E.S.S. experiment is an array of five imaging atmospheric Cherenkov telescopes located in the southern hemisphere in Namibia (23°16′18″ S, 16°30′00″ E) at an altitude of 1800 m above sea level [94]. At the time of the observations used in this study, the H.E.S.S. array consisted of four 12-meter telescopes. The telescopes, arranged in a square with 120-m sides, have been in operation since 2004 [95]. Each of these telescopes covers a field of view of 5° diameter. H.E.S.S. employs the stereoscopic imaging atmospheric Cherenkov technique [96] and is sensitive with these telescopes to γ rays above an energy threshold of ~ 0.1 TeV for observations at zenith, up to energies of tens of TeV. For details about the H.E.S.S. analysis, please refer to the publication of this work [2].

---

[2] The observed integral flux of the Crab Nebula above 1 TeV is $(2.26 \pm 0.08_{\text{stat}} \pm 0.45_{\text{sys}}) \times 10^{-11}$ cm^{-2}s^{-1} [94].

5.2.2 Results of the observations of Cen A with H.E.S.S.

The γ-ray core of Cen A was firmly detected by H.E.S.S. at a statistical significance of 12σ. Spectral analysis yields a photon index of $\Gamma = 2.52 \pm 0.13_{\rm stat} \pm 0.20_{\rm sys}$ and a normalization constant of $N_0 = (1.49 \pm 0.16_{\rm stat}{}^{+0.45}_{-0.30}{}_{\rm sys}) \times 10^{-13}$ cm^{-2} s^{-1} TeV^{-1} at E_0=1 TeV. The reconstructed spectrum of the Cen A γ-ray core is shown in Fig. 5.1. All of the eight SED data points in the VHE range are above a 2.5σ significance level, while only one SED data point exceeds a 2σ significance level in the 2009 study [90]. The derived data points for each energy band in the VHE range, shown in Fig. 5.1, agree within error bars with those for the first and second data sets. The VHE spectrum of the Cen A core is compatible with a power-law function ($\chi^2 = 3.9$ with 6 DOF).

If one takes the values of the spectral parameters from the 3FGL [34] obtained from the *Fermi*-LAT observations of Cen A between 100 MeV and 100 GeV assuming a single power-law spectrum, then one finds that $N_0 = (0.45 \pm 0.07) \times 10^{-13}$ ph cm^{-2}s^{-1}TeV^{-1} at 1 TeV and $\Gamma = 2.70 \pm 0.03$. Therefore, the differential flux at 1 TeV derived from the H.E.S.S. observations in 2004-2010 is about 3.5 times larger than that inferred from a power-law extrapolation of the 3FGL catalog spectrum. This indicates that a deviation of the spectrum from a single power law ("hardening") should occur at GeV energies to match the TeV data.

We searched the combined data set for evidence of time variability at the position of the Cen A core. No significant variability was found on timescales of 28 minutes (individual runs), months, or years. The lack of apparent flux variability along with no change in spectral parameters between the two data sets justifies combining all available data when

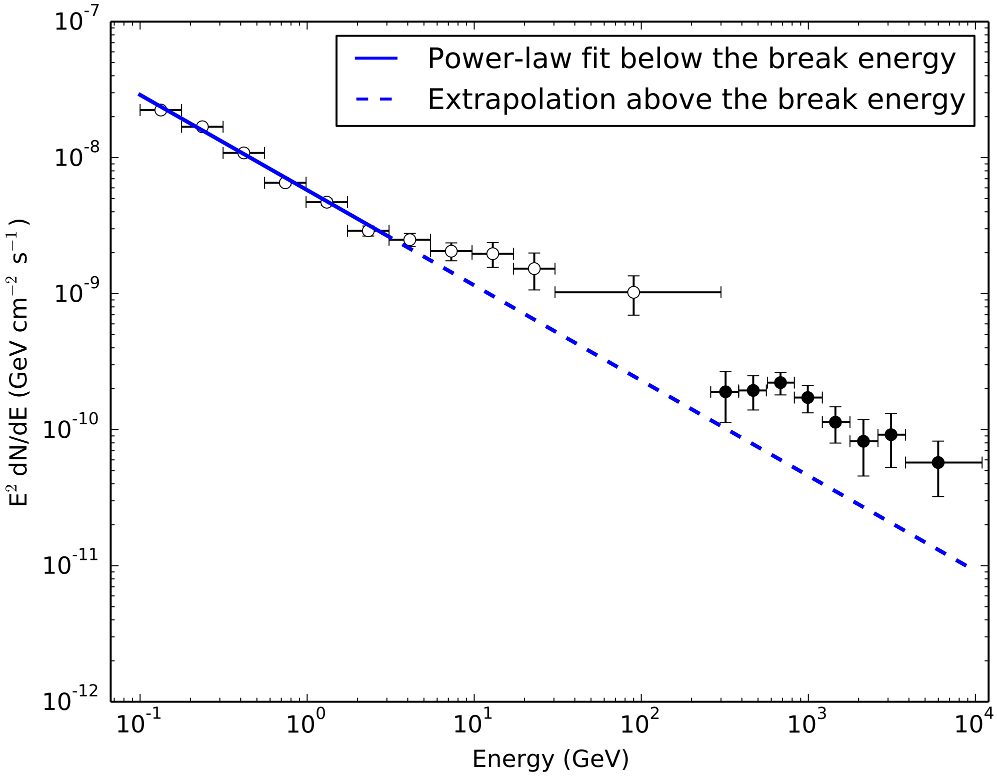

Figure 5.1: SED of Cen A γ-ray core. *Fermi*-LAT and H.E.S.S. data points along with a high-energy power-law extrapolation of the γ-ray spectrum measured below the break energy. Eight years of *Fermi*-LAT data and 213 hours of H.E.S.S. data were used. Statistical error bars are shown. This figure is reproduced here from the publication [2].

comparing the spectrum to that of *Fermi*-LAT. We note that given the low flux level of the Cen A γ-ray core, a flux increase by a factor of approximately ten would be needed to allow a significant detection of variability on timescales of 28 minutes (corresponding to a 5σ detection in individual runs).

5.3 *Fermi*-LAT observations and results

In HE γ rays, the core of Cen A is firmly detected with the *Fermi*-LAT using eight years of Pass 8 data spanning over three orders of magnitude in energy. LAT analysis of Cen A involves unique challenges not present in other individual extragalactic source analyses, largely due to the massive angular extent of the Cen A non-thermal outer lobes of $\sim 9^\circ$ and the proximity to the Galactic plane (Galactic latitude $\approx 19.4^\circ$), which is a bright source of diffuse γ-ray emission. In the following, we report corroborating evidence for the presence of an additional spectral component at γ-ray energies above a break of $\simeq 2.8$ GeV. No significant variability either above or below this break has been detected.

5.3.1 Observations and analysis

As described in Chapter 3, the LAT is a pair-conversion telescope on the FGST [5] with a large field of view (~2.4 sr) which has been scanning the entire sky continuously since August 2008. Thus, the LAT can provide HE data simultaneous with H.E.S.S. to give a clear spectral picture across a much wider band of energies.

We selected Pass 8 `SOURCE` class *Fermi*-LAT photon data spanning eight years between August 4, 2008 and July 6, 2016 (MET 239557417 to 489507985) with energies between 100 MeV and 300 GeV. Higher energies than 300 GeV yielded no detection. We performed a binned analysis by choosing a $10^\circ \times 10^\circ$ square ROI centered at the position of the Cen A core (3FGL J1325.4-4301) as reported in the 3FGL catalog, R.A. = $201\overset{\circ}{.}367$, Decl. = $-43\overset{\circ}{.}030$ [34], with spatial bins $0\overset{\circ}{.}1$ in size and initially eight energy bins per decade. We applied standard quality cuts `(DATA_QUAL==1 && LAT_CONFIG==1)` and removed all events with zenith angle $> 90^\circ$ to avoid contamination from the Earth's limb (see Sect. 3.3). In the following, models are compared based on the maximum value of the logarithm of the likelihood function, $\log\mathcal{L}$. The significance of model components or additional parameters is evaluated using the test statistic, whose expression is $\mathrm{TS} = 2(\log\mathcal{L} - \log\mathcal{L}_0)$, where $\mathcal{L}_0$ is the likelihood of the reference model without the additional parameter or component (see Sect. B.2.1) [97].

To model the sources within the ROI, we began with sources from the 3FGL within the $15^\circ \times 15^\circ$ region enclosing the ROI (the 3FGL models the Cen A lobes with a template created from 22 GHz *WMAP* data [98] as shown in Fig. 5.2). We included the isotropic and Galactic diffuse backgrounds, `iso_P8R2_SOURCE_V6_v06` and `gll_iem_v06` [99], respectively. We fixed the normalizations of both the isotropic and Galactic diffuse source models to one to avoid leakage of photons from the Cen A lobes into these templates; when free, they converged to unrealistic values. The convergence to unrealistic values is due to unmodeled emission from the Cen A lobes. We introduced additional background sources in order to account for excess lobe emission. After creation of the fully developed model, freeing both these diffuse sources has a negligible effect on the results. We optimized each source in the model individually using `optimize` within `fermipy` (see

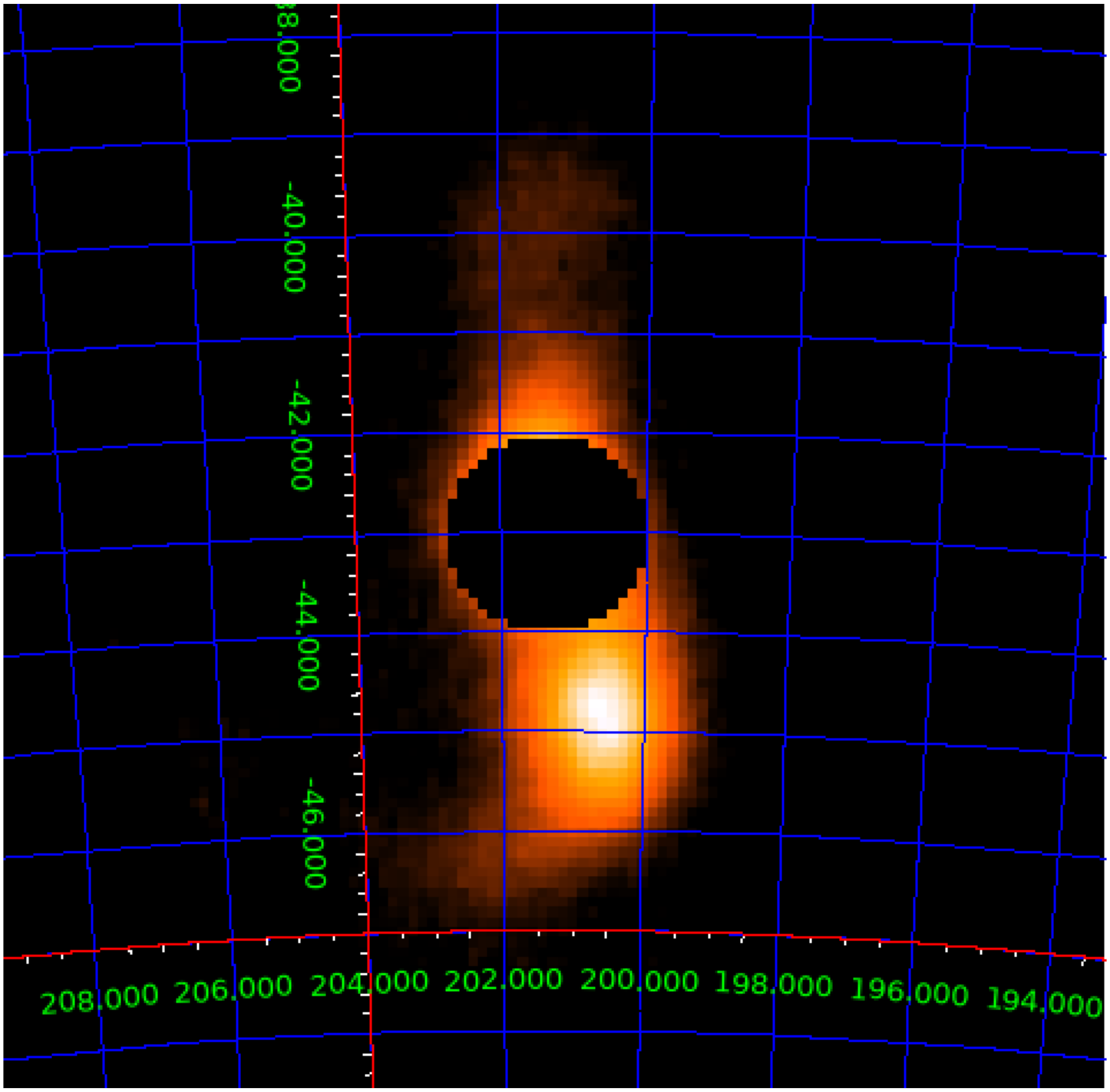

Figure 5.2: Template of Cen A lobes created from *WMAP* at 22 GHz [25].

Sect. 3.4.2), and then left the normalization parameters of sources within 3° and the spectral shapes of only the core and lobes free during the final likelihood maximization. We generated a residual TS map and residual significance map for the ROI and found several regions with data counts in excess of the model (see Sec. 3.4.2). New, fainter sources may then be identified at local maxima of the TS map. Using the residual TS map as a guide for missing emission, we added ten additional background sources to the ROI model. These ten sources are most likely a surrogate for excess lobe emission and should not be considered new individual point sources. After re-optimization and creation of a residual TS map, we observe no significant ($> 5\sigma$) regions of excess counts, and a histogram of the residuals is well fit as a Gaussian distribution centered around zero.

The precise γ-ray morphology of the Cen A lobes is beyond the scope of the work in this chapter and is not needed to accurately determine the SED of the core. This work on the Cen A core does not require a high-precision model for the lobes, as the angular size of the Cen A lobes is sufficiently larger than the PSF of the LAT, especially at higher energies where this study is focused ($< 1°$ 95% containment angle above 5 GeV)[3]. However, to verify this, we tested the modeling procedure above using two alternative γ-ray templates of the Cen A lobes. The first of these was a modification to the public *WMAP* template involving "filling in" the 2° diameter hole surrounding the core. This was accomplished by patching this area with nearby matching intensities. This template is shown in Fig. 5.3. The second alternate lobe template tested was one made from radio data from the Parkes telescope at 6.3 cm wavelength as shown in Fig. 5.4 [26]. Use of these alternate lobe templates had no significant effect on the resulting best-fit core break

---

[3] `https://www.slac.stanford.edu/exp/glast/groups/canda/lat_Performance.htm`.

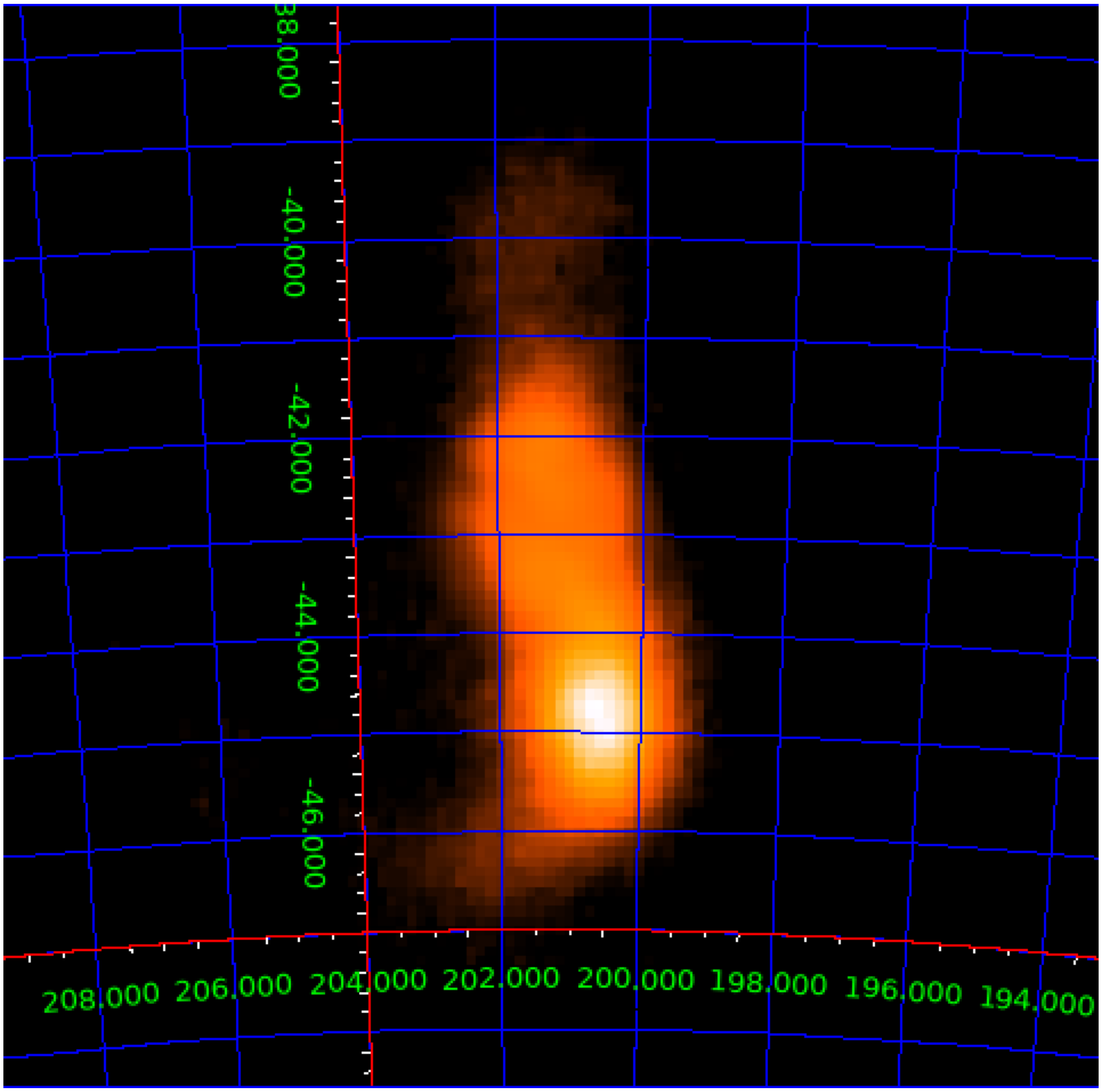

Figure 5.3: “Filled in” modified version of the 22 GHz *WMAP* Cen A lobes template as described in Sect. 5.3.1

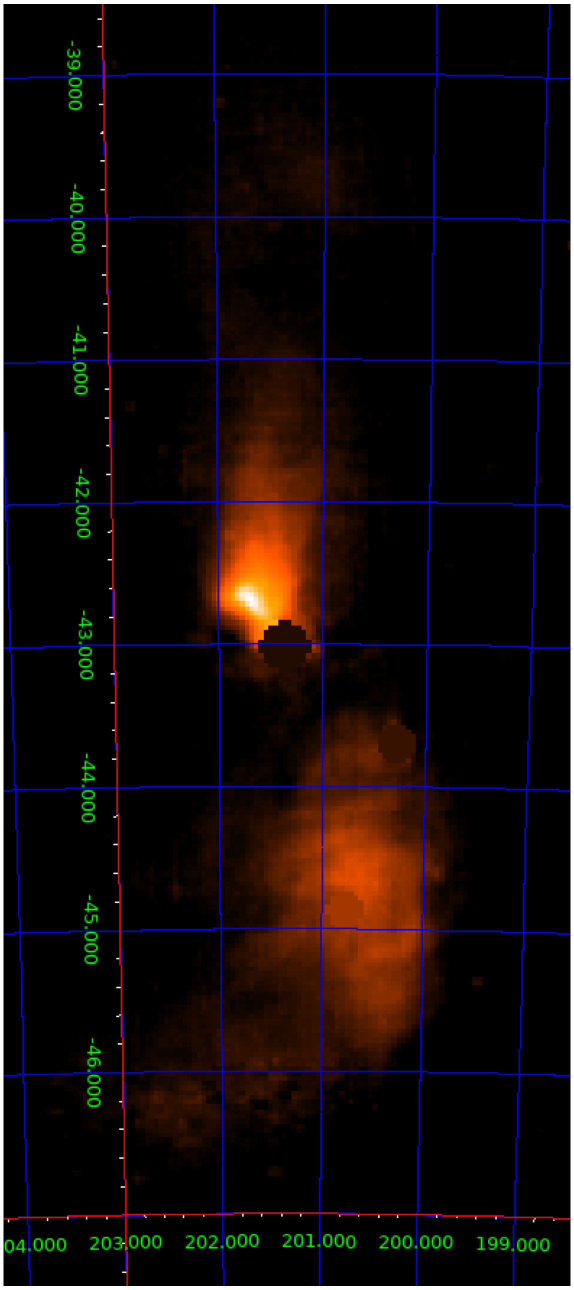

Figure 5.4: Template of the Cen A lobes created from Parkes radio data at 6.3 cm wavelength [26].

energy or the flux above the break energy. However, we did observe a flux deviation below the break energy, resulting in a drop in the full band energy flux of the core by up to 17% depending on which lobe template was being used. We believe this drop results from the lack of a hole (circle containing values of 0) around the core of the lobe template with the modified *WMAP* and the Parkes templates. We also introduced a version of the Parkes template with a hole matching the one in the *WMAP* and observed a flux increase of 2% instead of a drop, lending credence to our belief that the existence of the hole is the most important factor for this analysis.

5.3.2 Results of the observations of Cen A with *Fermi*-LAT

We calculated an SED over the full range by dividing the data into 14 equally spaced logarithmic energy bins and then merging the four highest energy bins into one for sufficient statistics. In each bin, the Cen A lobe and core spectral parameters were left free to optimize and within each bin these spectra were fit using a single power law. The resulting SED is plotted in Figs. 5.1 and 7.1. To plot the data point within the wide merged energy bin, we used the prescription from Lafferty & Wyatt 1995 [100]. The spectral hardening in the HE γ-ray emission from the core of Cen A above an energy break of 2.8 GeV is illustrated in Fig. 5.1. A broken power-law model describes well the shape of the *Fermi*-LAT γ-ray spectrum with a break energy of 2.8 GeV.

We optimized the break energy via a likelihood profile method. For this purpose, we fixed all parameters in the ROI model except the normalizations of sources within a 3° radius of the core to their best-fit values from the full optimization. The $\log\mathcal{L}$ profiles for the broken power-law spectral model were computed using the *WMAP*, modified *WMAP*, and Parkes templates as plotted in Fig. 5.5. From the position of the peak in the profile corresponding to the *WMAP* template, we find a best-fit break energy of $2.8^{+1.0}_{-0.6}$ GeV. To determine the statistical preference of the broken power-law model over the single power law, we subtract the overall $\log\mathcal{L}$ from the same ROI model with a single power law from the $\log\mathcal{L}$ from the break energy profile at 2.8 GeV. Because these models are nested, Wilks' theorem yields a preference of the broken power law with 4.0σ confidence ($\chi^2 = 19.0$ with 2 DOF).

From this fully optimized γ-ray model of the Cen A core, we obtain a strong detection at the 73σ statistical level and calculate a full-band energy flux of $(4.59 \pm 0.14_{\rm stat}{}^{+0.17}_{-0.13\,{\rm sys},A_{\rm eff}})\times 10^{-5}$ MeV cm^{-2} s^{-1}. The best-fit broken power-law prefactor[4] is $(3.64 \pm 0.15) \times 10^{-13}$ cm^{-2} s^{-1} MeV^{-1}. In the lower-energy band, we find a photon index of $2.70 \pm 0.02_{\rm stat}{}^{+0.05}_{-0.03\,{\rm sys},A_{\rm eff}}$, and in the higher band, $2.31 \pm 0.07_{\rm stat}{}^{+0.01}_{-0.04\,{\rm sys},A_{\rm eff}}$. This provides corroborating evidence for a spectral hardening by $\Delta\Gamma \sim 0.4$ above the break energy. Comparisons of these results to the Cen A core spectrum from the 3FGL catalog [34] are not meaningful, since their analysis did not include modeling of the Cen A core spectrum as a broken power law. Using the modified *WMAP* template we observe a consistent photon index in the lower and upper bands, respectively, of 2.68 ± 0.03 and 2.26 ± 0.07, and using the Parkes template, 2.67 ± 0.03 and 2.29 ± 0.07. We also tested for a log-parabola spectral shape using a likelihood ratio test, analogous to `Signif_Curve` in the 3FGL catalog, which was calculated as $2.3\,\sigma$, with a $\mathrm{TS}_{\rm curve} = 4.5$, or $\sim 2.1\,\sigma$. The power-law

---

[4] `https://fermi.gsfc.nasa.gov/ssc/data/analysis/scitools/source_models.html#BrokenPowerLaw`

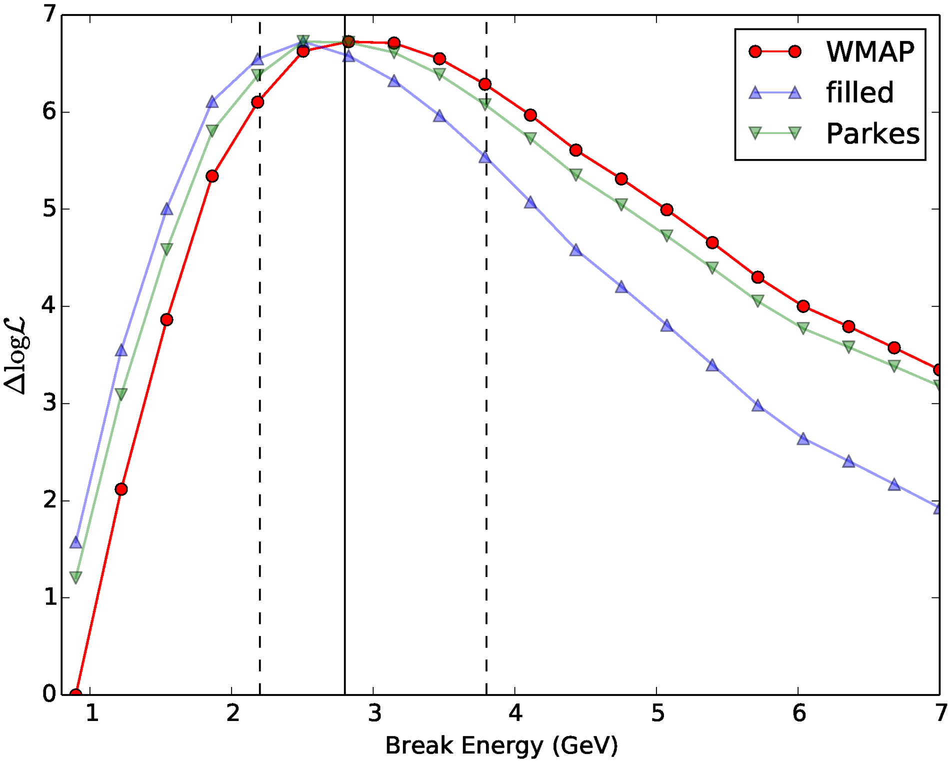

Figure 5.5: Change in overall logℒ while fixing Cen A core break energy to values within the range 0.9 – 7.0 GeV as derived from *Fermi*-LAT data using the *WMAP*, modified *WMAP*, and Parkes templates and compared to the logℒ value at 0.9 GeV for the *WMAP* template. The solid vertical line shows the best-fit value of the break energy parameter, while the dashed vertical lines show 1σ interval for the parameter. This figure is reproduced here from the publication [2].

index that we observe above the spectral break is consistent with the index above 10 GeV found in the 3FHL catalog [101].

Finally, we tested for variability of the Cen A core both above and below the break energy (2.8 GeV) by calculating light curves using a single power-law spectral model for each with the `lightcurve` tool within `fermipy` (see Sect. 3.4.2). Below the break, we divided the data into 64 45-day bins and calculated flux variability using the method described in the 2FGL [65] and Appendix C, with systematic correction factor $f = 0.02$. Keeping the power-law index fixed to 2.70, we calculate 0.09σ ($\chi^2 = 47.3$ with 63 DOF) significance for flux variability. Above the break, we divided the data into nine-month bins. Keeping the power-law index fixed to 2.31, we do not see evidence for flux variability (1.9σ, $\chi^2 = 16.6$ with 9 DOF).

Chapter 6: Centaurus A Lobes

6.1 Introduction

As mentioned in Sect. 5.1, the radio galaxy Cen A is the closest active galaxy at a distance of $d \simeq 3.8\,\mathrm{Mpc}$ [73]. Cen A features a clear double-lobed structure with outer lobes appearing hundreds of kpc away from the core in the same directions as the relativistic jets. From the radio morphology of the lobes, Cen A is classified as Fanaroff-Riley type I [37]. The outer lobes have been studied extensively in the radio and microwave bands. While the core of Cen A was firmly detected in γ rays by EGRET, there was insufficient sensitivity and angular resolution to observe the less intense diffuse outer lobes. In 2010, using $\sim$ 10 months of γ-ray data from the newly launched *Fermi*-LAT, the first γ-ray image of the outer lobes was created [25]. It was found to match well with the microwave morphology as observed by *WMAP* at 22 GHz [98].

In subsequent years, a template for the γ-ray emission made from this 22 GHz *WMAP* image (shown in Fig. 5.2) was used when modeling the Cen A outer lobes, including in all catalogs published by the *Fermi*-LAT Collaboration. With increased statistics from longer exposure time and with improvements made possible by the introduction of Pass 8 (see Sect. 3.3.1), it eventually became clear that the *WMAP* template was no longer sufficient at modeling the γ rays from these lobes. In fact, a clear outline of excess γ-ray emission became visible after accounting for lobe emission from the *WMAP* template beyond the known spatial extent of the lobes [45]. An example of this excess in shown in Fig. 6.1. This unexpected emission raises many questions, as the lobe emission has thus far been attributed to a simple leptonic model in which the same population of electrons produce synchrotron emission in the radio band and external Compton emission in γ rays via scattering off of the CMB photon field [25]. See Fig. 6.2 for the broadband SED. In the SED showing detail in the LAT range in Fig. 6.3, we can see that the IC from the CMB dominates. Therefore, we would expect good spatial coincidence between the radio and γ radiation.

In this chapter, we describe our study of the γ-ray morphology of the outer lobes of Cen A with the hope of better understanding this excess γ-ray emission phenomenon. We describe how we extracted a γ-ray morphology of the outer lobes of Cen A from data taken by *Fermi*-LAT using an iterative process concurrent with extraction of a background model. We explain how we performed checks on the extracted morphology to determine its uniqueness and specificity.

6.2 Observations & Analysis

6.2.1 *Fermi*-LAT Observations

We selected a $15^\circ \times 15^\circ$ region of interest (ROI) around the location of the Cen A core (RA= 201, DEC= -43.5) from the P8R2 source class (`evclass` 128) LAT dataset between August 4, 2008 (MET 239557417) and April 3, 2018 (MET 544459317), about 9.7 years, in the energy range from 100 MeV to 300 GeV. Using the software pack-

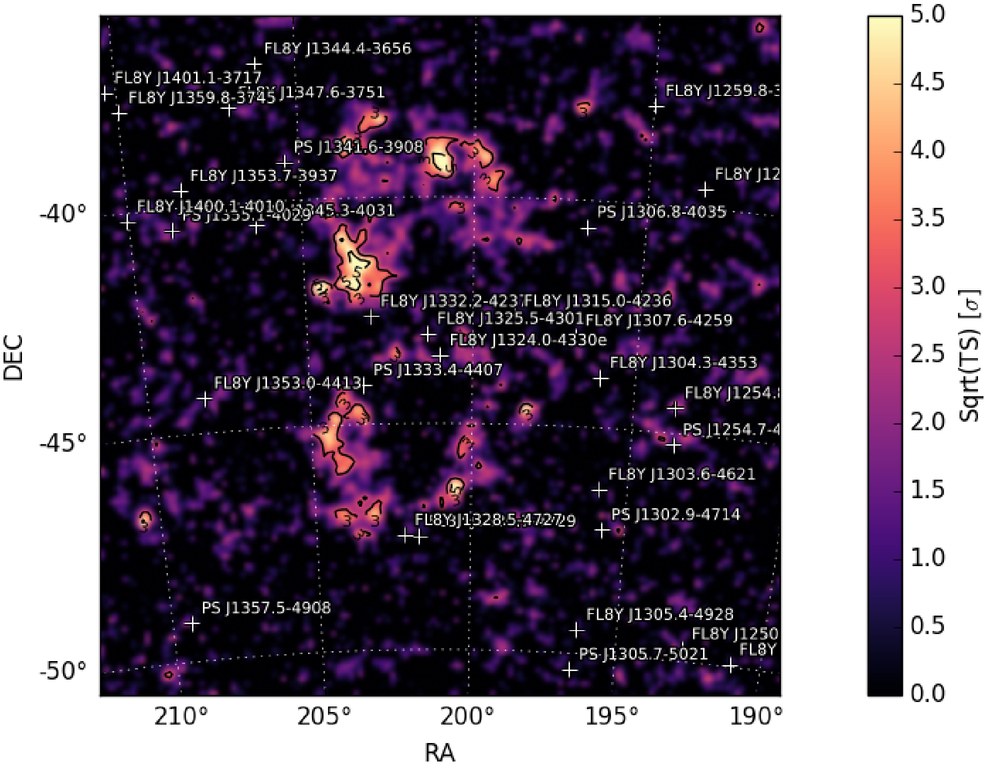

Figure 6.1: TS map of 9.7 years of Pass 8 LAT data cut above 1 GeV in the 15° × 15° ROI surrounding Cen A. This plot highlights the significant excess γ-ray emission present after modeling all visible point sources and the *WMAP* template (see Fig. 5.2) for the Cen A lobes. White text labels indicate sources being modeled. Those starting with "PS" were added during the analysis.

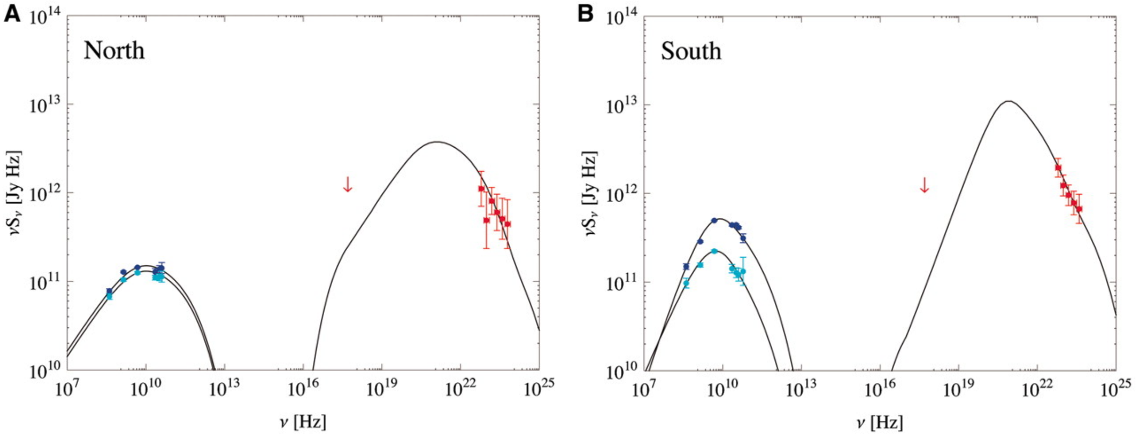

Figure 6.2: Broadband SED of emission from each lobe of Cen A. See the article for details [25].

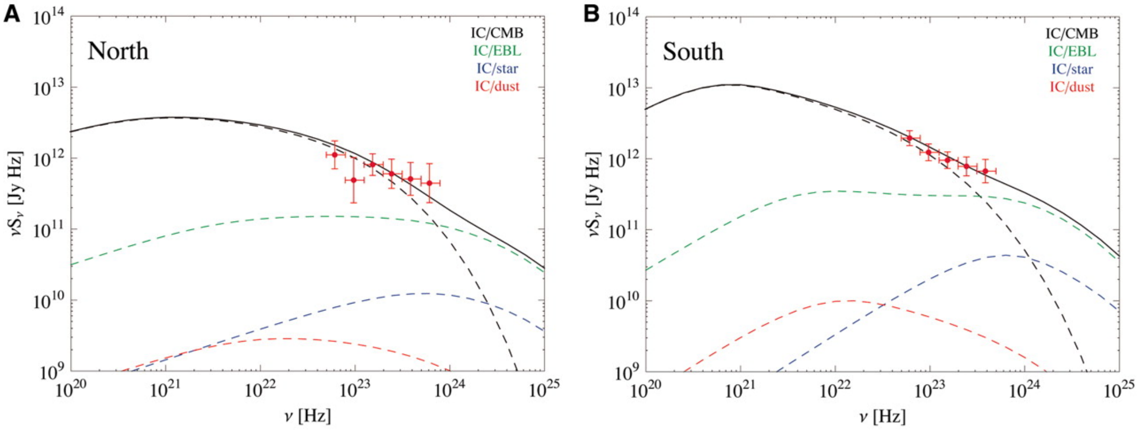

Figure 6.3: Detailed SED of emission from each lobe of Cen A with 10 month LAT data points showing IC contributions from each seed photon field. [25]

age `fermipy`[1] (see Sect. 3.4.2) v0.16.0 and LAT Science Tools v11-07-00, we set up a binned likelihood analysis with spatial binning size 0.1° and 8 bins per decade in energy. We utilized the Pass 8 PSF types by splitting the data into 4 components, where the first selects the PSF0 event type (`evtype` 4) and maximum zenith angle 70° and applies the isotropic model `iso_P8R2_SOURCE_V6_PSF0_v06.txt`; the second, PSF1 (`evtype` 8), 75°, and `iso_P8R2_SOURCE_V6_PSF1_v06.txt`; the third, PSF2 (`evtype` 16), 85°, and `iso_P8R2_SOURCE_V6_PSF2_v06.txt`; and the fourth, PSF3 (`evtype` 32), 90°, and `iso_P8R2_SOURCE_V6_PSF3_v06.txt`, respectively. This allows us to have the greatest spatial resolution possible. We applied the instrument response function `P8R2_SOURCE_V6` and the galactic interstellar emission model `gll_iem_v06.fits`. We did not turn on energy dispersion because spectral information is not the primary focus of the analysis and it is more computationally intensive.

6.2.1.1 γ-ray Morphology and Background Modeling

We populated the ROI model with sources from the Preliminary LAT 8-year Point Source List (FL8Y)[2] and changed the spectral model of the Cen A core to broken power law with break energy 2.8 GeV, following the results of Chapter 5. We deleted from our model the catalog's Cen A lobes model along with all point sources which were marked as unassociated. We did this because we suspect many unassociated sources in this region may be modeling what is actually diffuse lobe emission. We then began an iterative process of 1. finding unmodeled point sources, 2. searching AGN catalogs using the

---

[1] `http://fermipy.readthedocs.io/en/latest/`

[2] `https://fermi.gsfc.nasa.gov/ssc/data/access/lat/fl8y/`

locations of the new point sources which spatially coincide with the latest template for a possible known blazar background source, deleting all but the assumed background point sources from the ROI model, and optimizing, and 3. creating a new γ-ray template from the excess emission and adding it to the ROI model. In this manner, we are simultaneously converging on a γ-ray morphology of the Cen A lobes while developing an optimized background model. In the special case of the first iteration, we create a temporary morphology from the excess after step 1, since we have no γ-ray template yet available. During this entire convergence process, we keep the isotropic and galactic diffuse models fixed to their design amplitudes with normalizations equal to 1. We do this because the unmodeled lobe emission significantly skews the ROI fit of these diffuse sources to unrealistic normalization values. Upon completion of the γ-ray morphology extraction, these diffuse sources are allowed to vary and they converge to realistic values. We required 3 iterations to converge on a template morphology which models the data well.

This method relies on two assumptions: all new point sources found which are spatially coincident with the γ-ray lobes and cannot be identified with high confidence as a known blazar are assumed to be modeling lobe emission, and that the shape of each lobe is generally contiguous from our perspective. That is, we assume there are not unconnected islands of emission associated with the lobes.

For the first step, we utilize the `fermipy` function `GTAnalysis.find_sources()`, allowing only new sources which have a TS > 9. For each of the first two iterations, 20 new sources were found. For the third, none. In the special case of the first iteration, we then extract a temporary morphology from the excess emission in order to have information for spatial coincidence in step 2. Since much of the lobe emission is being modeled as several point sources, all that is left is diffuse and only slightly above the noise level. We created two TS maps using the `fermipy` function `GTAnalysis.tsmap()` to find regions of unmodeled emission, one with the full energy range and one cutting out data below 1 GeV. We use the Canny edge-detection algorithm [102] on both maps to programmatically identify edges of the lobes. The first stage of the Canny process is a Gaussian filter, whose radius we slowly increase just until the lobes appear as a closed shape. Finally, we measure the distance from each added point source to the closest spot on the Canny lobe edges and call everything within 1° as spatially coincident (1° is approximately the 68% containment angle PSF of the LAT at 1 GeV, see Fig. 3.9).

For the second step, we start by optimizing the localization of each new point source and getting containment uncertainties using the `fermipy` function `GTAnalysis.localize()`. During each localization, we allow the spectral parameters of all sources within 3° of the SOI to freely vary. Then, we search AGN catalogs using the ASDC Data Explorer Tool[3] for spatially coincident known blazars within the 99% containment circle. In the first iteration, we could find no known blazars coincident with the 20 added point sources. In the second, we found that 4 of the 20 added sources were coincident with possible known blazars.

For the creation of templates from γ-ray data, we used TS maps, which are good at showing regions of unmodeled emission. We confirmed this method works well at reproducing source morphology by testing with simulated LAT data and various template morphologies. In particular, we use the predicted counts (npred) map generated by `GTAnalysis.tsmap()` within `fermipy`, which was shown in our simulation tests to pro-

---

[3] `https://tools.ssdc.asi.it/`

duce optimal results. For every iteration, we separated the TS map into north and south lobe templates by cutting at the latitude of the Cen A core (DEC= $-43.0°$). We used TS maps which assume a power law spectral index equal to our current best guess of the index for each region in question. Then, to eliminate the background, we subtracted a constant threshold value from each map and then set all negative values to zero. This threshold value was chosen as the smallest amount that created a clear separation of the lobes from the background. After that, we eliminated stray regions of background from the edges of the map by setting to zero. The new templates were then applied to the ROI model with a power law spectral model and the ROI model was optimized.

In the first iteration, we used TS maps assuming a power law index found for each lobe by taking a weighted average of the indices found by Sun et al. 2016 [45]. The TS maps used were created from the full analysis energy range. During creation of this first map, we noticed the existence of what appears to be a long tail which stretches out from the south lobe to the east. This tail disappears completely in TS maps made above 1 GeV, implying it is soft and/or faint, but more importantly, that it seems to have a significantly different spectrum. Because it is significantly distinct, we separated off this tail by cutting the south TS map along RA=205°, which is at the outer edge of the south lobe, and analyzing it separately.

For the second iteration, because we observed the previous templates to be insufficient at fitting spectral changes across the lobes, we separated the templates into two energy ranges: 100 MeV–1 GeV and > 1 GeV. These templates were then applied to the model only in their designed energy ranges. The tail was no longer visible in either of these maps, and we believe that is because it is too faint to appear when the full energy range isn't being used. The tail always appears in TS maps made with the full energy range, and it is clearly visible as excess when applying these second templates.

Finally, for the third template, we also separated off the hotspot feature from the high energy map via a hard cut 16 pixels (1.6° of right ascension) by 15 pixels (1.5° of declination). After applying these 5 new templates (north lobe high energy, north lobe low energy, south lobe high energy, south lobe low energy, and southern hotspot) and optimizing the ROI, we made a final TS map from the excess in which only the southern tail feature is visible. Upon creating a tail template from this, applying it to the model, and reoptimizing, we observed that a residual map no longer shows significant excess across the ROI and a histogram of the residual significance map is well-fit to a normal distribution centered at zero, thus confirming the ROI model with these templates is a good fit to the γ-ray data. Each of these finalized extracted morphologies is shown in Fig. 6.4.

6.2.1.2 Checks on Morphology

We wanted to confirm the existence of the fine structures present in the extracted morphologies. We tracked the likelihood of the model as a fit to the data while varying the sigma parameter of a 2-dimensional Gaussian filter operating on each extracted template. We started each likelihood profile from the best fit model from Sect. 6.2.1.1. We allowed the normalization parameters of all sources within 4 degrees of the center of the tested template to vary, as well as the template's power law index. We increased the sigma at each point by an amount small enough to observe small deviations in the log(likelihood).

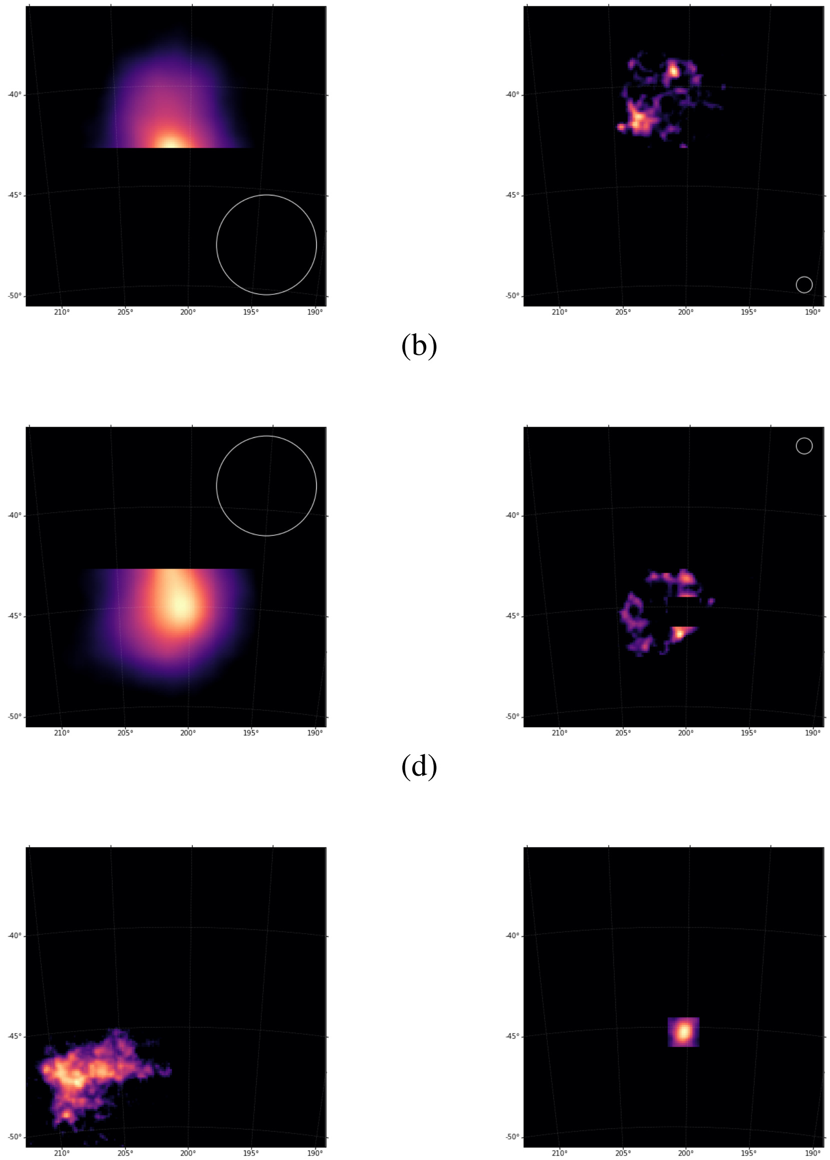

(a) (b)

(c) (d)

(e) (f)

Figure 6.4: 9-year γ-ray morphology of the outer lobes of Cen A extracted from *Fermi*-LAT data as described in Section 6.2.1.1. Plots (a) and (c), respectively, show the north and south lobe images below 1 GeV. Plots (b) and (d), respectively, show the north and south lobe images above 1 GeV. Plot (e) shows the extended southern tail feature and plot (f) shows the bright hotspot feature, both of which are applied across the full analysis energy range. The overlayed white circles shown on plots (a) – (d) show the largest possible 68% containment PSF within the template's energy range.

Data from this test on each of the templates is shown in Fig. 6.5.

We can see from these plots that the low energy templates are not very sensitive to Gaussian smoothing, whereas the high energy templates are very sensitive to smoothing. This indicates that the fine structures visible in the high energy templates are statistically significant, because the overall likelihood drops quickly upon removing them. The Gaussian filter σ values at which the $\log\mathcal{L}$ drops by 0.5 (i.e., TS = 1 or 68% confidence) are shown in Table 6.1.

6.3 Results

The best-fit spectral parameters and TS of each template is shown in Table 6.1. We calculated spectral energy distributions for each template using the same energy binning as the analysis. These are plotted in Fig. 6.6. We observed an inconsistency in the photon index across the best-fit spectra of the templates, the most unique being the south lobe hotspot.

We calculated energy flux light curves for each template using time binning on the available statistics. The two templates with sufficient statistics, the south hotspot and the north lobe (low), were binned in 30-day time bins. The south lobe (high and low) and the north lobe (high) were binned into 107-day time bins, and the tail into 1.2-year time bins. We did not detect variability with any of the templates except the southern hotspot, where we observed marginal variability with 3.2σ confidence ($\mathrm{TS}_{var} = 165.4$, 115 DOF).

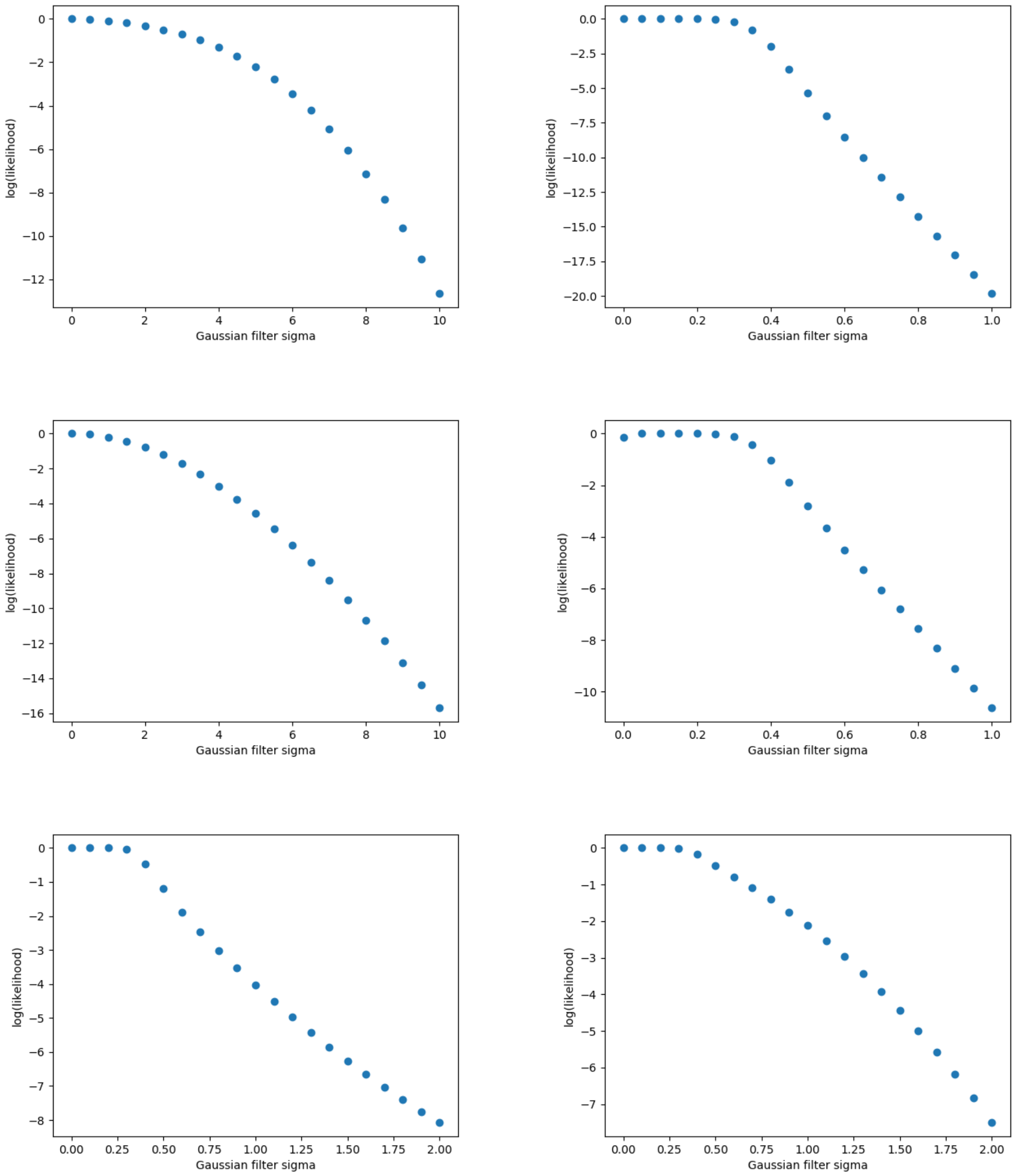

Figure 6.5: Likelihood profiles of each extracted γ-ray template while applying a 2D Gaussian smoothing filter with variable sigma. The filtered templates applied are arranged here correspondingly with their arrangement in Fig. 6.4.

Table 6.1: Best-fit spectral parameters associated with each of the six independent extracted lobe morphology templates.

Template	TS	Photon index	Full band photon flux (ph cm^{-2} s^{-1}) $\times 10^{-8}$	Full band energy flux (MeV cm^{-2} s^{-1}) $\times 10^{-5}$	68% spatial confidence 2D Gaussian filter σ
Cen A North Lobe < 1 GeV	1060	2.46 ± 0.07	10.0 ± 0.5	2.17 ± 0.08	2.5
Cen A North Lobe > 1 GeV	475	2.06 ± 0.05	0.42 ± 0.02	2.1 ± 0.2	0.35
Cen A South Lobe < 1 GeV	232	2.4 ± 0.4	6.1 ± 0.6	1.4 ± 0.2	1.5
Cen A South Lobe > 1 GeV	327	2.17 ± 0.06	0.39 ± 0.03	1.6 ± 0.2	0.35
Cen A Tail	91	2.22 ± 0.08	2.2 ± 0.3	1.0 ± 0.2	0.4
Cen A Hotspot	1520	2.60 ± 0.04	7.0 ± 0.4	1.85 ± 0.07	0.5

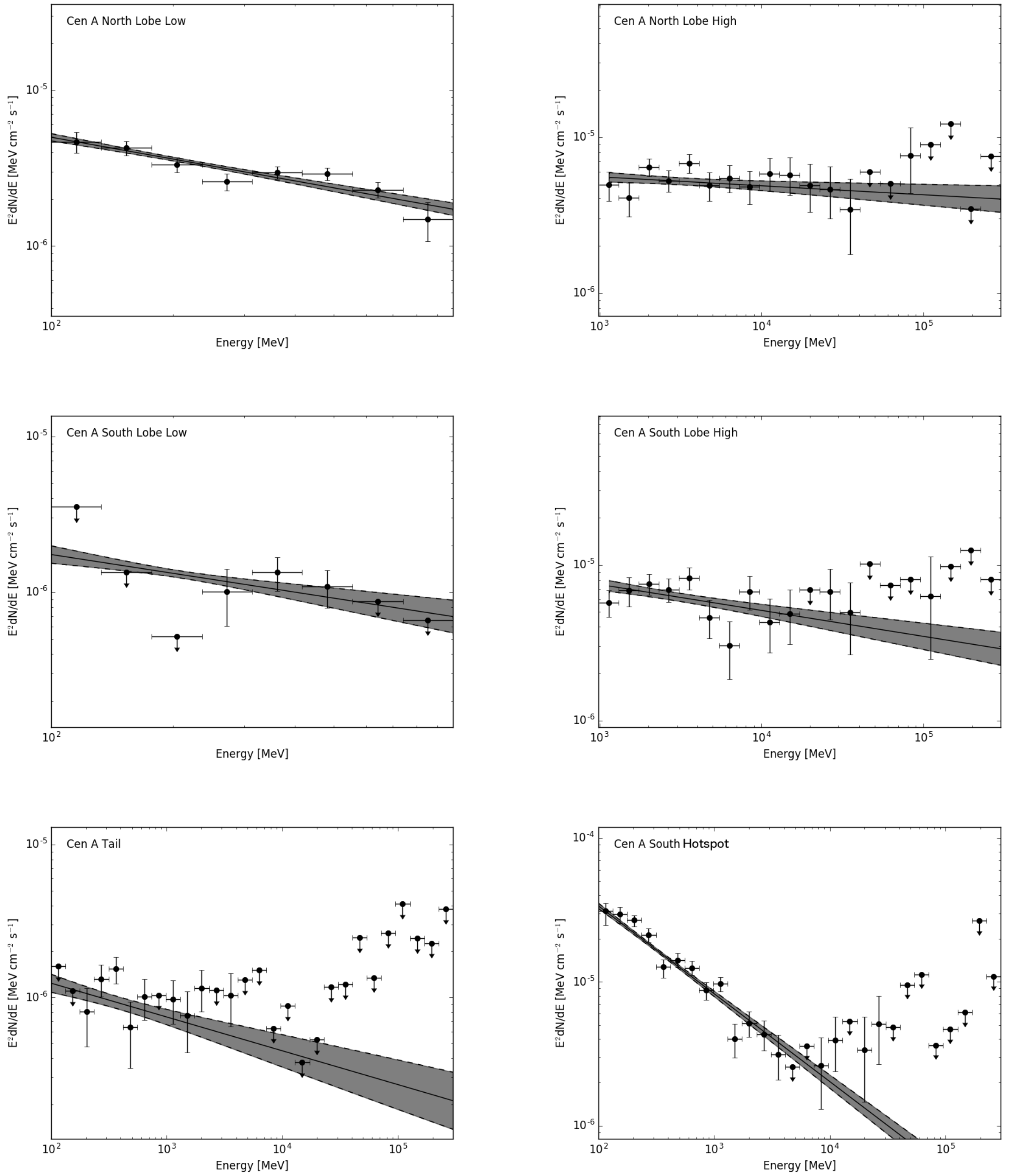

Figure 6.6: SEDs of each of the six independent lobe templates. The SEDs are arranged here correspondingly with their arrangement in Fig. 6.4.

Chapter 7: Discussion

7.1 Fornax A

Our *Fermi*-LAT study of the region around Fornax A consistently shows that, under all tests performed, the γ-ray emission region is significantly extended and the most likely spatial distribution is delineated by the radio lobes. Using a size-optimized flat disk model, extension beyond a point source was found to be significant at 5.9σ confidence, with a preferred radius of $0.^\circ 33 \pm 0.^\circ 05$. Modeling the emission as two point sources results in a western point source well matched to the radio lobe centroid and an eastern point source offset from the eastern lobe. This model is preferred over a single point source at the 4.8σ level. Furthermore, using the 1.5 GHz VLA radio morphology [9] as a template in combination with a central core point source results in a significantly greater likelihood than the point source alone with 6.0σ confidence. Contamination from the core is determined to be at most 14% based on a likelihood fit with the radio lobes template and a point source at the core location. While it is difficult to determine the exact morphology of the γ-ray emission, our study shows that it cannot be fully described as a point-like source.

A few scenarios could explain the offset γ-ray point-source localization seen in the 3FGL and in the single point-source analysis presented here. Firstly, since we now know the emission is extended (or at least not point-like), to use a point-source model to localize the emission is to start with a false assumption. The distribution of the γ-ray emitting regions may not be uniform across the lobe structure and thus would not result in a symmetric distribution of γ-ray emission. Second, based upon the offset eastern lobe point-source localization (point E in Figure 4.1), the existence of a background γ-ray source is not ruled out. However, adding a point source to the lobes template model and localizing with `gtfindsrc` yields only a slightly better fit at the 2.7σ level (see point C in Figure 4.1). We also find no evidence for variability in this source over ~ 6 years of observations. Variability might support the presence of a common background source such as a blazar. We note that another potential source that has been investigated in this region is the Fornax cluster [103, 104] whose center lies $3\overset{\circ}{.}6$ northeast of the Fornax A core, and may be contributing contaminating γ-ray flux from various cluster constituents. However, no galaxy cluster has been detected in γ rays so far.

Fermi-LAT data have been previously used by [44] to study Fornax A. They reported a photon flux above 100 MeV of 6.7×10^{-9} ph cm^{-2} s^{-1} using a point source spatial model, and our finding using the lobes template was close at $(5.7\pm0.9)\times10^{-9}$ ph cm^{-2} s^{-1}. Our study establishes for the first time spatial extension of Fornax A in γ rays, and distinguishes between γ-ray contributions from the core and lobes. This result was enabled thanks to the improvements brought about by the new Pass 8 event reconstruction, rather than the marginal increase in exposure time (i.e., 6 years of data in our study instead of 5 years in theirs).

7.1.1 Leptonic Modeling

The γ-ray emission was modeled following Georganopoulos et al. 2008 [11], in which the relativistic electrons in the lobes of the radio galaxy are IC scattered off of CMB and EBL photons. For details of how this model was created, see the publication on this work [1].

This model is shown along with the γ-ray spectral energy distribution and the radio-to-sub-mm measurements of the total emission from the lobes presented in [11] in Figure 4.5. Note that because Fornax A is an extended source in other wavelengths as well, care must be taken in defining the spatial structure in all wavelengths in order to draw meaningful comparisons. This model makes use of currently available *total* lobe fluxes. *WMAP* and Planck fluxes reported by [44] were obtained using resolution-dependent apertures that did not fully enclose the extent of the synchrotron lobe emission. The extracted spectral data points do not appear to match the predicted model shape based on IC/EBL emission alone. Fully accounting for the *Fermi*-LAT observed fluxes under the IC/EBL hypothesis alone would imply an EBL level that is even higher than the Stecker model [24], which was ruled out [105]. Consequently, the applied leptonic model cannot completely explain the observed emission. The model relies upon the assumption that all of the X-ray flux observed from the lobes is created by IC/CMB scattering to obtain the magnetic field strength. If some amount of the X-ray flux is thermal emission [61], our expected IC/EBL level would decrease, creating further discrepancy between model and data.

As discussed in Section 4.2.2.3, a more physically motivated choice of spatial template would be the higher-frequency *WMAP* data. However, the resulting changes in flux and spectral shape should be within the statistical errors of our current results, and therefore should not alter our result that the flux exceeds the leptonic model of the Fornax A lobes.

Note that the intensity of the IC contribution from the host galaxy photons of Fornax A is comparable to that of the EBL photons in the lobes, and it actually dominates at higher energies ($> 1\,\mathrm{GeV}$, see Figure 4.5). This differs from the case of Centaurus A, wherein the predicted EBL photon intensity is roughly five times that of the starlight [25]. Were it true that host galaxy photons dominate in Fornax A, the expected spatial distribution of γ rays from the lobes would not be uniform, with brighter emission nearer the center and less away from the core. Testing for this feature requires spatial resolution that is beyond the capabilities of the LAT with current statistics.

7.1.2 Hadronic Modeling

The problem of the model not fitting the γ-ray spectrum in Fornax A may be solved by an additional contribution from hadronic cosmic rays interacting within the lobes, as found by [44]. A model of hadronic emission (proton-proton interactions) was created assuming a total emitting volume of $7 \times 10^{70}\,\mathrm{cm}^3$, a uniform distribution of thermal gas with number density $3 \times 10^{-4}\,\mathrm{cm}^{-3}$ following [61], and a power-law cosmic-ray spectrum with energy index 2.3 extending from $\sim 3\,\mathrm{GeV}$ up to more than $10\,\mathrm{TeV}$. Modeling the γ rays as entirely hadronic in origin requires a large total cosmic-ray energy of $\sim 1{\times}10^{61}$ erg, which is twice the observed energy of $\sim 5 \times 10^{60}$ erg in the lobes of comparable radio galaxy Hydra A [69] and very high compared to an estimate of $\sim 5 \times 10^{58}$ erg in the outburst that is assumed to have created the lobes of Fornax A [106]. We then subtracted the lowest IC/EBL model [23] from our LAT spectral points and fit the residual flux as hadronic emission, and found we could achieve a reasonable fit, shown in Figure 4.5. The resulting cosmic-ray pressure fitted from this residual flux is $\sim 2\times10^{-11}\,\mathrm{dyn\,cm^{-2}}$ and the total energy contained in cosmic rays is $\sim 5\times10^{60}$ erg. This total energy is similar to that of Hydra A [69] and closer to an estimate of the total energy in the Fornax A lobes [106]. This result agrees with analogous calculations [44], in which the discrepancy is explained by suggesting the emission is primarily hadronic and localized to relatively denser sub-structures within the lobes, thereby decreasing the effective emitting volume. Later, we discovered direct evidence of fine sub-structures in the lobes of Cen A in HE γ rays (see Sect. 7.3).

7.2 Cen A Core

Prior to this study, the available data making up the broadband SED of the Cen A core showed good agreement with a simple leptonic synchrotron/SSC model, featuring the double bump structure as is commonly seen in blazars (see Sect. 2.3.1) [89]. However, the findings in this study of a high flux in the VHE regime and an apparently matching spectral break in the HE regime contradict this simple model. Shown in Fig. 7.1 is the broadband SED of Cen A, consisting of archival data from Meisenheimer et al. 2007 [79] covering the radio, mm-, infrared and optical bands except for points at 8.4 GHz and 22.3 GHz from TANAMI [107] replacing three older radio data points, hard X-ray 18 keV–8 MeV points from INTEGRAL SPI [108], low energy γ rays between

1 and 30 MeV from COMPTEL [87, 109], and HE and VHE γ rays from *Fermi*-LAT and H.E.S.S. It should be noted that with their reduced spatial resolution, INTEGRAL with $2^{\circ}\!.5$ and COMPTEL with 4°, their flux levels could contain contributions from the extended jet and inner lobes. While this broadband data was not observed contemporaneously, we would not expect significant differences at other times since we could not find evidence of variability.

These new data from *Fermi*-LAT and H.E.S.S. are incompatible with the SSC model as previously reported [89], and therefore demand an alternative or additional explanation. One possible explanation is a dual-zone SSC model instead of the simple single-zone. Our fit of a dual-zone SSC model to this broadband SED is shown in Fig. 7.1. Details about how this model was built can be found in the publication on this work [2]. Our modeling shows that, while other explanations for the new spectral feature are possible, a dual-zone SSC is one possibility.

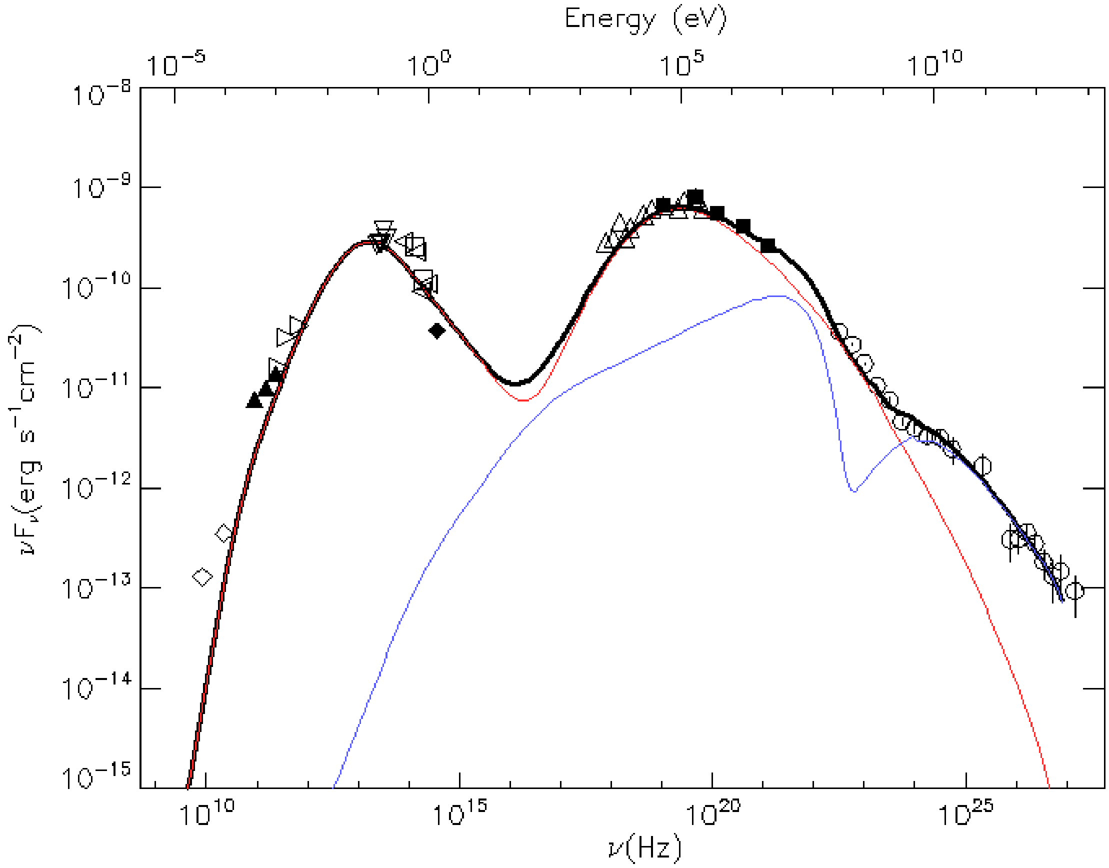

Figure 7.1: SED of Cen A core with model fits as described in text. The red curve corresponds to an SSC component designed to fit the radio to sub-GeV data. The blue curve corresponds to a second SSC component added to account for the highest energy data. The black curve corresponds to the sum of the two components. SED points as derived from H.E.S.S. and *Fermi*-LAT data in this study are shown with open circles. This figure is reproduced here from the publication [2].[2]

---

[2] Observations from the radio band to the MeV γ-ray band are from TANAMI (◇), SEST (▲), JCMT (▷), MIDI (▽), NAOS/CONICA (◁), NICMOS (□), WFPC2 (◆), *Suzaku* (△), OSSE/COMPTEL (■).

7.3 Cen A Lobes

This study was motivated by the curious γ-ray emission observed well beyond the known extent of the Cen A outer lobes as shown in Fig. 6.1. This emission appears to defy our understanding of the content and radiative processes of the lobes, because the γ-ray emission is assumed to come from relativistic energy particles scattering off of background photon fields such the CMB, and it is not clear how particles with such energy could have traveled so far from the active core without cooling, or why these particles are not also producing bright radio emission as is usually the case.

Take, for example, the bright region of residual γ-ray emission with TS > 25 in the northern part of Fig. 6.1. This region is $\sim 4.3^\circ$ in angular separation from the Cen A core, which, assuming a distance of $\sim 3.8\,\mathrm{Mpc}$ [73], implies a physical separation of $\sim 280\,\mathrm{kpc}$ away from the core. If the particles originate at the core and travel at the speed of light, they would be $\sim 9.1 \times 10^5$ years old upon arrival. The cooling time half-life of γ-ray-producing electrons via the synchrotron process in a typical scenario using Eq. 2.2 is a few hours. In a purely relative sense, it should still be true that the radio-producing particles should be allowed to travel farther than the γ-ray-producing particles by several orders of magnitude, but we observe γ-ray photons farther away than radio.

From our process of extracting morphology from the γ-ray emission from the outer lobes of Cen A, we converge on 6 separate images. Among them is an unanticipated ‘tail’ feature beyond the southeast region of the lobes. This feature entered the analysis as a result of the unbiased procedure of mapping out diffuse emission contiguous with the existing known scope of the lobes. The tail may or may not be truly associated with the lobes, but the only other alternative is that it is foreground emission from the Milky Way Galaxy. However, this is less likely when the spectral shape is considered. Galactic interstellar γ-ray emission usually has a photon index of 2.6–2.7 [99, 110], but the best-fit photon index of the tail from this analysis is 2.22 ± 0.08. Also, it would be unusual to observe such an island of galactic diffuse emission above the surrounding background. With these points considered, there is good evidence this tail is associated with the Cen A lobes. This leads to even further difficulties in explaining γ-ray emission so far away from the active core.

One of the features present in the extracted γ-ray lobe images, especially in the two created from $> 1\,\mathrm{GeV}$ photons where the spatial resolution is much better, is inhomogeneity and fine structure resembling filaments. Observational studies over the past few decades reveal filamentary structures in the lobes of radio galaxies, e.g. Cygnus A [111], 3C 310 [112], Fornax A [9], NGC 193 [113], B2 0755+37 [113], etc. However, there is still no consensus on the factor(s) responsible for the origin of the observed filamentary features. Recent Giant Metrewave Radio Telescope observations at 325 and 235 MHz radio frequencies detected filamentary sub-structures in the southern lobe of Centaurus A [114]. The study indicated that the filaments seem to have a higher pressure than the lobe. The authors interpreted the origin of the filaments in terms of weak shocks from magnetohydrodynamical turbulence or from a recent jet activity of the central AGN; it could also be an interplay of both. The XMM-Newton observations detected no excess X-ray emission from the filaments which indicates that the excess synchrotron emission in the filaments simply cannot be produced purely by excess number of electron (or emitting particles); the filament magnetic field strength must be higher compared to the lobe and greater than the equipartition value of the filament [115].

Our study, for the first time, detected the filamentary structure Cen A lobes at GeV energies. The existence of these fine structure filaments was confirmed via Gaussian smoothing tests as described in Sect. 6.2.1.2. This detection was made possible thanks to the improved sensitivity and angular resolution made available with Pass 8 LAT event reconstruction (see Sect. 3.3.1) as well as the new imaging technique as described in Sect. 6.2.1.1. See Table 6.1 for spectral parameters obtained from each extracted morphology. According to this γ-ray morphology, the outer lobes of Cen A extend about 9 degrees end-to-end and about 5 degrees in width, not including the possible tail feature extending to the southeast.

Several aspects of our observations of the lobes indicate the possibility of local re-acceleration of charged particles, as opposed to acceleration only occurring within the AGN core central engine. First, as explained above, the particles necessary for γ rays are simultaneously too far from the core and too high in energy to make sense originating at the core. Second, the existence of large regional of differences in emission across the lobes, both the filaments and the bright south lobe hotspot, suggest the presence of multiple emitting components. This is especially true of the hotspot, assuming it is not caused by the presence of a background object of some kind, as the observed photon index of 2.60 ± 0.04 stands out clearly relative to the surrounding emission, with photon indices between 2.17 and 2.4. Also, the intensity of the emission from this hotspot would not be expected of a collection of particles gradually falling off in energy away from the core. Furthermore, the marginal variability we observe in the hotspot would seem to indicate possible activity away from the AGN core. Some unknown form of local re-acceleration, potentially from magnetohydrodynamical and/or kelvin-Helmholtz instabilities, may explain these observed phenomena.

Another interpretation comes from the question of whether or not charged particles are being trapped by a magnetic field as they travel outward. We are confident of a magnetic field wherever we observe low energy radiation in the radio and microwave bands, because it is very likely to be produced from the synchrotron process, which requires a magnetic field. We also know that the lobes are not homogeneous in radio, and thus the magnetic field is likely not truly homogeneous. If some of the charged particles created from the AGN jet were to avoid the filaments of high magnetic field, their cooling time would be longer, and thus they could travel farther. If some of the particles were escaping the field, then the higher energy ones would be able to travel farther than the lower energy. This may be another explanation for such high energy GeV γ rays beyond the radio lobes: they are made from relativistic charged particles which have not been trapped by the magnetic fields in the synchrotron-producing regions and which travel farther than lower energy particles.

Chapter 8: Conclusions

We investigated the HE γ-ray emission from two radio galaxies, Fornax A and Cen A. We can compare them as examples typical of radio galaxies and AGNs (see Chapter 2), however there are clear differences between them that may limit the usefulness of such a comparison. While Cen A shows features more typical of FR 1 type radio galaxies, it does not completely fall neatly into that category, since Cen A does appear to feature a prominent hotspot like an FR 2 radio galaxy although not at the edge as is normal for FR 2s. The classification of Fornax A is also unclear, with its wide and separated lobes like an FR 2 type, but no visible hotspots like an FR 1 type (see Sect. 2.2.2 for an explanation of FR types).

We have known for some time that radio galaxies produce γ rays, among their emission in many other bands. As mentioned in Sect. 2.1, Cen A was the first radio galaxy detected in HE γ rays with EGRET, along with 66 other positively identified AGNs. It could not yet be distinguished, however, between γ rays from the core and lobes. Starting in 2008 with its more advanced instrumentation as described in Chapter 3, the *Fermi*-LAT allowed us to observe radio galaxies much more clearly, and thereby learn much more about them.

By 2010, the LAT observed radio galaxy lobes for the first time with HE γ rays with

Cen A, finally being able to distinguish lobe from core emission. The lobe emission was found to fit a model of synchrotron and external-Compton emission, with seed photons primarily from the CMB (see Sect. 2.3.1 and Appendix A) [25]. The core emission was found to fit well from radio through HE bands with a blazar-style synchrotron/SSC model, however, there were already hints of anomalous VHE emission [81].

With the discovery of extended emission from Fornax A in Chapter 4, it became the second radio galaxy known to produce HE γ rays from within the galaxy lobes. In fact, though not as clear as the picture available with Cen A (because of its distance, and thus, angular size), we were able to largely rule out core emission as at most $\sim 14\%$ of the total observed flux. With its assumed lobe origin, the Fornax A γ-ray emission was found to be too luminous for the simple IC/EBL leptonic model (see Sect. 7.1.1), even using the highest EBL models currently proposed. Hadronic modeling was investigated as an alternative in Sect. 7.1.2, however the energy requirement was found to be unrealistic. One solution to this is the possibility that the γ-ray emission in the Fornax A lobes is confined to denser filamentary sub-structures, as was discovered here in the lobes of Cen A in Chapter 6.

Our spectral picture of the bright core of Cen A was enhanced with a joint *Fermi*-LAT and H.E.S.S. study in Chapter 5. The anomalous VHE emission previously reported [81] was confirmed, along with a matching discovery of an upward spectral break in the HE γ-ray band. Together, these definitively conflict with a conventional single-zone SSC model. This could be explained with the addition of a second zone of SSC which dominates the spectrum above ~ 2.8 GeV. These findings seem to set Cen A apart from Fornax A, with its core seemingly undetected in HE γ rays.

Along with the extended exposure time and increased spatial resolution thanks to the release of Pass 8 (see Sect. 3.3.1), a new technique for imaging using *Fermi*-LAT data was developed and applied to the outer lobes of Cen A, described in Chapter 6. This yielded a discovery of fine and probably dense γ-ray-emitting filamentary sub-structures there. This was the first time the *Fermi*-LAT was used to observe such diffuse substructure from any celestial object, and the first time these were observed in radio galaxy lobes from γ rays. Filamentary structures in the Cen A lobes have been seen in radio bands, and in other radio galaxies as well. In Sect. 7.3, it was explained how the observed filaments and the south lobe hotspot as well as the presence of γ-ray emission farther out than radio emission could indicate that local re-acceleration is taking place away from the core. Another explanation for the γ-ray emission outside the radio may be possible: since the synchrotron morphology contains filaments, the magnetic field does not fill all space of the lobes, leaving gaps for high energy particles to escape the lobes and finally scatter with the CMB via the IC process.

8.1 Future work

Our modeling for Fornax A was done using previously published multiwavelength data. Further analysis in other wavelengths in the future will yield a more definitive picture of the SED. More detailed observations, such as with the hard X-ray telescope *NuSTAR*, would help determine if the X-ray emission is contaminated by thermal processes [61], which would test our initial assumptions that the radio data traces the X-rays and γ rays, and that the X-rays could be used to constrain the lobe magnetic field. Observations at MeV energies should provide more information about the IC/CMB component [64], where the emission is assumed to be much brighter than at GeV. Potentially with greater statistics, the *Fermi*-LAT or a telescope at VHE could extend the lobes' detection to higher energies and additionally observe the effect of the host-galaxy photons on the spatial distribution of γ rays in the Fornax A lobes.

Despite their faintness at γ-ray energies, radio galaxies such as Cen A are emerging as a unique γ-ray source population offering important physical insight beyond what could usually be achieved in classical blazar sources. With its increased sensitivity, the Cherenkov Telescope Array is expected to probe deeper into this and help to eventually resolve the nature of the γ-ray emission in the Cen A core.

As shown in Fig. 6.2, the lobes are predicted to be more luminous in the MeV range than in any other. Naturally, a space-based telescope optimized for the MeV range such as the proposed All-sky Medium Energy Gamma-ray Observatory (AMEGO) should teach us a lot about these strange diffuse structures. AMEGO, making good use of both the Compton detection process between 0.2 and 10 MeV and the pair conversion process between 10 MeV and 10 GeV, would be able to fill in theses gaps in our observation (see Fig. 8.1). Additionally, with a much better PSF at 100 MeV than *Fermi*-LAT ($\sim 1^\circ$ instead of $\sim 10^\circ$, see Fig. 8.2), AMEGO has the potential to spatially resolve fine features at lower energies where it is difficult with the LAT. See, for example, the lack of features in the low energy templates in Fig. 6.4. AMEGO observations could reveal filaments at these lower energies.

Synchrotron radiation, when generated in an anisotropic magnetic field, is polarized. If the filaments of Cen A are indicative of some degree of order in the field, we

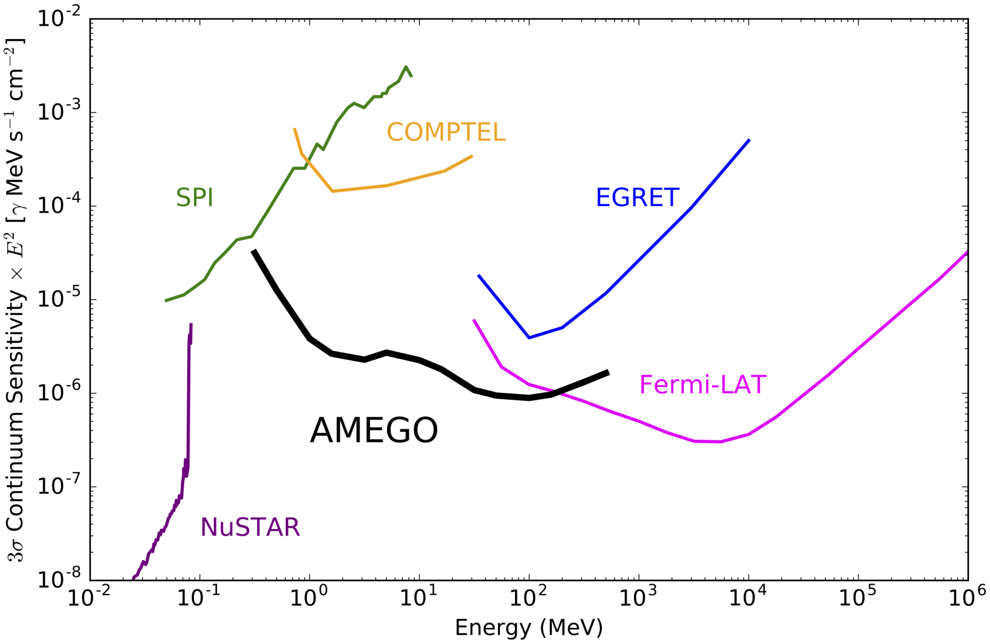

Figure 8.1: Sensitivity over energy of various astronomy observatories in the X-rays to γ rays.

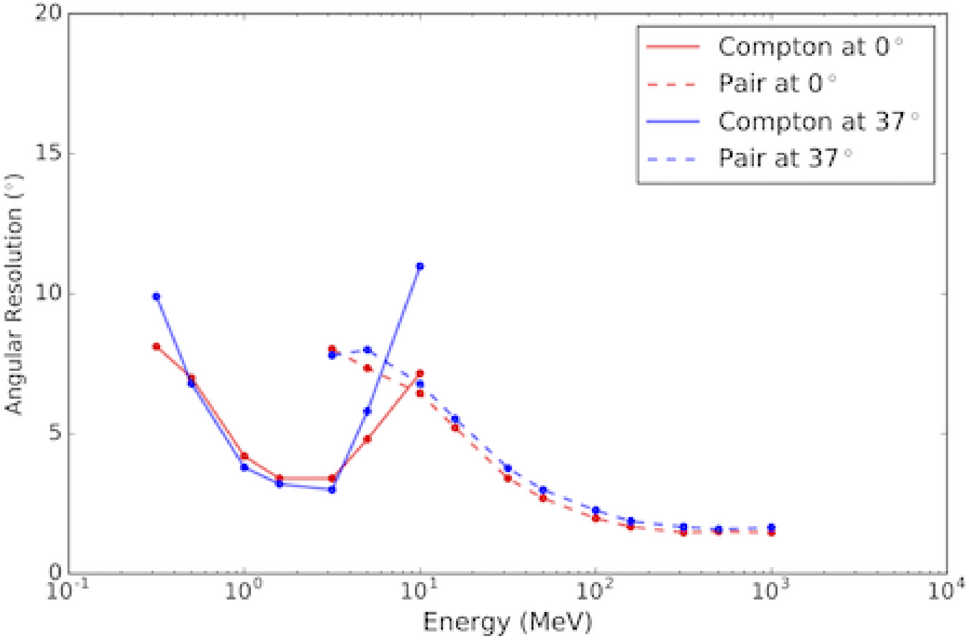

Figure 8.2: Angular resolution of the proposed AMEGO instrument, showing the difference between Compton and pair conversion events.

should be able to observe it with polarization imaging at MHz radio frequencies.

Appendix A: Diffuse extragalactic background radiation

Diffuse extragalactic background radiation refers to the combined photon radiation field in all frequency bands resulting from the Big Bang. Common names for the field are usually given according to the frequency band. As shown in Fig. A.1, the brightest band is in the microwave range, called the CMB. The CMB is the thermal black body radiation of the Universe [116] which has a temperature of 2.7260 ± 0.0013 K, according to data taken by *WMAP* [117]. The next brightest band is the EBL, which includes light in the ultraviolet, optical, and infrared (labeled CUVOB in Fig. A.1). The EBL is the diffuse radiation accumulated from star formation and AGNs. The EBL is much more difficult to measure because of zodiacal light, sunlight scattering off of dust particles in the Solar System. The EBL photon field is the cause for our inability to observe VHE γ rays from great distances, because VHE γ rays have a high probability of destruction via photon-photon interaction with EBL photons. This attenuation feature presents an opportunity to measure the EBL indirectly, as was done through γ-ray observations of blazars [105]. EC with the EBL and the CMB photon fields is important to radio galaxies, as it is assumed they are the only seed photons present with appropriate energy to be upscattered into γ rays in the region of the galaxy lobes.

---

[2] `https://commons.wikimedia.org/wiki/File:Extragalactic-background-power-density.jpg`

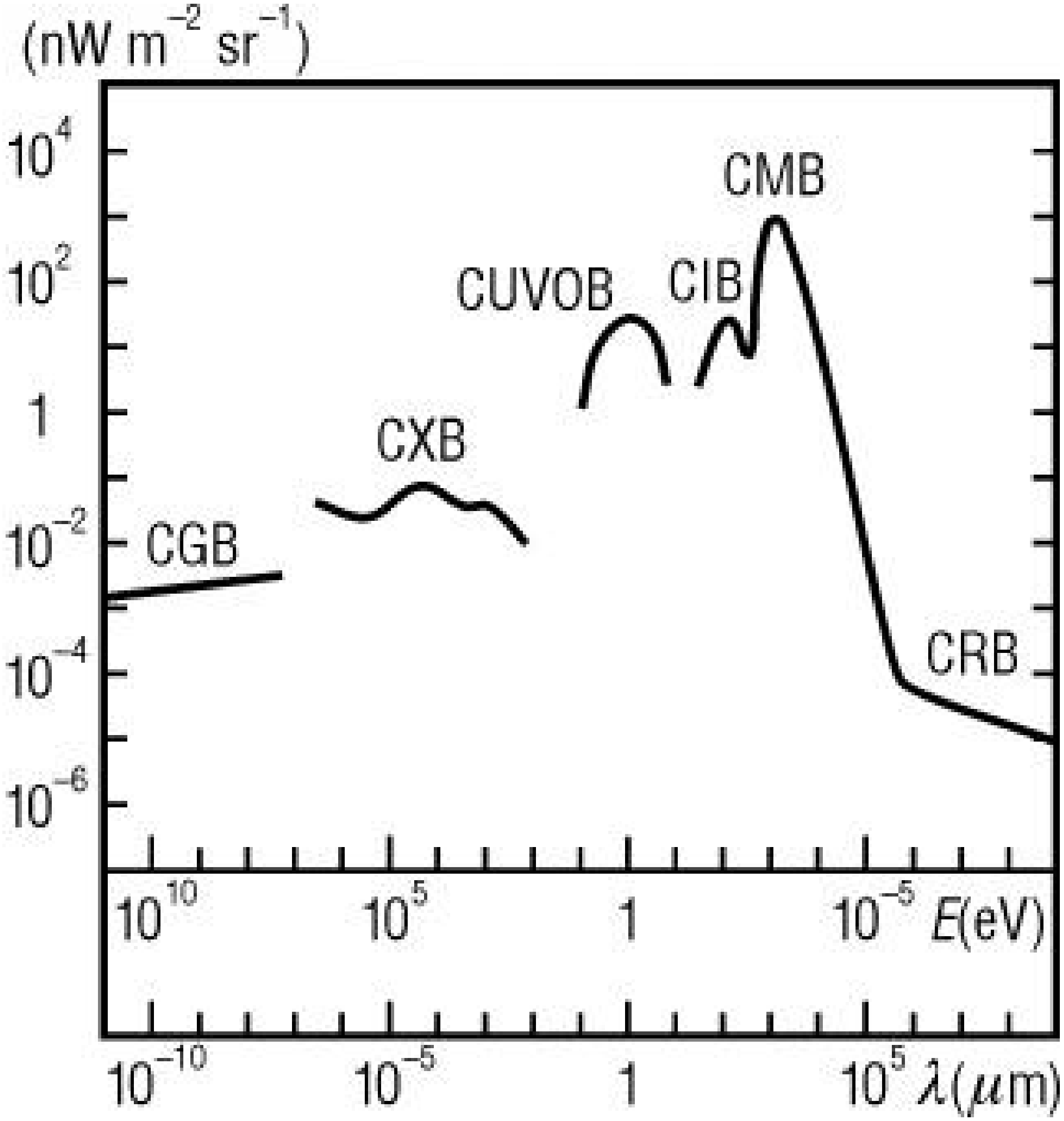

Figure A.1: Schematic representation of the spectral energy distribution of the diffuse extragalactic background radiation.[2]

Appendix B: Statistics

B.1 Parameter Estimation

Estimating higher-level parameters from the data begins by establishing a model of the ROI with a set of parameters μ and a procedure for mapping the chosen model and parameters to a binned map of model counts m, exactly matching the spatial and energy binning of the data counts n. This mapping must also include convolution with the IRF being assumed. For *Fermi*-LAT analysis, this is usually done using the `gtmodel` tool. Because the γ-ray data is an integer count of the number of events, the probability of the data counts given the model counts in each bin follows a Poisson distribution,

$$p(n|m) = e^{-m}\frac{m^n}{n!}.$$

The *likelihood* is the product of these probabilities from all bins,

$$L(m|n) = \prod_i p_i(n_i|m_i).$$

The likelihood then becomes a single number which is the probability of the whole ROI model and the chosen parameters being a good fit to the data. The full *likelihood function* $\mathcal{L}(\mu|n)$ is the value of the likelihood at any given selection of model parameters μ. It is a function of the model parameters given the data. It would be nearly impossible to write down the likelihood function analytically, but it could be mapped out numerically by running the calculation at all possible values of all model parameters. This can be prohibitively time-consuming, of course, especially with more numerous model parameters.

With the full likelihood function at hand, we can calculate the posterior probability distribution with our choice of the Bayesian prior π as

$$P(\mu|d) \propto \mathcal{L}(\mu|d)\pi(\mu),$$

where μ represents the set of model parameters and d represents the observed data. After multiplying, we then normalize to get P between 0 and 1. If we are only interested in a small subset of the model parameters, we can extract a probability distribution of the parameters of interest by marginalizing over the remaining parameters with

$$p(\mu_0) = \int P(\mu_0, \mu_1, \ldots) d\mu_1 d\mu_2 \ldots .$$

These parameters which are not of interest are called *nuisance* parameters, and they are often made of up parameters designed for modeling the background sources in the ROI. Here, μ_0 is the single parameter which we are interested in. In this work, only non-informative priors were used.

B.1.1 Maximum Likelihood

If we have the full likelihood function, the best estimate of the model parameters is the global maximum of the likelihood function. That is, the set of parameter values that have the greatest likelihood. Conveniently, even without access to the full likelihood function, we can often quickly estimate this maximum numerically by making small adjustments to the model parameters and climbing the path of steepest ascent until the maximum is reached, i.e., until no more small changes to the parameters yields greater likelihood. This is called the *maximum likelihood* technique. It is common to apply standard numerical minimization algorithms such as Minuit [52] to minimize the negative likelihood or log-likelihood. In order for this estimate of the maximum of the likelihood function to always closely match the true maximum, the function must be monotonic leading up to the peak and there must be only one maximum globally. These are assumed for the maximum likelihood done in this thesis.

Another approach to reducing the likelihood function to a subset of parameters is the *profile likelihood*. Instead of marginalizing over the nuisance parameters, we profile over them. This means finding the maximum of the full likelihood function at several fixed choices of the parameter of interest. Since this method requires choosing a range of model parameter values to calculate the profile likelihood, it relies on the assumption that the peak in the profile likelihood is not just a local maximum, but also the global maximum, so it helps to have corroborating estimates of roughly the correct global maximum. One such profile likelihood function which was calculated in this work is shown in Fig. 4.2 (copied here as Fig. B.1 for convenience). The specifics about how the plot was made are not important here (see Sect. 4.2.2.1 for details), only that there is a model parameter, disk radius, with its values being used on the x-axis and resulting changes in overall likelihood with each radius on the y-axis. The profile likelihood is the method which was used in this thesis.

With the maximum likelihood on its own, we end up with the best-fit parameters of the model we've chosen, but we have no information about the statistical uncertainties of these parameters. To obtain the credible region for a parameter, we can locate the values

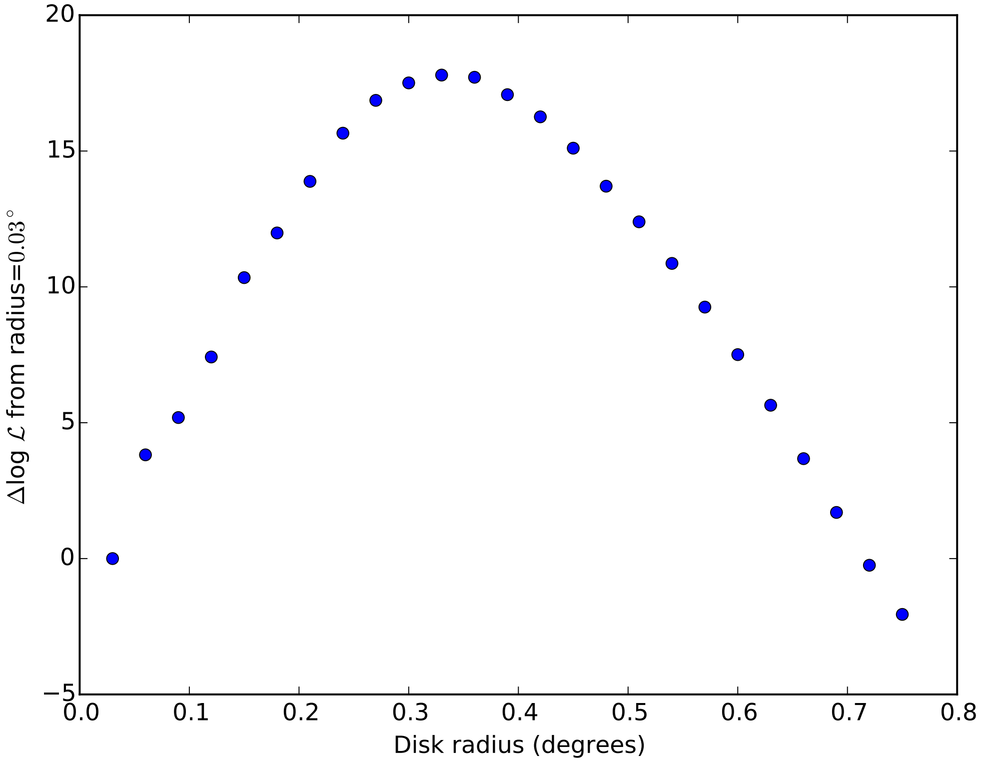

Figure B.1: Example profile likelihood

of the parameter for which the log-likelihood drops from its maximum by the amount matching your desired confidence level. These parameter values above and below the peak are the upper and lower ends of the credible region at the desired confidence level. If the peak is asymmetric about the maximum, these values will not be equidistant from the best-fit value. This procedure works to give us the desired credible region because we are actually using likelihood ratios and Wilks' Theorem (see Sect. B.2.1). In Fig. B.1, we can see that there is a maximum likelihood, it is clearly defined, and it is located at about a radius of $0\overset{\circ}{.}33$ with a log-likelihood of 17.3. We can then find a credible region with any choice of significance. For example, if we want to know the 68% 1σ uncertainty, we know that we need to find the location on the profile where the log-likelihood is 0.5 less than at the maximum, since that would give $\Delta \ln \mathcal{L} = 0.5$, $\mathrm{TS} = 2 \times 0.5 = 1$, and significance $= \sqrt{1} = 1\sigma$. We find from looking at Fig. B.1 that the profile reaches 16.8 approximately at radii of $0\overset{\circ}{.}28$ and $0\overset{\circ}{.}38$, therefore the 1σ uncertainty in the best-fit radius is $\pm 0\overset{\circ}{.}05$. The same process can be used to find the uncertainty in every parameter of the model.

B.2 Model Comparison

The comparison of two models H_0 and H_1 in how well the data favors H_0 over H_1 can be calculated using the Bayes factor

$$K = \frac{\int \mathcal{L}_0(\mu_0)\pi_0(\mu_0)d\mu_0}{\int \mathcal{L}_1(\mu_1)\pi_1(\mu_1)d\mu_1}, \tag{B.1}$$

where $\mathcal{L}_i$ is the full likelihood function, π_i is the prior probability distribution, and μ_i is the set of all parameters for each model. The integration occurs over all of the model

Table B.1: Common interpretation of the Bayes factor from Harold Jeffreys [3].

$K > 1$	H_0 supported
$1 > K > 10^{-1/2}$	Evidence against H_0, but not worth more than a bare mention
$10^{-1/2} > K > 10^{-1}$	Evidence against H_0 substantial
$10^{-1} > K > 10^{-3/2}$	Evidence against H_0 strong
$10^{-3/2} > K > 10^{-2}$	Evidence against H_0 very strong
$K < 10^{-2}$	Evidence against H_0 decisive

parameters. Smaller K corresponds to greater evidence against H_0 being favored by the data. More specific interpretation of the magnitude of the Bayes factor is up for debate, but one interpretation commonly cited is outlined in Table B.1. One strength of this approach is it automatically accounts for differences in the complexity and number of parameters, penalizing more complex models and thereby preventing overfitting. Another strength is it does not require the models to be nested.

In the context of multivariate maximum likelihood analysis, such as is used in this work, an approximation is often used in place of the Bayes factor. Without having access to the full likelihood function to compute this integral, it is possible to simplify Eq. B.1 into a ratio of likelihoods at their respective maximum values. This removes the advantages of automatically accounting for model complexity and introduces the requirement for nested models.

B.2.1 Likelihood Ratio Test

When comparing two models, a null model hypothesis with number of parameters m and an alternative hypothesis with number of parameters h where $h > m$, we start by defining the likelihood ratio

$$\Lambda = \frac{\mathcal{L}_0}{\mathcal{L}_1},$$

where $\mathcal{L}_0$ is the likelihood of the null hypothesis and $\mathcal{L}_1$ is the likelihood of the alternative hypothesis. Since the alternative hypothesis is fit to the same data with more parameters than the null hypothesis, it will always have a higher likelihood. So, while the ratio gives information about how much better the alternative is compared to the null, we need a formulation called Wilks' Theorem [71] to know how much better it needs to be for us to know if the alternative is significantly preferred. Wilks' Theorem, a formulation verified via Monte Carlo simulations [97], defines a value called the *test statistic* as

$$\mathrm{TS} \equiv -2\ln\Lambda = -2\ln\frac{\mathcal{L}_0}{\mathcal{L}_1} = 2(\ln\mathcal{L}_1 - \ln\mathcal{L}_0) \tag{B.2}$$

and then states that the TS is distributed like χ^2 with $h - m$ DOF. In order for Wilks' Theorem to be valid, i.e., for the TS to be distributed like χ^2, there must be sufficient data — at least roughly 10–20 total counts.

This provides us with the ability to turn the likelihood ratio into a p-value, the probability that the improvement from the alternative hypothesis is merely a fluke caused by random statistical fluctuation, or the significance (σ) that the alternative is preferred over the null. The p-value is equal to 1 minus the χ^2 cumulative distribution function of the TS with DOF $= h - m$, and the significance is the inverse normal cumulative distribution function of 1 minus the p-value/2. When DOF = 1, the significance is easily calculated as the square root of the TS.

However, it's not enough just for the alternative hypothesis to have a greater number of parameters, Wilks' Theorem only applies to a pair of models that are *nested*. When two models are nested, the alternative hypothesis can be used to exactly replicate the null hypothesis by fixing one or more of its parameters. For example, if the null hypothesis is a polynomial with degree 2 (so $m = 2$), such as $f_0(x) = ax + b$, and the alternative is a polynomial with degree 4 (so $h = 4$), such as $f_1(x) = cx^3 + dx^2 + gx + j$, then f_0 is easily reproducible from f_1 simply by fixing the parameters $c = 0$ and $d = 0$. Thus, f_0 and f_1 are nested models. However, another alternative hypothesis may not able to reproduce f_0, such as $f_2(x) = kx^3 + lx^2 + n$. Here, f_0 and f_2 are not nested models, but f_1 and f_2 are.

Looking again at the profile likelihood in Fig. B.1 and using Wilks' Theorem, we can compare the best-fit radius log-likelihood to the log-likelihood when the radius is roughly zero (in the plot this is shown as the zero point of the log-likelihood as well) to learn the significance of the existence of a radius. With its one additional parameter, the introduction of the radius increases the likelihood by 17.3, so $\ln \mathcal{L}_1 - \ln \mathcal{L}_0 \approx 17.3$, $\mathrm{TS} = 2 \times 17.3 = 34.6$, and thus the significance of the radius is $\sqrt{34.6} \approx 5.9\sigma$.

Appendix C: Light curves

A light curve is a form of astronomical data which shows the changes in flux or intensity over time. While the primary quantity represented is the source flux, individual spectral parameter changes over time can also be represented. A light curve is made by dividing the data into time bins, in addition to the usual space and energy bins, and then extracting the source flux within each window of time.

Light curves have many uses in time-domain astronomy, of course, such as studies of transients like gamma-ray bursts (GRBs). They are also very useful for studies of AGNs, because variability is frequently observed in blazars with HE γ rays. The lobes of radio galaxies, however, are assumed to be very constant emitters, since we have no evidence of local time-dependent activity. In the studies of the lobes of Cen A presented in this thesis (see Chapter 6), this light curve code was used to quickly calculate flux variability for each individual extracted piece of the lobe morphology, thereby shedding light onto the possibility of activity or the presence of an active background source, such as a blazar.

C.1 Light curves with `fermipy`

The procedure for creating light curves which was implemented into `fermipy` involves re-binning the data into equal time bins and then performing a full analysis of the source using only the data from each bin to extract the source flux. In order to allow for the option of multithreading, each bin analysis is performed completely separately with no shared data. This separability of the calculation into independent parts makes it a natural candidate for speed improvements via multithreading across multiple CPU cores.

Since the amount of available statistics can vary greatly between time bins, `fermipy` makes use of intelligent freeing/fixing logic of background sources according to the user's specifications. Probably most frequently used is the option to free sources within a given radius of the SOI, because these are most likely to affect the result.

C.1.1 Variability

One of the most common ways to identify flux variability from LAT data in the context of individual source analysis is through a χ^2 test, using fluxes and uncertainties extracted from each bin and taking the sum of all χ^2 values comparing them to a constant value. While this method gives a variability, it works from a reduced form of the data, and therefore it is less sensitive than a method which uses the data more fully to calculate variability. The variability calculation incorporated into `fermipy` uses a full likelihood-based computation of the flux variability, and it works by performing a likelihood ratio test within each time bin (see Appendix B).

First, the maximum likelihood is computed for the full-time analysis before the re-binning takes place. This is equivalent to assuming all sources in the ROI model are constant across time. The flux and spectrum of the SOI from this full-time constant fit are saved. Then, along with primary computation of the flux in each time bin as requested by the user's choice of free and fixed sources in the model, two separate maximum likelihood calculations are performed. In the first of these, with the state of free and fixed parameters of the ROI from the successful time bin fit, the spectrum of the SOI is set fixed to values extracted from the full-time constant fit and the likelihood is maximized. We call this $\mathcal{L}_{const}$, since it is the likelihood that the source flux is constant in time. In the second calculation, the ROI model is identical except that the normalization parameter of the SOI is set free to vary. With this changed, the maximum likelihood is once again computed as $\mathcal{L}_{fixed}$ (so called because it is different from the primary light curve only by the fixing of the SOI spectral shape parameters).

With these two quantities at hand, we compute the likelihood ratio within each bin as

$$\Lambda = \frac{\mathcal{L}_{const}}{\mathcal{L}_{fixed}}.$$

The difference in the number of free parameters between the $\mathcal{L}_{const}$ and $\mathcal{L}_{fixed}$ calculations is 1, the SOI normalization parameter. Then, according to Wilks' Theorem as shown in Eq. B.2, the TS of variability in a single bin i is

$$TS_{var,i} = -2 \ln \Lambda_i.$$

We then combine the variability likelihood ratio from all bins by taking the product, or the sum of the log-likelihoods as

$$TS_{var} = 2 \sum_i \left(\ln \mathcal{L}_{fixed,i} - \ln \mathcal{L}_{const,i} \right).$$

In accordance with the procedure carried out in the 2FGL [65] and 3FGL [34], we also introduce a systematic correction factor of $f = 0.02$, chosen so that known variable pulsar PSR J1741–2054 is computed as marginally variable. The correction factor is incorporated as

$$TS_{var} = 2\sum_{i} \frac{\sigma_{F_i}^2}{\sigma_{F_i}^2 + f^2 F_{const}^2} \left(\ln \mathcal{L}_{fixed,i} - \ln \mathcal{L}_{const,i}\right),$$

where σ_{F_i} is the error in the flux in bin i and F_{const} is the flux as extracted from the full-time constant fit. In this implementation, the bins in which the 'fixed' light curve fit did not succeed are ignored. Therefore, the TS_{var} can be interpreted as a χ^2 distribution with degrees of freedom equal to the number of successful 'fixed' light curve bins, since each uses exactly one additional free parameter.

This likelihood-based flux variability calculation is more sensitive than the simpler χ^2 method because it operates using the whole ROI data in each time bin. Because it uses the full analysis in each bin, it would be very difficult to calculate without the context of the higher-level scripting that `fermipy` provides. The calculation also makes it possible to easily compare variability determinations from individual source analysis with results reported in existing γ-ray catalogs, such as the 3FGL [34], which have used the same method.

Bibliography

[1] M Ackermann, M Ajello, L Baldini, J Ballet, G Barbiellini, D Bastieri, R Bellazzini, E Bissaldi, RD Blandford, ED Bloom, et al. Fermi large area telescope detection of extended gamma-ray emission from the radio galaxy fornax a. *The Astrophysical Journal*, 826(1):1, 2016.

[2] H Abdalla, A Abramowski, F Aharonian, F Ait Benkhali, EO Angüner, M Arakawa, C Armand, M Arrieta, M Backes, A Balzer, et al. The γ-ray spectrum of the core of centaurus a as observed with hess and fermi-lat. *arXiv preprint arXiv:1807.07375*, 2018.

[3] Harold Jeffreys. *The theory of probability*. OUP Oxford, 1998.

[4] Aous A Abdo, M Ackermann, M Ajello, L Baldini, J Ballet, G Barbiellini, D Bastieri, K Bechtol, R Bellazzini, B Berenji, et al. Fermi large area telescope observations of markarian 421: The missing piece of its spectral energy distribution. *The Astrophysical Journal*, 736(2):131, 2011.

[5] WB Atwood, Aous A Abdo, Markus Ackermann, W Althouse, B Anderson, M Axelsson, L Baldini, J Ballet, DL Band, Guido Barbiellini, et al. The large area telescope on the fermi gamma-ray space telescope mission. *The Astrophysical Journal*, 697(2):1071, 2009.

[6] Silvia Masciocchi. Semiconductor detectors - 3. SS2017, 2017.

[7] WB Atwood, R Bagagli, Luca Baldini, R Bellazzini, G Barbiellini, F Belli, T Borden, A Brez, M Brigida, GA Caliandro, et al. Design and initial tests of the tracker-converter of the gamma-ray large area space telescope. *Astroparticle Physics*, 28(4-5):422–434, 2007.

[8] Alexander A Moiseev, RC Hartman, JF Ormes, DJ Thompson, MJ Amato, TE Johnson, KN Segal, and DA Sheppard. The anti-coincidence detector for the glast large area telescope. *Astroparticle Physics*, 27(5):339–358, 2007.

[9] Edward B Fomalont, Kathleen A Ebneter, Wil JM van Breugel, and Ronald D Ekers. Depolarization silhouettes and the filamentary structure in the radio source fornax a. *The Astrophysical Journal*, 346:L17–L20, 1989.

[10] William McConville. *Investigating the Origin of Gamma-Ray Emission in Non-Blazar AGN with the Fermi Large Area Telescope*. PhD thesis, University of Maryland, College Park, 2014.

[11] Markos Georganopoulos, Rita M Sambruna, Demosthenes Kazanas, Analia N Cillis, Chi C Cheung, Eric S Perlman, Katherine M Blundell, and David S Davis. A novel method for measuring the extragalactic background light: Fermi application to the lobes of fornax a. *The Astrophysical Journal Letters*, 686(1):L5, 2008.

[12] EA Finlay and BB Jones. Measurements of source strengths at 29· 9 mhz. *Australian Journal of Physics*, 26(3):389–402, 1973.

[13] MJ Cameron. The structure of bright galaxies at 408 mhz. *Monthly Notices of the Royal Astronomical Society*, 152(4):439–460, 1971.

[14] Paul A Jones and W Bruce McAdam. The structure of southern extragalactic radio sources. *The Astrophysical Journal Supplement Series*, 80:137–203, 1992.

[15] RD Ekers, WM Goss, KJ Wellington, A Bosma, RM Smith, F Schweizer, et al. The large-scale radio structure of fornax a. *Astronomy and Astrophysics*, 127:361, 1983.

[16] John Gatenby Bolton and AJ Shimmins. The parkes 2700 mhz survey (fifth part): Catalogue for the declination zone-35o to-45o. *Australian Journal of Physics Astrophysical Supplement*, 30:1, 1973.

[17] H Kühr, A Witzel, IIK Pauliny-Toth, and U Nauber. A catalogue of extragalactic radio sources having flux densities greater than 1 jy at 5 ghz. *Astronomy and Astrophysics Supplement Series*, 45:367–430, 1981.

[18] N Isobe, K Makishima, M Tashiro, K Itoh, N Iyomoto, I Takahashi, and H Kaneda. The xmm-newton examination of energetics in the east lobe of the nearby radio galaxy fornax a (ngc 1316). *The Astrophysical Journal*, 645(1):256, 2006.

[19] B. Y. Mills, O. B. Slee, and E. R. Hill. A Catalogue of Radio Sources between Declinations -20° and -50°. *Australian Journal of Physics*, 13:676, December 1960.

[20] G Hinshaw, MR Nolta, CL Bennett, R Bean, O Doré, MR Greason, M Halpern, RS Hill, N Jarosik, A Kogut, et al. Three-year wilkinson microwave anisotropy probe (wmap*) observations: Temperature analysis. *The Astrophysical Journal Supplement Series*, 170(2):288, 2007.

[21] ED Feigelson, SA Laurent-Muehleisen, RI Kollgaard, and EB Fomalont. Discovery of inverse-compton x-rays in radio lobes. *The Astrophysical Journal Letters*, 449(2):L149, 1995.

[22] AN Cillis, RC Hartman, and DL Bertsch. Stacking searches for gamma-ray emission above 100 mev from radio and seyfert galaxies. *The Astrophysical Journal*, 601(1):142, 2004.

[23] Justin D Finke, Soebur Razzaque, and Charles D Dermer. Modeling the extragalactic background light from stars and dust. *The Astrophysical Journal*, 712(1):238, 2010.

[24] FW Stecker, OC De Jager, and MH Salamon. Tev gamma rays from 3c 279-a possible probe of origin and intergalactic infrared radiation fields. *The Astrophysical Journal*, 390:L49–L52, 1992.

[25] Fermi-LAT Collaboration et al. Fermi gamma-ray imaging of a radio galaxy. *Science*, 328(5979):725–729, 2010.

[26] N Junkes, RF Haynes, JI Harnett, and DL Jauncey. Radio polarization surveys of centaurus a (ngc 5128). i-the complete radio source at 6.3 cm. *Astronomy and Astrophysics*, 269:29–38, 1993.

[27] Gregory A Shields. A brief history of active galactic nuclei. *Publications of the Astronomical Society of the Pacific*, 111(760):661, 1999.

[28] EA Fath. The spectra of some spiral nebulae and globular star clusters. *Lick Observatory bulletin*, 5:71, 1909.

[29] Carl K Seyfert. Nuclear emission in spiral nebulae. *The Astrophysical Journal*, 97:28, 1943.

[30] H. Alfvén and N. Herlofson. Cosmic radiation and radio stars. *Phys. Rev.*, 78:616–616, Jun 1950.

[31] RC Hartman, DL Bertsch, SD Bloom, AW Chen, P Deines-Jones, JA Esposito, CE Fichtel, DP Friedlander, SD Hunter, LM McDonald, et al. The third egret catalog of high-energy gamma-ray sources. *The Astrophysical Journal Supplement Series*, 123(1):79, 1999.

[32] P Sreekumar, DL Bertsch, RC Hartman, PL Nolan, and DJ Thompson. Gev emission from the nearby radio galaxy centaurus a. *Astroparticle Physics*, 11(1):221–223, 1999.

[33] C Megan Urry and Paolo Padovani. Unified schemes for radio-loud active galactic nuclei. *Publications of the Astronomical Society of the Pacific*, 107(715):803, 1995.

[34] Fabio Acero, Markus Ackermann, M Ajello, A Albert, WB Atwood, Magnus Axelsson, Luca Baldini, J Ballet, G Barbiellini, D Bastieri, et al. Fermi large area telescope third source catalog. *The Astrophysical Journal Supplement Series*, 218(2):23, 2015.

[35] M Ackermann, M Ajello, WB Atwood, Luca Baldini, J Ballet, G Barbiellini, D Bastieri, J Becerra Gonzalez, R Bellazzini, E Bissaldi, et al. The third catalog of active galactic nuclei detected by the fermi large area telescope. *The Astrophysical Journal*, 810(1):14, 2015.

[36] M Hayashida, K Nalewajko, GM Madejski, M Sikora, R Itoh, M Ajello, RD Blandford, S Buson, J Chiang, Yasushi Fukazawa, et al. Rapid variability of blazar 3c 279 during flaring states in 2013- 2014 with joint fermi-lat, nustar, swift, and ground-based multi-wavelength observations. *The Astrophysical Journal*, 807(1):79, 2015.

[37] BL Fanaroff and JM Riley. The morphology of extragalactic radio sources of high and low luminosity. *Monthly Notices of the Royal Astronomical Society*, 167(1):31P–36P, 1974.

[38] Roger D Blandford and Roman L Znajek. Electromagnetic extraction of energy from kerr black holes. *Monthly Notices of the Royal Astronomical Society*, 179(3):433–456, 1977.

[39] Shigeo S Kimura, Kohta Murase, and Kenji Toma. Neutrino and cosmic-ray emission and cumulative background from radiatively inefficient accretion flows in low-luminosity active galactic nuclei. *The Astrophysical Journal*, 806(2):159, 2015.

[40] J Becker Tjus, B Eichmann, F Halzen, A Kheirandish, and SM Saba. High-energy neutrinos from radio galaxies. *Physical Review D*, 89(12):123005, 2014.

[41] Floyd W Stecker. Pev neutrinos observed by icecube from cores of active galactic nuclei. *Physical Review D*, 88(4):047301, 2013.

[42] Karl Mannheim. The proton blazar. *Astronomy and Astrophysics*, 269:67–76, 1993.

[43] M Böttcher, A Reimer, K Sweeney, and A Prakash. Leptonic and hadronic modeling of fermi-detected blazars. *The Astrophysical Journal*, 768(1):54, 2013.

[44] B McKinley, Ruizhi Yang, M López-Caniego, F Briggs, N Hurley-Walker, RB Wayth, AR Offringa, R Crocker, G Bernardi, P Procopio, et al. Modelling of the spectral energy distribution of fornax a: leptonic and hadronic production of high-energy emission from the radio lobes. *Monthly Notices of the Royal Astronomical Society*, 446(4):3478–3491, 2014.

[45] Xiao-na Sun, Rui-zhi Yang, Benjamin Mckinley, and Felix Aharonian. Giant lobes of centaurus a as seen in radio and γ-ray images obtained with the fermi-lat and planck satellites. *Astronomy & Astrophysics*, 595:A29, 2016.

[46] IceCube Collaboration et al. Neutrino emission from the direction of the blazar txs 0506+ 056 prior to the icecube-170922a alert. *Science*, 361(6398):147–151, 2018.

[47] J Eric Grove and W Neil Johnson. The calorimeter of the fermi large area telescope. In *Space Telescopes and Instrumentation 2010: Ultraviolet to Gamma Ray*, volume 7732, page 77320J. International Society for Optics and Photonics, 2010.

[48] AFJ Moffat. A theoretical investigation of focal stellar images in the photographic emulsion and application to photographic photometry. *Astronomy and Astrophysics*, 3:455, 1969.

[49] J Bregeon, E Charles, et al. Fermi-lat data reprocessed with updated calibration constants. *arXiv preprint arXiv:1304.5456*, 2013.

[50] Carmelo Sgrò. The new event analysis of the fermi large area telescope. In *Space Telescopes and Instrumentation 2014: Ultraviolet to Gamma Ray*, volume 9144, page 91443K. International Society for Optics and Photonics, 2014.

[51] Matthew Wood, Regina Caputo, Eric Charles, Mattia Di Mauro, Jeffrey Magill, et al. Fermipy: An open-source python package for analysis of fermi-lat data. *arXiv preprint arXiv:1707.09551*, 2017.

[52] Fred James and Matts Roos. Minuit: a system for function minimization and analysis of the parameter errors and corrections. *Comput. Phys. Commun.*, 10(CERN-DD-75-20):343–367, 1975.

[53] Barry F Madore, Wendy L Freedman, N Silbermann, Paul Harding, John Huchra, Jeremy R Mould, John A Graham, Laura Ferrarese, Brad K Gibson, Mingsheng Han, et al. The hubble space telescope key project on the extragalactic distance scale. xv. a cepheid distance to the fornax cluster and its implications. *The Astrophysical Journal*, 515(1):29, 1999.

[54] BJ Geldzahler and EB Fomalont. Radio observations of the jet in fornax a. *The Astronomical Journal*, 89:1650–1657, 1984.

[55] H Kaneda, M Tashiro, Y Ikebe, Y Ishisaki, H Kubo, K Makishima, T Ohashi, Y Saito, H Tabara, and T Takahashi. Detection of inverse-compton x-rays from lobes of the radio galaxy fornax a. *The Astrophysical Journal Letters*, 453(1):L13, 1995.

[56] Makoto S Tashiro, Naoki Isobe, Hiromi Seta, Keiko Matsuta, and Yuichi Yaji. Hard x-ray spectrum from west lobe of radio galaxy fornax a observed with suzaku. *Publications of the Astronomical Society of Japan*, 61(sp1):S327–S335, 2009.

[57] DE Harris and JE Grindlay. The prospects for x-ray detection of inverse-compton emission from radio source electrons and photons of the microwave background. *Monthly Notices of the Royal Astronomical Society*, 188(1):25–37, 1979.

[58] Judith H Croston, MJ Hardcastle, DE Harris, E Belsole, M Birkinshaw, and DM Worrall. An x-ray study of magnetic field strengths and particle content in the lobes of fr ii radio sources. *The Astrophysical Journal*, 626(2):733, 2005.

[59] Jun Kataoka and Łukasz Stawarz. X-ray emission properties of large-scale jets, hot spots, and lobes in active galactic nuclei. *The Astrophysical Journal*, 622(2):797, 2005.

[60] Naoki Isobe, Hiromi Seta, and Makoto S Tashiro. Suzaku measurement of electron and magnetic energy densities in the east lobe of the giant radio galaxy da 240. *Publications of the Astronomical Society of Japan*, 63(sp3):S947–S955, 2011.

[61] Hiromi Seta, Makoto S Tashiro, and Susumu Inoue. Suzaku detection of thermal x-ray emission associated with the western radio lobe of fornax a. *Publications of the Astronomical Society of Japan*, 65(5), 2013.

[62] YT Tanaka, G Madejski, SP O'Sullivan, CC Cheung, IJ Feain, Y Fukazawa, P Gandhi, MJ Hardcastle, J Kataoka, M Ostrowski, et al. Giant lobes of centaurus a radio galaxy observed with the suzaku x-ray satellite. *The Astrophysical Journal*, 766(1):48, 2013.

[63] SP O'Sullivan, IJ Feain, NM McClure-Griffiths, RD Ekers, E Carretti, T Robishaw, SA Mao, BM Gaensler, J Bland-Hawthorn, et al. Thermal plasma in the giant lobes of the radio galaxy centaurus a. *The Astrophysical Journal*, 764(2):162, 2013.

[64] CC Cheung and A Springmann. The central engine of active galactic nuclei (asp conf. ser. 373), ed. lc ho & j. *W. Wang (San Francisco, CA: ASP)*, 255, 2007.

[65] PL Nolan, AA Abdo, Markus Ackermann, Marco Ajello, A Allafort, E Antolini, WB Atwood, Magnus Axelsson, Luca Baldini, Jean Ballet, et al. Fermi large area telescope second source catalog. *The Astrophysical Journal Supplement Series*, 199(2):31, 2012.

[66] Dong-Woo Kim and Giuseppina Fabbiano. Chandra x-ray observations of ngc 1316 (fornax a). *The Astrophysical Journal*, 586(2):826, 2003.

[67] Y Takeuchi, Jun Kataoka, Y Takahashi, K Maeda, T Nakamori, CC Cheung, A Celotti, Y Tanaka, T Takahashi, et al. Suzaku x-ray imaging of the extended lobe in the giant radio galaxy ngc 6251 associated with the fermi-lat source 2fgl j1629. 4+ 8236. *The Astrophysical Journal*, 749(1):66, 2012.

[68] Junichiro Katsuta, YT Tanaka, SP O'Sullivan, CC Cheung, J Kataoka, S Funk, T Yuasa, H Odaka, T Takahashi, J Svoboda, et al. Fermi-lat and suzaku observations of the radio galaxy centaurus b. *Astronomy & Astrophysics*, 550:A66, 2013.

[69] A Abramowski, Fabio Acero, F Aharonian, AG Akhperjanian, G Anton, S Balenderan, A Balzer, A Barnacka, Yvonne Becherini, J Becker, et al. Constraints on the gamma-ray emission from the cluster-scale agn outburst in the hydra a galaxy cluster. *Astronomy & Astrophysics*, 545:A103, 2012.

[70] Joshua Lande, Markus Ackermann, Alice Allafort, Jean Ballet, Keith Bechtol, TH Burnett, Johann Cohen-Tanugi, Alex Drlica-Wagner, Stefan Funk, Francesco Giordano, et al. Search for spatially extended fermi large area telescope sources using two years of data. *The Astrophysical Journal*, 756(1):5, 2012.

[71] Samuel S Wilks. The large-sample distribution of the likelihood ratio for testing composite hypotheses. *The Annals of Mathematical Statistics*, 9(1):60–62, 1938.

[72] FP Israel. Centaurus a–ngc 5128. *The Astronomy and Astrophysics Review*, 8(4):237–278, 1998.

[73] Gretchen LH Harris, Marina Rejkuba, and William E Harris. The distance to ngc 5128 (centaurus a). *Publications of the Astronomical Society of Australia*, 27(4):457–462, 2010.

[74] MJ Hardcastle, DM Worrall, RP Kraft, WR Forman, C Jones, and SS Murray. Radio and x-ray observations of the jet in centaurus a. *The Astrophysical Journal*, 593(1):169, 2003.

[75] Shinji Horiuchi, David L Meier, Robert A Preston, and Steven J Tingay. Ten milliparsec-scale structure of the nucleus region in centaurus a. *Publications of the Astronomical Society of Japan*, 58(2):211–216, 2006.

[76] C Müller, Matthias Kadler, R Ojha, M Perucho, C Großberger, E Ros, J Wilms, J Blanchard, M Böck, B Carpenter, et al. Tanami monitoring of centaurus a: The complex dynamics in the inner parsec of an extragalactic jet. *Astronomy & Astrophysics*, 569:A115, 2014.

[77] Mairi H Brookes, CR Lawrence, J Keene, D Stern, V Gorijan, M Werner, and V Charmandaris. Spitzer observations of centaurus a: Infrared synchrotron emission from the northern lobe. *The Astrophysical Journal Letters*, 646(1):L41, 2006.

[78] Martin J Hardcastle, RP Kraft, and DM Worrall. The infrared jet in centaurus a: multiwavelength constraints on emission mechanisms and particle acceleration. *Monthly Notices of the Royal Astronomical Society: Letters*, 368(1):L15–L19, 2006.

[79] K Meisenheimer, KRW Tristram, W Jaffe, F Israel, N Neumayer, D Raban, H Röttgering, WD Cotton, U Graser, Th Henning, et al. Resolving the innermost parsec of centaurus a at mid-infrared wavelengths. *Astronomy & Astrophysics*, 471(2):453–465, 2007.

[80] RP Kraft, WR Forman, C Jones, SS Murray, MJ Hardcastle, and DM Worrall. Chandra observations of the x-ray jet in centaurus a. *The Astrophysical Journal*, 569(1):54, 2002.

[81] AA Abdo, Markus Ackermann, Marco Ajello, WB Atwood, Luca Baldini, J Ballet, Guido Barbiellini, D Bastieri, BM Baughman, K Bechtol, et al. Fermi large area telescope view of the core of the radio galaxy centaurus a. *The Astrophysical Journal*, 719(2):1433, 2010.

[82] R-Z Yang, Narek Sahakyan, Emma de Ona Wilhelmi, Felix Aharonian, and Frank Rieger. Deep observation of the giant radio lobes of centaurus a with the fermi large area telescope. *Astronomy & Astrophysics*, 542:A19, 2012.

[83] L Maraschi, G Ghisellini, and A Celotti. A jet model for the gamma-ray emitting blazar 3c 279. *The Astrophysical Journal*, 397:L5–L9, 1992.

[84] Steven D Bloom and Alan P Marscher. An analysis of the synchrotron self-compton model for the multi–wave band spectra of blazars. *The Astrophysical Journal*, 461:657, 1996.

[85] A Reimer and M Böttcher. Studies of active galactic nuclei with cta. *Astroparticle Physics*, 43:103–111, 2013.

[86] RL Kinzer, WN Johnson, CD Dermer, JD Kurfess, MS Strickman, JE Grove, RA Kroeger, DA Grabelsky, WR Purcell, MP Ulmer, et al. Osse observations of gamma-ray emission from centaurus a. *The Astrophysical Journal*, 449:105, 1995.

[87] H Steinle, K Bennett, H Bloemen, W Collmar, R Diehl, W Hermsen, GG Lichti, D Morris, V Schonfelder, AW Strong, et al. Comptel observations of centaurus a at mev energies in the years 1991 to 1995. *Astronomy and Astrophysics*, 330:97–107, 1998.

[88] P Sreekumar, DL Bertsch, RC Hartman, PL Nolan, and DJ Thompson. Gev emission from the nearby radio galaxy centaurus a. *Astroparticle Physics*, 11(1):221–223, 1999.

[89] Marco Chiaberge, Alessandro Capetti, and Annalisa Celotti. The bl lac heart of centaurus a. *Monthly Notices of the Royal Astronomical Society*, 324(4), 2001.

[90] F Aharonian, AG Akhperjanian, G Anton, U Barres De Almeida, AR Bazer-Bachi, Yvonne Becherini, B Behera, W Benbow, K Bernlöhr, C Boisson, et al. Discovery of very high energy γ-ray emission from centaurus a with hess. *The Astrophysical Journal Letters*, 695(1):L40, 2009.

[91] Aous A Abdo, Markus Ackermann, Marco Ajello, WB Atwood, M Axelsson, Luca Baldini, J Ballet, Guido Barbiellini, D Bastieri, BM Baughman, et al. Bright active galactic nuclei source list from the first three months of the fermi large area telescope all-sky survey. *The Astrophysical Journal*, 700(1):597, 2009.

[92] N Sahakyan, R Yang, FA Aharonian, and FM Rieger. Evidence for a second component in the high-energy core emission from centaurus a? *The Astrophysical Journal Letters*, 770(1):L6, 2013.

[93] Anthony M Brown, Céline Bœhm, Jamie Graham, Thomas Lacroix, Paula Chadwick, and Joseph Silk. Discovery of a new extragalactic population of energetic particles. *Physical Review D*, 95(6):063018, 2017.

[94] Felix Aharonian, AG Akhperjanian, AR Bazer-Bachi, M Beilicke, Wystan Benbow, David Berge, K Bernlöhr, C Boisson, Oliver Bolz, V Borrel, et al. Observations of the crab nebula with hess. *Astronomy & Astrophysics*, 457(3):899–915, 2006.

[95] James Anthony Hinton, Hess Collaboration, et al. The status of the hess project. *New Astronomy Reviews*, 48(5):331–337, 2004.

[96] A Daum, G Hermann, M Hess, W Hofmann, H Lampeitl, G Pühlhofer, F Aharonian, AG Akhperjanian, JA Barrio, AS Beglarian, et al. First results on the performance of the hegra iact array. *Astroparticle Physics*, 8(1-2):1–11, 1997.

[97] James R Mattox, DL Bertsch, J Chiang, BL Dingus, SW Digel, JA Esposito, JM Fierro, RC Hartman, SD Hunter, G Kanbach, et al. The likelihood analysis of egret data. *The Astrophysical Journal*, 461:396, 1996.

[98] Gary Hinshaw, JL Weiland, RS Hill, N Odegard, D Larson, CL Bennett, J Dunkley, B Gold, MR Greason, N Jarosik, et al. Five-year wilkinson microwave anisotropy probe* observations: data processing, sky maps, and basic results. *The Astrophysical Journal Supplement Series*, 180(2):225, 2009.

[99] F Acero, M Ackermann, M Ajello, A Albert, L Baldini, J Ballet, G Barbiellini, D Bastieri, R Bellazzini, E Bissaldi, et al. Development of the model of galactic interstellar emission for standard point-source analysis of fermi large area telescope data. *The Astrophysical Journal Supplement Series*, 223(2):26, 2016.

[100] GD Lafferty and TR Wyatt. Where to stick your data points: The treatment of measurements within wide bins. *Nuclear Instruments and Methods in Physics Research Section A: Accelerators, Spectrometers, Detectors and Associated Equipment*, 355(2-3):541–547, 1995.

[101] M Ajello, WB Atwood, L Baldini, Jean Ballet, G Barbiellini, D Bastieri, R Bellazzini, E Bissaldi, RD Blandford, ED Bloom, et al. 3fhl: the third catalog of hard fermi-lat sources. *The Astrophysical Journal Supplement Series*, 232(2):18, 2017.

[102] John Canny. A computational approach to edge detection. *IEEE Transactions on pattern analysis and machine intelligence*, (6):679–698, 1986.

[103] Shin'ichiro Ando and Daisuke Nagai. Fermi-lat constraints on dark matter annihilation cross section from observations of the fornax cluster. *Journal of Cosmology and Astroparticle Physics*, 2012(07):017, 2012.

[104] Markus Ackermann, M Ajello, A Albert, A Allafort, WB Atwood, Luca Baldini, J Ballet, G Barbiellini, D Bastieri, K Bechtol, et al. Search for cosmic-ray-induced gamma-ray emission in galaxy clusters. *The Astrophysical Journal*, 787(1):18, 2014.

[105] Markus Ackermann, M Ajello, A Allafort, P Schady, Luca Baldini, Jean Ballet, Guido Barbiellini, D Bastieri, R Bellazzini, RD Blandford, et al. The imprint of the extragalactic background light in the gamma-ray spectra of blazars. *Science*, 338(6111):1190–1192, 2012.

[106] Lauranne Lanz, Christine Jones, William R Forman, Matthew LN Ashby, Ralph Kraft, and Ryan C Hickox. Constraining the outburst properties of the smbh in fornax a through x-ray, infrared, and radio observations. *The Astrophysical Journal*, 721(2):1702, 2010.

[107] Roopesh Ojha, Matthias Kadler, M Böck, R Booth, MS Dutka, PG Edwards, AL Fey, L Fuhrmann, RA Gaume, H Hase, et al. Tanami: Milliarcsecond resolution observations of extragalactic gamma-ray sources. *arXiv preprint arXiv:1001.0059*, 2009.

[108] Mark J Burke, Elisabeth Jourdain, Jean-Pierre Roques, and Daniel A Evans. The hard x-ray continuum of cen a observed with integral spi. *The Astrophysical Journal*, 787(1):50, 2014.

[109] Helmut Steinle. Centaurus a at hard x-rays and soft gamma-rays. *Publications of the Astronomical Society of Australia*, 27(4):431–438, 2010.

[110] Guðlaugur Jóhannesson. private conversation. 2018.

[111] RA Perley, JW Dreher, and JJ Cowan. The jet and filaments in cygnus a. *The Astrophysical Journal*, 285:L35–L38, 1984.

[112] W Van Breugel and EB Fomalont. Is 3c 310 blowing bubbles? *The Astrophysical Journal*, 282:L55–L58, 1984.

[113] RA Laing, D Guidetti, AH Bridle, P Parma, and M Bondi. Deep imaging of fanaroff–riley class i radio galaxies with lobes. *Monthly Notices of the Royal Astronomical Society*, 417(4):2789–2808, 2011.

[114] Sarka Wykes, Huib T Intema, Martin J Hardcastle, Abraham Achterberg, Thomas W Jones, Helmut Jerjen, Emanuela Orrú, Alex Lazarian, Timothy W Shimwell, Michael W Wise, et al. Filaments in the southern giant lobe of centaurus a: constraints on nature and origin from modelling and gmrt observations. *Monthly Notices of the Royal Astronomical Society*, 442(4):2867–2882, 2014.

[115] Sarka Wykes, Martin J Hardcastle, and Judith H Croston. Centaurus a: constraints on the nature of the giant lobe filaments from xmm-newton observations. *Monthly Notices of the Royal Astronomical Society*, 454(3):3277–3282, 2015.

[116] P James E Peebles, DN Schramm, EL Turner, and RG Kron. The case for the relativistic hot big bang cosmology. *Nature*, 352(6338):769, 1991.

[117] DJ Fixsen. The temperature of the cosmic microwave background. *The Astrophysical Journal*, 707(2):916, 2009.